8-23-2021 10:00 AM

Considerations for the Tornado-Resilient Structural Design of Low-Rise Buildings

Cody J. Van Der Kooi, *The University of Western Ontario*

Supervisor: Bitsuamlak, Girma T., *The University of Western Ontario*

A thesis submitted in partial fulfillment of the requirements for the Master of Engineering Science degree in Civil and Environmental Engineering

Abstract

Building codes and standards have begun to incorporate tornado-specific loads to help protect community infrastructure against these potentially devastating storms, with a specific focus on low-rise buildings. The current tornado design loads are derived from atmospheric boundary layer (ABL) winds, even though it is relatively unclear to what extent tornado and ABL wind loads are equivalent for a given intensity. This research focuses on the tornado-resilient design of the main wind force resisting system (MWFRS) and component and cladding (C&C) elements of a low-rise gable roof building. Tornado loads derived from the results of experiments completed in a vortex simulator are compared to those obtained from both ABL wind tunnel tests and the proposed tornado-specific design provisions in the upcoming ASCE 7-22 standard. The external pressure datasets from the tornado and ABL wind tests are supplemented by a numerical model for internal pressure to represent enclosed and partially enclosed opening conditions. The analysis demonstrates the impact of the atmospheric pressure drop on enhancing the external tornado-induced MWFRS and C&C loads while showing that the tornado and ABL-induced loads are comparable once internal pressures are considered. Local variations attributed to increased tornado suction loads in high flow separation regions are also highlighted for the MWFRS and C&C. For the building geometry and simulated tornado studied, the peak normalized uplift forces, bending moments, and C&C pressures are found to be effectively enveloped by the ASCE 7-22 tornado design loads for the enclosed building configuration but generally exceed the ASCE loads for the perfectly sealed and partially enclosed cases. The lateral load coefficients computed from ASCE 7-22 are also found to be slightly unconservative irrespective of the opening condition. Further refinements in the internal and external pressure design values as well as the C&C loading zones may be required to better represent the tornado load conditions. Key uncertainties and limitations of the tornado data used in this study are outlined and discussed.

Keywords

Tornado, ABL wind, ASCE, low-rise buildings, wind tunnel testing, internal pressure, structural wind loads, components and cladding, WindEEE Dome

Summary for Lay Audience

Tornadoes are severe wind events that can result in enormous economic loss to communities and a significant loss of life. A large portion of tornado-induced damage is associated with low-rise buildings, which includes both residential and commercial structures. In response to this, building codes and standards in North America are beginning to incorporate clauses pertaining to tornado wind loads on buildings, which have been derived by applying adjustment factors to the design wind loads from typical storms. Since the characteristics of tornado winds differ significantly from normal straight-line winds, it is critical to understand how these variations carry through to the resulting tornado-induced loads on buildings, which can help to better inform the new tornado design provisions being included in engineering standards.

In this study, a scaled-down simulated tornado was produced at the WindEEE Dome facility at Western University. The tornado was translated past a low-rise building model, where pressure measurements were obtained on its external surface. These measurements were further supplemented by a numerical model used to estimate the internal pressures caused by the natural leakage or significant openings present in the building envelope. From the external and internal pressure data, net loads caused by the simulated tornado were derived for both the main structural system of the building (such as the primary frames) as well as for smaller component and cladding elements (such as roof and wall panels).

The experimental tornado-induced loads acting on the building were first compared to those calculated from straight-line wind tunnel data, showing that the net loads acting on the primary frames and building components behave quite similarly between the two flow regimes with some local variations. The same set of tornado loads were then compared to the proposed tornado design loads in the ASCE 7-22 standard from the United States, which revealed that the standard appears to perform well but can be slightly unconservative depending on the opening configuration of the building. The study showed that tornado wind loads are becoming more effectively understood by the engineering community, while highlighting some of the challenges that need to be addressed in future work.

Co-Authorship Statement

This thesis has been prepared according to the regulations set by the School of Graduate and Postdoctoral Studies at Western University for an Integrated Article format thesis. The co-authorship statements of the thesis chapters are as follows:

Chapter 3 is Part A of a journal article being prepared for submission, co-authored by C. Van Der Kooi and G. Bitsuamlak. C. Van Der Kooi conceptualized and carried out the experiments, conducted the data analysis and prepared the manuscript. G. Bitsuamlak assisted in experiment conceptualization and supervised the research progress.

Chapter 4 is Part B of a journal article being prepared for submission, co-authored by C. Van Der Kooi and G. Bitsuamlak. C. Van Der Kooi conceptualized and carried out the experiments, conducted the data analysis and prepared the manuscript. G. Bitsuamlak assisted in experiment conceptualization and supervised the research progress.

Acknowledgments

I would first like to extend my sincere gratitude to Dr. Girma Bitsuamlak, who was an exceptional supervisor and mentor. He was the first person to introduce me to the field of wind engineering back when I was a high school student, and his connection to resources, guidance and encouragement made this work a success.

This work was funded by a variety of sources, including the NSERC Master's Canada Graduate Scholarships, the Ontario Queen Elizabeth II Graduate Scholarships in Science and Technology, and the Alan G. Davenport Memorial Scholarship. I am extremely grateful for this financial support, which enabled me to pursue the study of wind engineering.

I am very appreciative of the assistance and technical support shared by my colleagues Anant Gairola, Tsinuel Geleta, Aaron Jaffe, Chris Howlett, Kermelos Woldeyes, and Matiyas Bezabeh, throughout my studies. I am also appreciative of the time spent by Kate Current, Matt Vandewiel, and Tsigereda Getachew Eshete to proofread this work. I would also like to extend a large thank you to all my other colleagues in the wind engineering department who made me feel welcome and were always willing to share their knowledge and experiences with me, including Abiy, Anwar, Barilelo, Clara, Hadil, Hang-You, Kim, Thomas, Eric, Muna, Meseret, Tibebu, Tewodros, Tsegaye, Samuel, Dagimawi, Aya, Sarah, Shiyu, Kamran, and Emilio.

A special note of thanks is also given to those who made the experimental testing at the WindEEE Dome possible, which was further complicated by the COVID-19 pandemic. I am deeply grateful for the hard work of Tristan Cormier and Adrian Costache, who conducted the tornado testing on my behalf due to the lockdown restrictions. I also extend my gratitude to Ian Vinkenvleugel and Gary Snyders at University Machine Services for constructing the building models for the experiment.

Finally, but most important, I would like to thank my family, especially my parents, and my girlfriend Zoe for their love and support over the last two years. Due to the pandemic, which kept us all away from campus, I had to rely on them even more for support and encouragement through all of the challenges I faced during these unique circumstances. Without them, this thesis would not have been possible.

Table of Contents

Abstract ii

Summary for Lay Audience iii

Co-Authorship Statement iv

Acknowledgments v

Table of Contents vi

List of Tables ix

List of Figures x

Nomenclature xvi

Chapter 1 1

1 Introduction 1

1.1 Background 1

1.2 Tornado Loads on a Low-Rise Structure 3

1.3 Research Objectives 7

1.4 Overview of Thesis 8

References 9

Chapter 2 14

2 Experimental Methodology and Analysis Procedure 14

2.1 Introduction 14

2.2 Tornado Experimental Testing 14

2.2.1 Tornado Simulator Description 14

2.2.2 Target Tornado and Geometric Scaling 16

2.2.3 Model Description and Experimental Setup 18

2.2.4 Pressure Coefficients and Reference Velocity 22

2.3 Atmospheric Boundary Layer Wind Aerodynamic Database 25

2.4 Comparisons between Tornado and Straight-line Wind Pressures 28
2.4.1 Equivalent Pressure Coefficients 28
2.4.2 Tap Layout and Density 29
2.5 Internal Pressure 30
2.5.1 Model Description 30
2.5.2 Model Validation 34
2.6 Conclusion 36
References 36
Chapter 3 40
3 Tornado Load Considerations for the Main Wind Force Resisting System of a Low-Rise Building 40
3.1 Introduction 40
3.2 External Wind Pressure Data 46
3.2.1 Tornado External Pressures 46
3.2.2 ABL Wind External Pressures 48
3.2.3 Mean External Pressure Distributions 51
3.3 Internal Pressure 55
3.4 Main Wind Force Resisting System (MWFRS) Analysis 59
3.4.1 Structural Model Description and Assumptions 59
3.4.2 Structural Actions and Load Coefficients 60
3.5 Results and Discussion 64
3.5.1 Tornado Load Coefficients 64
3.5.2 WindEEE Tornado versus NIST ABL Wind Load Coefficients 70
3.5.3 WindEEE Tornado versus ASCE 7-22 Tornado Load Coefficients 77
3.6 Conclusions 87
References 89

Chapter 4 94
4 Tornado Impact on the Component and Cladding Design of a Low-Rise Building 94
4.1 Introduction 94
4.2 Analysis Description 97
4.2.1 External and Internal Pressure Data 97
4.2.2 Component and Cladding Wind Loads in ASCE 7-22 103
4.3 Results and Discussion 106
4.3.1 Enveloped Tornado and ABL Peak Pressures 106
4.3.2 Enveloped Tornado and ASCE 7-22 Peak Pressures 115
4.4 Conclusions 124
References 126
Chapter 5 130
5 Conclusions 130
5.1 Summary of Findings 131
5.2 Recommendations for Future Work 132
References 133
Curriculum Vitae 135

List of Tables

Table 1.1: Estimated wind speed for each EF-Scale category of tornado intensity (Environment Canada, 2018). 2

Table 2.1: Controlling parameters for the experimental simulation of tornado flow. 16

Table 2.2: Parameters of experimental tornado cases tested at the WindEEE Dome..... 21

Table 2.3: Comparison of wind tunnel test parameters between the WindEEE Dome (TLV) and the NIST Aerodynamic Database (ABL Wind). 28

Table 2.4: Model-Scale Parameters used in the SDE and MDE equations to numerically model internal pressure. 34

Table 3.1: Summary of recent tornado experimental studies regarding overall structural loading and responses. 44

Table 3.2: Summary of the internal pressure opening cases for the low-rise building..... 55

Table 3.3: Load coefficient comparison between the tornado WindEEE experimental data, ABL NIST aerodynamic data and ASCE 7-22 design pressures for a perfectly sealed, enclosed and partially enclosed building. 83

Table 4.1: Comparison of wind tunnel test parameters between the WindEEE Dome (TLV) and the NIST Aerodynamic Database (ABL Wind). 100

Table 4.2: Summary of the internal pressure opening cases for the low-rise building..... 101

List of Figures

Figure 1.1: Mean normalized velocity, V/V_h, and turbulence intensity, I_u, profiles as a function of normalized height, z/h for atmospheric boundary layer winds generated in a wind tunnel facility (Ho et al., 2003). 3

Figure 1.2: Two-dimensional tornado wind streamlines overlaid on contours of the normalized tangential velocity, $V_{tan}/V_{tan,max}$, distributed over normalized radial distance, r/R_C, and normalized height, z/H. In addition, normalized radial profiles of tangential velocity and surface static pressures, $C_{P,static}$, are shown. All results correspond to computational simulations of a multi-celled vortex completed by the author. 4

Figure 2.1: WindEEE Dome cross-section and plan view schematics demonstrating tornado-like vortex generation. 15

Figure 2.2: (a) 2009 Goshen County, Wyoming tornado shown in its mature phase (Fitts, 2009); (b) Comparison of the normalized tangential velocity profile between WindEEE PIV measurements of a stationary tornado with a swirl ratio of 0.76 and full-scale Doppler radar measurements from the Goshen County V3 tornado record (reproduced from Refan and Hangan, 2018). 17

Figure 2.3: Layout of the (a) building model and (b) base plate for the WindEEE Dome tornado test. 19

Figure 2.4: Low-rise building model and base plate installed at the WindEEE Dome. 20

Figure 2.5: View of the pressure tubing and acquisition system underneath the WindEEE Dome test chamber. 20

Figure 2.6: Test schematic for a translating tornado in the WindEEE Dome..... 21

Figure 2.7: Cobra probe orientation and acceptance cone for wind speed measurements. 24

Figure 2.8: (a) Sample instantaneous and moving average (corresponding to 3 seconds in full-scale) horizontal wind speed time series measured at a probe orientation, α, of 30^o and probe height, z, of 60 mm. The time axis is shown at model scale. (b) vertical profile of peak 3-second

(full-scale) gust wind speeds for a cobra probe mast located at the centre of the WindEEE Dome test chamber. 25

Figure 2.9: Layout of the "Building 3" model from the NIST ABL wind aerodynamic database. The grey arrow indicates the inflow ABL wind direction. 26

Figure 2.10: (a) View of the NIST database test setup at the Alan G. Davenport Boundary Layer Wind Tunnel on the campus of Western University. (b) Simulated mean wind speed and turbulence intensity profiles for open exposure terrain. 26

Figure 2.11: Effect of pressure time series interpolation and resampling between the original NIST tap layout (left) and the WindEEE tap layout (right), illustrated by the mean external pressure distribution for a building orientation, θ, of 270^o where the inflow wind direction is shown with the grey arrow. 30

Figure 2.12: (a) Enclosed opening case with 80 holes distributed over the building walls (indicated by the blue dots). (b) Partially enclosed opening case with the 80 distributed leakage holes and an 8.13 x 1.91 m dominant opening on the predominantly windward face of the building (shown by the red rectangle). 32

Figure 2.13: Comparison between (a) ensemble-averaged internal pressure and the spatial ensemble-average of external pressure over the building envelope and (b) ensemble-averaged internal pressure and the ensemble-average ground static pressure measured at a location upstream of the building for an enclosed building oriented at $\theta = 0^o$. 35

Figure 3.1: (a) Pressure tap layout for the WindEEE test building model. (b) Test schematic for a translating tornado in the WindEEE Dome. 47

Figure 3.2: Vertical profile of peak gust horizontal velocities measured at the centre of the WindEEE Dome chamber. 48

Figure 3.3: Layout of the "Building 3" model from the NIST ABL wind aerodynamic database. The grey arrow indicates the inflow ABL wind direction. 49

Figure 3.4: Comparison of the simulated mean wind speed and turbulence intensity in the Western University BLWT II to the Engineering Science Data Unit (ESDU) profiles for open exposure terrain (Ho et al., 2003). 50

Figure 3.5: Ensemble-averaged ground surface pressures and external building pressures for building orientations of 0°, 45°, and 90° at tornado positions, y_T, of -1.5R_C to -0.5R_C. 53

Figure 3.6: Ensemble-averaged ground surface pressures and external building pressures for building orientations of 0°, 45° and 90° at vortex positions, y_T, of 0R_C to 1.0R_C..... 54

Figure 3.7: Mean external pressure distributions for the resampled NIST ABL wind data at building orientations, θ, of 180°, 225°, and 270°, with the tap layout matching the WindEEE building model. The grey arrow indicates the inflow ABL wind direction. 55

Figure 3.8: Schematics of the enclosed opening case with 80 holes distributed over the building walls (indicated by the blue dots) and the partially enclosed case with an 8.13 x 1.91 m dominant opening on the predominantly windward face of the building (shown by the red rectangle)..... 56

Figure 3.9: Comparison between ensemble-averaged tornado internal pressures between the enclosed and partially enclosed opening configurations. 57

Figure 3.10: Mean and peak internal pressure coefficients under ABL wind flow as a function of building orientation for the enclosed and partially enclosed building opening cases. 58

Figure 3.11: Structural system layout for the gable roof building model. 60

Figure 3.12: Plan view of building model with frame and bay definitions. 60

Figure 3.13: Cross sections of the moment frames and influence coefficients for the moment at the ridge of the two-pin frame and the moment at the knee of the three-pin frame system. An arrow pointing towards the centre of the building indicates a positive N_k^j value. 62

Figure 3.14: Diagram showing position of dominant opening for original (i.e. measured) and reflected building orientations for determining enveloped peak load coefficients for a partially enclosed building. 64

Figure 3.15: Load coefficients induced by tornado-like winds for building orientations, θ, of 0°, 45°, and 90° considering perfectly sealed, enclosed, and partially enclosed opening configurations. 66

Figure 3.16: Load coefficients induced by tornado-like wind for an enclosed building at orientations, θ, of 0°, 45°, and 90°. The median peak values are plotted with bars corresponding to the 10th and 90th percentiles of the set of observed peaks for each building orientation. ... 68

Figure 3.17: Normalized vortex position, y_T/R_C, corresponding to select peak observed load coefficients of each translation run for a building at orientations of 0°, 45°, and 90°. 69

Figure 3.18: Comparison of enveloped peak load coefficients between the tornado WindEEE experimental data and ABL NIST aerodynamic data for the perfectly sealed, enclosed, and partially enclosed opening configurations. 71

Figure 3.19: Instantaneous pressure distributions for an enclosed building corresponding to the peak enveloped uplift coefficients for both tornado and ABL winds. 73

Figure 3.20: Instantaneous pressure distributions for an enclosed building corresponding to the peak enveloped horizontal force coefficients for both tornado and ABL winds. 74

Figure 3.21: Instantaneous frame load distributions for an enclosed building corresponding to the peak enveloped moment coefficients at the ridge of a frame pined at the base for both tornado and ABL winds. 75

Figure 3.22: Instantaneous frame load distributions for an enclosed building corresponding to the peak enveloped moment coefficients at Knee 1 of a frame pined at the base for both tornado and ABL winds. 76

Figure 3.23: C_P values from ASCE 7-22 Figure 27.3-1 for the design of the MWFRS using the Directional procedure for (a) wind direction predominately normal to the roof ridge and (b) wind direction predominately parallel to the roof ridge. 78

Figure 3.24: Comparison of enveloped peak load coefficients between the tornado WindEEE experimental data and ASCE 7-22 design pressures for the perfectly sealed, enclosed, and partially enclosed opening configurations. 82

Figure 3.25: Case study comparison of enveloped peak loads based on a EF1 tornado reference wind speed (49.2 m/s) between the tornado experimental data and ASCE 7-22 design pressures for a perfectly sealed, enclosed, and partially enclosed building corresponding to three mean recurrence intervals (MRIs). 86

Figure 4.1: (a) Test schematic for a translating tornado in the WindEEE Dome. (b) Image of the tornado test setup in the WindEEE Dome chamber. 98

Figure 4.2: (a) Layout of the "Building 3" model from the NIST ABL wind aerodynamic database. The grey arrow indicates the inflow ABL wind direction. (b) Image of the ABL test setup in the Boundary Layer Wind Tunnel (Ho et al., 2003). 99

Figure 4.3: Schematics of the enclosed opening case with 80 holes distributed over the building walls (indicated by the blue dots) and the partially enclosed case with an 8.13 x 1.91 m dominant opening on the predominantly windward face of the building (shown by the red rectangle). 102

Figure 4.4: Component and cladding pressure coefficient zones provided by Figures 30.3-1 and 30.3-2B in ASCE 7-22 for a low rise, gable roof building with a roof slope between 7° and 20°. 105

Figure 4.5: External pressure coefficient, GC_P, envelope curves provided by ASCE 7-22 for the roof zones (defined by Figure 30.3-2B) and wall zones (defined by Figure 30.3-1)..... 105

Figure 4.6: Diagram showing position of dominant opening for original (i.e. measured) and reflected building orientations for determining enveloped peak pressures for a partially enclosed building. 106

Figure 4.7: Contour and scatter plots comparing the peak minimum enveloped pressure coefficients between tornado and ABL wind flows for a perfectly sealed building. 109

Figure 4.8: Contour and scatter plots comparing the peak minimum enveloped pressure coefficients between tornado and ABL wind flows for an enclosed building. 110

Figure 4.9: Contour and scatter plots comparing the peak minimum enveloped pressure coefficients between tornado and ABL wind flows for a partially enclosed building..... 111

Figure 4.10: Comparison of the peak negative enveloped pressure coefficients between the tornado and ABL wind flows for a perfectly sealed, enclosed, and partially enclosed building along a row of pressure taps at the model mid-section. The bars represent the 10^{th} and 90^{th} percentiles of the of the set of observed peak pressure coefficients for each building orientation. 113

Figure 4.11: Comparison of the peak negative enveloped pressure coefficients between the tornado and ABL wind flows for a perfectly sealed, enclosed, and partially enclosed building along a row of roof edge pressure taps. The bars represent the 10^{th} and 90^{th} percentiles of the of the set of observed peak pressure coefficients for each building orientation. 114

Figure 4.12: (a) Pressure taps and their tributary areas for the end walls of the building model. (b) Overlaid area-averaging cell grid corresponding to a cell aspect ratio of one. 116

Figure 4.13: Comparison of the area-averaged enveloped minimum peak pressure coefficients from the tornado experimental data to the ASCE 7-22 C&C envelope curves for a perfectly sealed building. 119

Figure 4.14: Comparison of the area-averaged enveloped minimum peak pressure coefficients from the tornado experimental data to the ASCE 7-22 C&C envelope curves for an enclosed building. 120

Figure 4.15: Comparison of the area-averaged enveloped minimum peak pressure coefficients from the tornado experimental data to the ASCE 7-22 C&C envelope curves for a partially enclosed building. 121

Figure 4.16: Case study comparison of the area-averaged enveloped minimum peak pressures from the tornado experimental data with the ASCE 7-22 C&C envelope curves for a partially enclosed building located in Chicago, IL for three mean recurrence intervals (MRI's). 123

Nomenclature

A_{ik}	Distribution of the surface pressure applied over the tributary area of tap i to the k-th attachment point
A_m	Area of opening m
a	Aspect ratio
B	Bay width
$\hat{C}_{ABL}$	Peal ABL wind load coefficients
C_P	Tornado ASCE design external pressure coefficient for the main wind force resisting system
$C_{P,eq}$	Equivalent net pressure coefficient
$C_{P_{static}}$	Static ground pressure
$C_{Pe,ABL}$	ABL wind external pressure coefficient
$C_{Pe,eq}$	Equivalent external pressure coefficient
$C_{Pe,TLV}$	Tornado-like vortex external pressure coefficient
$C_{Pi,eq}$	Equivalent internal pressure coefficient
$\hat{C}_{TLV}$	Peak tornado-like vortex load coefficients
C_Y	Lateral force coefficient
C_Z	Uplift coefficient
d	Hydraulic diameter
$E(C_{Pe,eq})$	Weighted average of external pressures by pressure tap tributary area
f_s	Sampling frequency
$F_{WT,ASCE}$	Wind tunnel factor applied to ASCE design wind pressure coefficients
$F_{WT,NIST}$	Wind tunnel factor applied to NIST ABL wind pressure coefficients
$\hat{F}_Y$	Peak lateral force
$\hat{F}_Z$	Peak uplift force

GC_P	Tornado ASCE design external pressure coefficient for components and cladding
GC_{piT}	Tornado ASCE design internal pressure coefficient
G_T	Tornado gust-effect factor
H	Inlet height in tornado vortex simulator
H_R	Roof ridge height
h	Mean height of gable-roof building
I_c	Column moment of inertia
I_g	Girder moment of inertia
I_u	Turbulence intensity
k	Discharge coefficient
K_{dT}	Tornado directionality factor
K_e	Ground elevation factor
K_{vT}	Vertical wind adjustment factor
K_{zTor}	Tornado exposure coefficient
$l_{e,m}$	Effective length of an air slug at opening m
l_i	Length of pressure tap tributary area
l_0	Opening length
m	Opening on the exterior building surface
$\widehat{M}$	Peak bending moment
N	Number of repeated tornado translation runs
N_k^j	Influence coefficient for the bending moment at cross section j due to a unit force applied at the k-th purlin
n	Flow coefficient
n_s	Number of wind speed samples corresponding to the gust averaging time
p_e	External pressure

$p_{e,m}$	External pressure at opening m
p_i	Internal pressure
p_0	Reference pressure
Q	Flow rate per unit axial length
r	Radial distance from vortex centre
r_0	Updraft radius
R_C	Core radius of tornado-like vortex
$R_{C,FS}$	Full-scale core radius
$R_{C,MS}$	Model-scale core radius
Re_r	Radial Reynolds number
S	Swirl ratio
t	Time
t_d	Tornado experimental test duration
t_s	Wind speed gust sampling time
$V_{3\ s,h,open}$	3-second peak wind gust measured at the mean roof height in open terrain
$V_{3600\ s,h,open}$	Mean hourly wind speed at the mean roof height in open terrain
V_i	Peak moving average horizontal wind speed for a given tornado translation run
V_T	ASCE 3-sec gust horizontal tornado wind speed
$\hat{V}_{TLV}$	Tornado-like vortex peak gust velocity
V/V_h	Mean normalized velocity
V_{EF1}	Upper-bound EF1 wind speed
$V_{0,m}$	Internal volume at model scale
V_{ref}	Reference wind speed
$V_{ref,ABL}$	ABL reference wind speed

$V_{ref,TLV}$	Tornado-like vortex reference wind speed
V_t	Translation speed
V_{tan}	Tangential velocity
$V_{tan,max}$	Maximum tangential velocity
W	Building width
w_i	Width of pressure tap tributary area
x_B, y_B	Building model horizontal coordinate system
x_m	Position of air slug at opening m
$\dot{x}_m$	First time derivative of air slug position at opening m
$\ddot{x}_m$	Second time derivative of air slug position at opening m
x_T, y_T	Tornado simulator horizontal coordinate system
y_T/R_C	Tornado y-axis position normalized by the core radius, R_C
z	Elevation above ground level
$z_{max,FS}$	Full-scale height of overall maximum tangential velocity in a vortex flow
$z_{max,MS}$	Model-scale height of overall maximum tangential velocity in a vortex flow
α	Cobra probe orientation
β_g	Gumbel distribution scale parameter
β_i	Angle between a vector normal to the building surface associated pressure tap i and the z–axis
Γ_{max}	Maximum circulation in the vortex flow
γ	Ratio of specific heats of air
θ	Building orientation
$\lambda_{L,ABL}$	ABL wind length scale
$\lambda_{T,ABL}$	ABL wind time scale
$\lambda_{V,ABL}$	ABL wind velocity scale

$\lambda_{L,TLV}$	Tornado-like vortex length scale
$\lambda_{T,TLV}$	Tornado-like vortex time scale
$\lambda_{V,TLV}$	Tornado-like vortex velocity scale
μ	Dynamic viscosity
μ_g	Gumbel distribution location parameter
ν	Kinematic viscosity
ρ	Density of air

Chapter 1

1 Introduction

1.1 Background

The study of the effects of extreme weather phenomena, such as tornadoes, on structures in Canada and the United States has been receiving increased attention over the past few decades. In the United States, 1225 tornado events and 74 tornado-related deaths have occurred annually, on average, between the years of 2000 to 2020 (NOAA, 2021). Canada also experiences a frequent number of tornadoes, with the Northern Tornado Project at Western University confirming an average of 67 tornado events per year between 2018 and 2020 (Northern Tornado Project, 2021). Between the period of 2009 to 2019, data collected by MunichRe's National Catastrophe Database estimated yearly insured losses in the United States due to severe convective storm events, including tornadoes, to be USD $14.4 billion (Insurance Information Institute, 2021). In 2011 alone, 1691 tornadoes occurred in the United States (NOAA, 2021) resulting in USD $25.8 billion in storm-related property damage (Munich RE, 2012). Recent tornado events in Canada have also demonstrated the devastation that these tornadoes can produce, such as the 2018 Dunrobin tornado which caused CAD $334 million in damage (Insurance Bureau of Canada, 2019). Using post-tornado damage survey information, the majority of these economic losses have been attributed to light-frame timber residential structures, but significant damage to commercial structures has also been observed (Womble et al., 2017; Wood et al., 2020; Roueche et al., 2021).

A tornado is a localized windstorm event often formed from a supercell thunderstorm, consisting of a violently rotating and translating vortex that typically leaves behind a path of destruction. The severity of a tornado is classified based on the level of observed damage, due to the challenges and infeasibility of directly measuring their wind speeds, particularly those close to the ground. Originally, the intensity of a tornado was measured by the Fujita Scale (F-Scale), introduced by Tetsuya Theodore Fujita in 1971 (Fujita, 1971). This was a forensic scale based on the analysis of post-tornado damage for

both natural and man-made structures, which are known as damage indicators (DI's). The Fujita scale was widely used for over 30 years until there was a need to update it due to limitations that lead to inconsistent use and inaccurate wind speed estimates, which were overestimated in many cases (Sills et al., 2014). In 2006, the Enhanced Fujita Scale (EF-Scale) was introduced as an improved version of the original F-Scale (McDonald et al., 2006), which measures tornado wind speeds on a scale from EF0 (lowest intensity) to EF5 (highest intensity). This new scale was adopted in 2007 by the United States and later by Environment Canada in 2013 (Environment Canada, 2018). The EF-Scale employs a large number of structures as damage indicators than the original F-Scale, therefore improving the accuracy of estimated tornado wind speeds. The estimated 3-second gust wind speeds associated with each level of the EF scale are shown below.

Table 1.1: Estimated wind speed for each EF-Scale category of tornado intensity (Environment Canada, 2018).

Enhanced Fujita Scale	3-sec Gust Wind Speed (km/h)	3-sec Gust Wind Speed (m/s)
EF0	105-137	29-38
EF1	138-178	39-49
EF2	179-218	50-60
EF3	219-266	61-73
EF4	267-322	74-89
EF5	>322	>89

In light of recent tornado disasters, communities have begun adopting tornado-resistant building codes, such as in Moore, Oklahoma after their 2013 tornado (Simmons et al., 2015). Further, tornado-specific design loads have also been included in the commentary of ASCE 7-16 (ASCE, 2017) and are expected to have a designated chapter in the upcoming ASCE 7-22 standard (ASCE, 2021). The current tornado design loads are based on atmospheric boundary layer (ABL) winds, with modification factors applied to account for tornado-specific characteristics. Therefore, assessing and understanding the

differences between ABL and tornado-induced wind loads is important in order to evaluate the effectiveness of the tornado design loads being incorporated into standards, especially with respect to low-rise buildings which represent 85% and 90% of the current North American building stock (Prevatt et al., 2012).

1.2 Tornado Loads on a Low-Rise Structure

The traditional focus of the study of wind loads on low-rise buildings has been on straight-line, ABL winds typically associated with extra-tropical cyclones or hurricanes. Over the past several decades, there has been an amassed knowledge of these synoptic winds and their effects on structures through experimental wind tunnel tests (e.g. Stathopoulos, 1979; Davenport, 1983; Ho et al., 2005) and computational studies (e.g. Dagnew and Bitsuamlak, 2013; Hajra et al., 2016; Elshaer et al., 2019). ABL winds are considered to have a non-varying mean horizontal component (i.e. stationarity) in the context of engineering design, and their mean wind profile and turbulence characteristics are highly understood, as depicted in Figure 1.1 for a typical wind tunnel study.

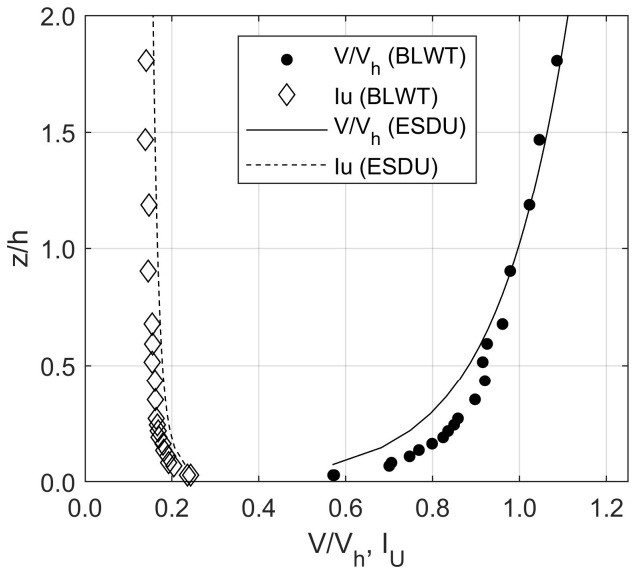

Figure 1.1: Mean normalized velocity, V/V_h, and turbulence intensity, I_u, profiles as a function of normalized height, z/h for atmospheric boundary layer winds generated in a wind tunnel facility (Ho et al., 2003).

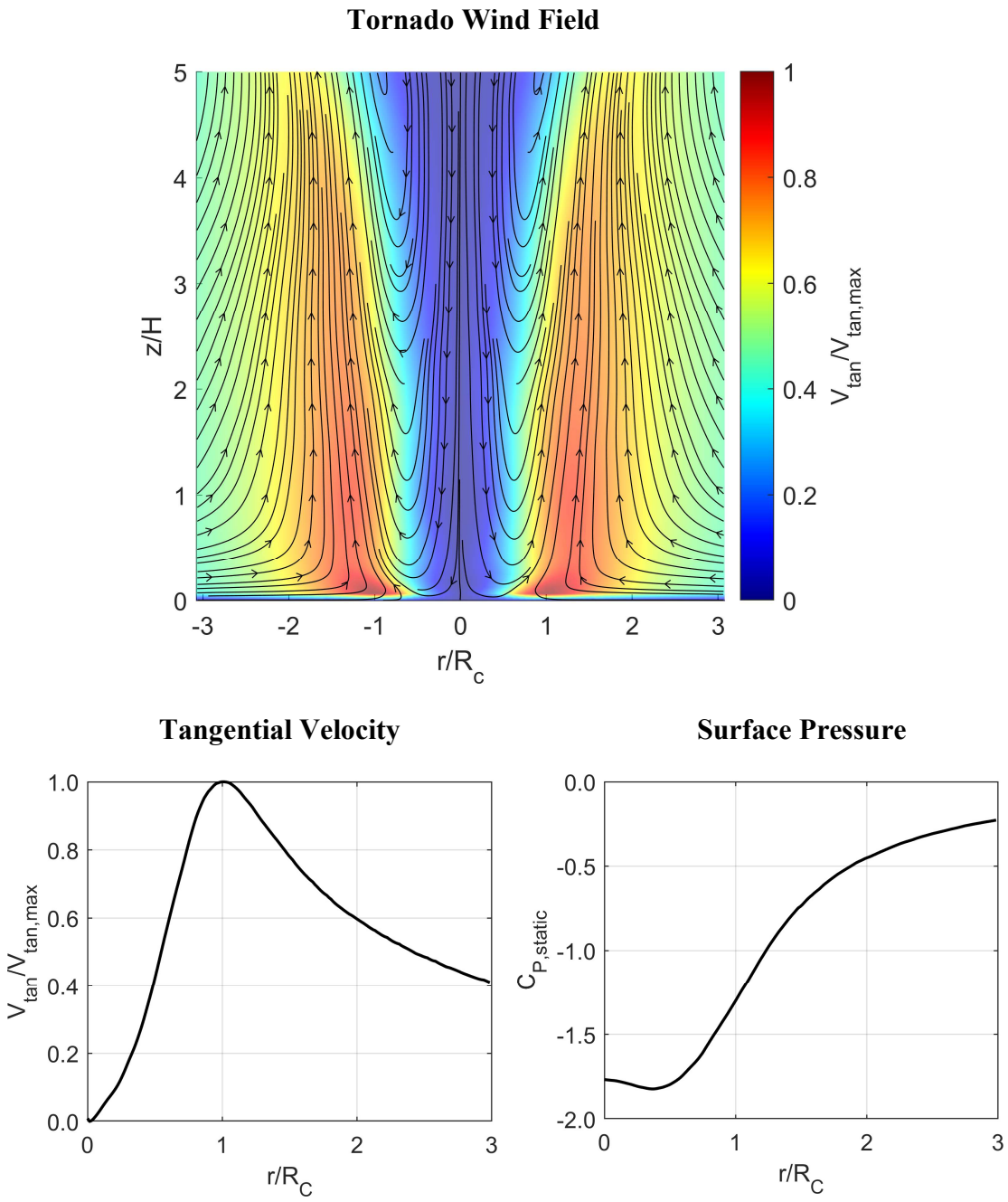

Figure 1.2: Two-dimensional tornado wind streamlines overlaid on contours of the normalized tangential velocity, $V_{tan}/V_{tan,max}$, distributed over normalized radial distance, r/R_C, and normalized height, z/H. In addition, normalized radial profiles of tangential velocity and surface static pressures, $C_{P,static}$, are shown. All results correspond to computational simulations of a multi-celled vortex completed by the author.

In contrast, the wind field of a tornado differs significantly from those of synoptic winds, as it contains significant mean rotational, radial, vertical, and translational velocity components accompanied by rapid changes in atmospheric pressure near the vortex core, as depicted in Figure 1.2 for a computational simulation of a tornado-like vortex completed by the author. Since the flow field has a significant effect on the resulting building aerodynamics and wind loads (e.g. Tieleman, 2003), it is expected that the pressure distribution on a building experiencing a tornado will differ from those of straight-line, ABL winds. Characteristics including the building location relative to the tornado core, effective wind angles of attack, wind elevation angles, gradients of static pressure, turbulence intensities, and transient and rotational wind speeds are all factors that can influence the loads on a building during a tornado (Haan, 2017; Razavi and Sarkar, 2018; Kopp and Wu, 2020; Roueche et al., 2020; Kassab, 2021).

Experimental and computational simulations of ABL wind have been widely verified by full-scale measurements (e.g. Surry, 1991), but the same full-scale measurements have been difficult to obtain for tornado winds. Tornado wind fields have been recorded using Doppler radar, which typically do not effectively capture wind velocity data in the lowest 50 metres, however, there have been a select few cases of wind speed data obtained close to the ground. Kosiba and Wurman (2013) obtained velocity measurements at a height of five metres, and indicated that the highest wind speeds may occur in the lower five metres of the wind profile. Lombardo (2018) obtained anemometer measurements at an elevation of 2.5 metres, and through analysis of the wind record showed that the variables and statistics of the tornado have significant differences versus those assumed in codes and standards for ABL winds. The lack of information on turbulence levels in tornadoes (Haan et al., 2010; Dao et al., 2014) also provides challenges for assessing the building aerodynamics and wind loads.

Several experimental simulators have been constructed to produce ‘tornado-like vortices’, which have been used to study the flow structure of tornadoes and their interactions with the built environment at the engineering scale. The first notable tornado simulator was developed by Neil Ward (Ward, 1972), which used guide vanes to induce angular momentum to a converging flow field, thus producing a stationary vortex. In the

following years, additional simulators were constructed and many studies were carried out to understand the mechanics of tornado vortex flow (Davies-Jones, 1973; Jischke and Parang, 1974; Church et al., 1977). Currently, there are 'Ward'-type simulators in operation at Texas Tech University (Mishra et al., 2008a; Mishra et al., 2008b), Tokyo Polytechnic University (Sabareesh et al., 2012), and the University of Birmingham (Gillmeier et al., 2018). In addition, relatively newer facilities have emerged that use an 'unbounded flow' design at Iowa State University (Haan et al., 2008), Tongji University (Wang et al., 2016), and Western University (Hangan, 2014).

Various studies have focused on exploring the wind pressures on low-rise structures caused by tornadoes in an effort to determine how the loads on these buildings differ from ABL winds. Mishra et al. (2008b) demonstrated the significant difference in load distributions on a cubic building experiencing tornadic wind flow versus straight-line winds. The study also highlighted the important role the atmospheric pressure drop at the vortex core plays in the resulting external wind pressures on the building. Haan et al. (2010) used a tornado-like flow field to determine the wind loads on a one-storey, gable-roofed building in smooth, open terrain and found that the overall external uplift loads exceed those from ASCE 7-05 by a factor of 3, and horizontal loads by a factor of 1.6. Hu et al. (2011) used particle-image velocimetry (PIV) to study the tornado flow field and its interaction with a low-rise gable roof building, showing that the mean flow field around the building at mid-wall height is significantly different than the ABL-induced flow when the building is located near or within the vortex core. Razavi and Sarkar (2018) investigated the influence of different parameters on external tornado loading for a low-rise gable roof building, specifically the tornado structure (governed by the swirl ratio), translation speed, building distance from the vortex path, and building orientation, finding that the building experiences maximum horizontal forces near the core radius and maximum uplift forces in the region bounded by the core radius. Razavi and Sarkar (2021) further investigated the lateral forces, uplift and bending moments on low-rise building frames with flat, gable and hip roof geometries in a translating tornado, finding that the tornado provisions of ASCE 7-16 under-predicts overall and local uplifts on a gable roof building by 41% and 55% respectively, underpredicts bending moments up to 9% for interior gable roof frames, and overpredicts overall lateral forces by up to 81%.

In addition to characterizing the external pressures, there have been a limited, but growing, number of studies seeking to understand the internal pressures within low-rise buildings induced by tornado winds. Kikitsu et al. (2011) conducted one of the first studies of internal pressures caused by tornado vortices, showing that it is a function of both the envelope porosity and opening configurations. Letchford et al. (2015) studied tornado-induced internal pressures for a variety of opening configurations, showing that the largest internal pressures are associated with a dominant opening located on the wall predominantly subjected to the impinging tornado wind flow. Roueche et al. (2020) used the classical Helmholtz resonator numerical model for tornado-induced internal pressures to demonstrate that net tornado-induced pressures can be on average 13% larger than the net pressures induced by ABL winds over the envelope of a low-rise gable roof building. Wang and Cao (2021) also studied the effect of net pressures on a cubic building with both distributed and dominant openings, finding that the current tornado load provisions in ASCE 7-16 were able to conservatively evaluate the overall uplift and base shear on the building with distributed leakage while ASCE underestimated uplift by 21% when a dominant opening was considered.

1.3 Research Objectives

From a review of the literature, it is clear that there is a rapidly growing body of work aimed at addressing the impacts of tornado loads on low-rise buildings, however there are some gaps that require further study. Most of the studies outlined used aerodynamic data derived from relatively small-scale tornado simulators while many studies were also limited in vortex translation speeds. This raises questions about turbulence, near ground wind profiles, and the ability of these tests to replicate tornadic wind fields (Baker and Sterling, 2019; Kopp and Wu, 2020), which will have a direct impact on the resulting structural loads. As a consequence of the small-scale tornadoes simulated, many building models studied were also small-scale and lacked the high pressure tap resolution necessary to conduct detailed studies of tornado loading within specific building zones. As well, the majority of the current work considered only external tornado-induced loading rather than net loads determined through either direct measurement or numerical estimations of internal pressures. Further, many of the comparisons between loads induced on low-rise

buildings by simulated tornadoes versus those from ABL winds were made to design wind loads from building standards, with very few direct comparisons made to aerodynamic data obtained from standard straight-line wind tunnel tests. Finally, there are no independent assessments available for the proposed tornado wind loads in ASCE 7-22, which would be very useful for the engineering community.

In light of these gaps, the main objective of this thesis was to compare the tornado-induced net loading on a case study low rise building to both ABL-induced wind loads and the proposed tornado design loads from ASCE 7-22 in order to evaluate their relative similarities and differences. The study will focus on the tornado wind loads impacting the main wind force resisting system (MWFRS) and component and cladding (C&C) elements of the structure. To achieve this objective, a high-frequency pressure integration (HFPI) model was developed for a low-rise building with standard geometry and tested in the Wind Engineering, Energy and Environment (WindEEE) Dome at Western University, which was capable of producing relatively large-scale tornadoes at high translation speeds. The simulated tornado had characteristics and scaling reflective of a recorded full-scale event. Further, aerodynamic loads from boundary layer wind tunnel tests were obtained for the same structure from an aerodynamic database (Ho et al., 2005). Net wind loads were determined for both datasets using a numerical model for internal pressure. The MWFRS loads were evaluated for global uplift and lateral force actions in addition to internal bending moments for an assumed structural system, while peak enveloped pressures were used to conduct the C&C analysis.

1.4 Overview of Thesis

An overview of each chapter within this thesis is as follows:

- In Chapter 2, a detailed description of the tornado experimental testing at the WindEEE Dome is provided, including the model creation, tornado scaling, and experiment configurations. An explanation of the ABL wind aerodynamic data obtained from the National Institute of Standards and Technology (NIST) database is also outlined in addition to considerations made for comparisons to the tornado-

induced loads. The theory and equations used to estimate the internal pressures are also provided.

- Chapter 3 presents the analysis completed for the MWFRS, which includes evaluation of global uplift and lateral forces in addition to bending moments in the main structural frames. Comparisons were made to both the ABL wind structural loads and the MWFRS tornado design loads included in ASCE 7-22.

- Chapter 4 focuses on the analysis of the tornado data with regard to the C&C system, through the evaluation of peak enveloped pressures at each tap and for various averaging areas. Again, comparisons were made to both ABL wind peak enveloped pressures and the ASCE 7-22 C&C loads for different zones of the building envelope.

- Chapter 5 concludes the study by summarizing the results while also discussing the study limitations and possible areas for future research.

References

ASCE, 2017. Minimum design loads and associated criteria for buildings and other structures. American Society of Civil Engineers, Reston, Virginia.

ASCE, 2021. Draft of minimum design loads and associated criteria for buildings and other structures (released for public comment). American Society of Civil Engineers, Reston, Virginia.

Baker, C., Sterling, M., 2019. Are tornado vortex generators fit for purpose? J. Wind Eng. Ind. Aerodyn. 190, 287–292. https://doi.org/10.1016/j.jweia.2019.05.011

Church, C.R., Snow, J.T., Agee, E.M., 1977. Tornado vortex simulation at Purdue University. Bull. Am. Meteorol. Soc. 58, 900–908. https://doi.org/10.1175/1520-0477(1977)058<0900:tvsapu>2.0.co;2

Dagnew, A.K., Bitsuamlak, G.T., 2013. Computational evaluation of wind loads on buildings: a review. Wind Struct. An Int. J. 16, 629–660. https://doi.org/10.12989/was.2013.16.6.629

Dao, T.N., Graettinger, A.J., Alfano, C., Gupta, R., Haan, F.L., Prevatt, D.O., Richardson, J., Kashani, A.G., 2014. Failure progression analysis of observed residential structural damage within a tornado wind field. Struct. Congr. 2014 - Proc. 2014 Struct. Congr. 1448–1459. https://doi.org/10.1061/9780784413357.128

Davenport, A.G., 1983. On the assessment of the reliability of wind loading on low buildings. J. Wind Eng. Ind. Aerodyn. 11, 21–37. https://doi.org/10.1016/0167-6105(83)90088-0

Davies-Jones, R.P., 1973. The dependence of core radius on swirl ratio in a tornado simulator. J. Atmos. Sci. https://doi.org/10.1175/1520-0469(1973)030<1427:tdocro>2.0.co;2

Elshaer, A., Bitsuamlak, G.T., Abdallah, H., 2019. Variation in wind load and flow of a low-rise building during progressive damage scenario. Wind Struct. An Int. J. 28, 389–404. https://doi.org/10.12989/was.2019.28.6.389

Fujita, T.T., 1971. Proposed characterization of tornadoes and hurricances by area and intensity (No. 91), Satellite and Mesometeorology Research Project.

Gillmeier, S., Sterling, M., Hemida, H., Baker, C., 2018. A reflection on analytical tornado-like vortex flow field models. J. Wind Eng. Ind. Aerodyn. 174, 10–27. https://doi.org/10.1016/j.jweia.2017.12.017

Haan, F.L., Sarkar, P.P., Gallus, W.A., 2008. Design, construction and performance of a large tornado simulator for wind engineering applications. Eng. Struct. 30, 1146–1159. https://doi.org/10.1016/j.engstruct.2007.07.010

Haan, F.L., Balaramudu, V., Sarkar, P.P., 2010. Tornado-induced wind loads on a low-rise building. J. Struct. Eng. 136, 106–116. https://doi.org/10.1061/(ASCE)ST.1943-541X.0000093

Haan, F.L., 2017. An examination of static pressure and duration effects on tornado-induced peak pressures on a low-rise building. Front. Built Environ. 3, 1–11. https://doi.org/10.3389/fbuil.2017.00020

Hajra, B., Bitsuamlak, G.T., Aboshosha, H., Elshaer, A., 2016. Large eddy simulation of wind induced loads on a low rise building with complex roof geometry. Proceedings, Annu. Conf. - Can. Soc. Civ. Eng. 2, 1513–1521.

Hangan, H., 2014. The Wind Engineering Energy and Environment (WindEEE) Dome at Western University, Canada. Japan Assoc. Wind Eng. 39, 350–351. https://doi.org/10.5359/jawe.39.350

Ho, E., Surry, D., Morrish, D., Nywening, M., Kopp, G.A., Simiu, E., Main, J.A., Harris, G., 2003. University of Western Ontario data sets [WWW Document]. Natl. Inst. Stand. Technol. Eng. Lab. URL https://www.nist.gov/el/materials-and-structural-systems-division-73100/nist-aerodynamic-database/university-western (accessed 1.15.21).

Ho, E., Surry, D., Morrish, D., Kopp, G.A., 2005. The UWO contribution to the NIST aerodynamic database for wind loads on low buildings: Part 1. Archiving format and basic aerodynamic data. J. Wind Eng. Ind. Aerodyn. 93, 1–30.

https://doi.org/10.1016/j.jweia.2004.07.006

Hu, H., Yang, Z., Sarkar, P.P., Haan, F.L., 2011. Characterization of the wind loads and flow fields around a gable-roof building model in tornado-like winds 835–851. https://doi.org/10.1007/s00348-011-1102-6

Insurance Bureau of Canada, 2019. 2019 facts of the property and casualty insurance industry in Canada [WWW Document]. Insur. Bur. Canada. URL http://assets.ibc.ca/Documents/Facts Book/Facts_Book/2019/IBC-2019-Facts.pdf (accessed 9.8.20).

Insurance Information Institute, 2021. Archived tables: natural catastrophe losses in the United States [WWW Document]. MunichRe NatCatSERVICE. URL https://www.iii.org/table-archive/21420 (accessed 6.10.21).

Jischke, M.C., Parang, M., 1974. Properties of simulated tornado-like vortices. J. Atmos. Sci. https://doi.org/10.1175/1520-0469(1974)031<0506:POSTLV>2.0.CO;2

Kassab, A., 2021. Experimental study of tornado-induced pressures. (Ph.D. Dissertation) Western University Electronic Thesis and Dissertation Repository.

Kikitsu, H., Sarkar, P.P., Haan, F.L., 2011. Experimental study on tornado-induced loads of low-rise buildings using a large tornado simulator, in: 13th International Conference on Wind Engineering. Amsterdam.

Kopp, G.A., Wu, C.H., 2020. A framework to compare wind loads on low-rise buildings in tornadoes and atmospheric boundary layers. J. Wind Eng. Ind. Aerodyn. 204, 104269. https://doi.org/10.1016/j.jweia.2020.104269

Kosiba, K.A., Wurman, J., 2013. The three-dimensional structure and evolution of a tornado boundary layer. Weather Forecast. 28, 1552–1561. https://doi.org/10.1175/WAF-D-13-00070.1

Letchford, C.W., Levitz, B., James, D.L., 2015. Internal pressure dynamics in simulated tornadoes, in: Structures Congress 2015. American Society of Civil Engineers, Reston, Virginia, pp. 2689–2701.

Lombardo, F.T., 2018. Engineering analysis of a full-scale high-resolution tornado wind speed record. J. Struct. Eng. (United States) 144, 1–9. https://doi.org/10.1061/(ASCE)ST.1943-541X.0001942

McDonald, J.R., Mehta, K.C., Mani, S., 2006. A recommendation for an Enhanced Fujita Scale (EF-Scale), Revision 2, Wind Science and Engineering Center, Texas Tech University. Lubbock, Texas.

Mishra, Amit R., James, D.L., Letchford, C.W., 2008. Physical simulation of a single-celled tornado-like vortex, Part A: Flow field characterization. J. Wind Eng. Ind. Aerodyn. 96, 1243–1257. https://doi.org/10.1016/j.jweia.2008.02.063

Mishra, A. R., James, D.L., Letchford, C.W., 2008. Physical simulation of a single-celled tornado-like vortex, Part B: Wind loading on a cubical model. J. Wind Eng. Ind. Aerodyn. 96, 1258–1273. https://doi.org/10.1016/j.jweia.2008.02.027

Munich RE, 2012. 2011 Natural Catastrophe: year in review [WWW Document]. Insur. Inf. Inst. URL https://www.iii.org/sites/default/files/docs/pdf/MunichRe-010412.pdf (accessed 10.5.21).

NOAA, 2021. Monthly and Annual U.S. Tornado Summaries [WWW Document]. NOAA / Natl. Weather Serv. Strorm Predict. Cent. URL https://www.spc.noaa.gov/climo/online/monthly/newm.html (accessed 6.10.21).

Northern Tornado Project, 2021. Northern Tornado Project open data [WWW Document]. URL https://westernu.maps.arcgis.com/apps/dashboards/19460b79cf24493680e5792f5247f46d (accessed 6.10.21).

Prevatt, D.O., van de Lindt, J.W., Back, E.W., Graettinger, A.J., Pei, S., Coulbourne, W., Gupta, R., James, D.L., Agdas, D., 2012. Making the case for improved structural design: tornado outbreaks of 2011. Leadersh. Manag. Eng. 12, 254–270. https://doi.org/10.1061/(asce)lm.1943-5630.0000192

Razavi, A., Sarkar, P.P., 2018. Tornado-induced wind loads on a low-rise building: Influence of swirl ratio, translation speed and building parameters. Eng. Struct. 167, 1–12. https://doi.org/10.1016/j.engstruct.2018.03.020

Razavi, A., Sarkar, P.P., 2021. Effects of roof geometry on tornado-induced structural actions of a low-rise building. Eng. Struct. 226, 111367. https://doi.org/10.1016/j.engstruct.2020.111367

Roueche, D.B., Prevatt, D.O., Haan, F.L., 2020. Tornado-induced and straight-line wind loads on a low-rise building with consideration of internal pressure. Front. Built Environ. 6, 1–18. https://doi.org/10.3389/fbuil.2020.00018

Roueche, D.B., Amini, M., Barnes, R., Crawford, S., Javadinasab Hormozabad, S., Ibrahim, H., Krautwurst, S., Pilkington, S., Rittelmeyer, B., Kijewski-Correa, T., Prevatt, D.O., Robertson, I., 2021. 25 March 2021 Deep South tornado outbreak preliminary virtual reconnaissance report, in: StEER - 25 March 2021 Deep South Tornado Outbreak. DesignSafe-CI, pp. 1–45. https://doi.org/https://doi.org/10.17603/ds2-2zs2-r990.

Sabareesh, G.R., Matsui, M., Tamura, Y., 2012. Dependence of surface pressures on a cubic building in tornado like flow on building location and ground roughness. J. Wind Eng. Ind. Aerodyn. 103, 50–59. https://doi.org/10.1016/j.jweia.2012.02.011

Sills, D.M.L., McCarthy, P.J., Kopp, G.A., 2014. Implementation and application of the EF-Scale in Canada, in: 27th Conference on Severe Local Storms. American Meterological Society, Madison, WI.

Simmons, K.M., Kovacs, P., Kopp, G.A., 2015. Tornado damage mitigation: Benefit-cost analysis of enhanced building codes in Oklahoma. Weather. Clim. Soc. 7, 169–178. https://doi.org/10.1175/WCAS-D-14-00032.1

Stathopoulos, T., 1979. Turbulent wind action on low-rise buildings. (Ph.D. Dissertation) University of Western Ontario, London, ON, Canada.

Surry, D., 1991. Pressure measurements on the Texas Tech building: Wind tunnel measurements and comparisons with full scale. J. Wind Eng. Ind. Aerodyn. 38, 235–247. https://doi.org/10.1016/0167-6105(91)90044-W

Tieleman, H.W., 2003. Wind tunnel simulation of wind loading on low-rise structures: A review. J. Wind Eng. Ind. Aerodyn. 91, 1627–1649. https://doi.org/10.1016/j.jweia.2003.09.021

Wang, J., Cao, S., Pang, W., Cao, J., Zhao, L., 2016. Wind-load characteristics of a cooling tower exposed to a translating tornado-like vortex. J. Wind Eng. Ind. Aerodyn. 158, 26–36. https://doi.org/10.1016/j.jweia.2016.09.008

Wang, J., Cao, S., 2021. Characteristics of tornado wind loads and examinations of tornado wind load provisions in ASCE 7–16. Eng. Struct. 241, 112451. https://doi.org/10.1016/j.engstruct.2021.112451

Ward, N.B., 1972. The exploration of certain features of tornado dynamics using a laboratory model. J. Atmos. Sci. 29, 1194–1204.

Womble, J.A., Wood, R.L., Smith, D.A., Louden, E.I., Mohammadi, M.E., 2017. Reality capture for tornado damage to structures. Struct. Congr. 2017 Business, Prof. Pract. Educ. Res. Disaster Manag. - Sel. Pap. from Struct. Congr. 2017 134–144. https://doi.org/10.1061/9780784480427.012

Wood, R.L., Roueche, D.B., Cullum, K., Davis, B., Gutierrez Soto, M. Javadinasab Hormozabad, S. Liao, Y., Lombardo, F.T., Moravej, M., Pilkington, S., Prevatt, D.O., Kijewski-Correa, T., Djima, W., Robertson, I., 2020. 3 March 2020 Nashville tornadoes early access reconnaissance report, in: StEER - 3 March 2020 Nashville Tornadoes. DesignSafe-CI, pp. 1–92. https://doi.org/https://doi.org/10.17603/ds2-2zs2-r990

Chapter 2

2 Experimental Methodology and Analysis Procedure

2.1 Introduction

This chapter provides a detailed description of the aerodynamic data used for the analysis of the wind loads induced by a tornado-like vortex (TLV) and atmospheric boundary layer (ABL) winds on a low-rise building. Throughout this chapter, "TLV" and "tornado" will be used interchangeably for conciseness and ease of reading. In Section 2.1, the tornado experimental wind load analysis carried out at the Wind Engineering, Energy and Environment (WindEEE) Dome is described. In Section 2.2, the ABL wind aerodynamic database prepared by the National Institute of Standards and Technology (NIST) in conjunction with Western University and the Alan G. Davenport Wind Engineering Group is discussed. Next, methods used to compare the tornado and ABL wind loads are outlined in Section 2.3. Finally, Section 2.4 describes the numerical model utilized to estimate internal pressures for both tornado and ABL winds.

2.2 Tornado Experimental Testing

2.2.1 Tornado Simulator Description

External pressures due to tornado wind loads were measured on a gable roof building model using the WindEEE Dome facility at Western University. The double-layered chamber facility is hexagonal-shaped with a 25 m diameter and 3.8 m high inner testing chamber confined within a larger 40 m diameter recirculation chamber. The simulation of tornadoes can be achieved by using six fans in the upper plenum to create the necessary tornado updraft while guide vanes located along the peripheral walls of the test chamber regulate the angular momentum of the inlet flow, as shown in Figure 2.1. The tornado updraft flows through the bellmouth back into the plenum, where it is then driven through the outer chamber and back into the test chamber by the fans. The simulator's bellmouth can travel up to 4.6 m along the y_S-axis of the chamber using a hydraulic system, enabling the simulation of translating tornadoes at speeds up to 1.5 m/s.

The WindEEE Dome facility has a larger size compared to other tornado simulators at institutions worldwide, allowing for greater measurement resolution of the near-surface tornado wind flow and pressures acting on the surfaces of buildings, which are critical elements needed for engineering design. Further, the capability of the WindEEE Dome to produce large tornado sizes at high translation speeds enables more accurate scaling of important aerodynamic properties of for simulated tornado flows (Baker and Sterling, 2019).

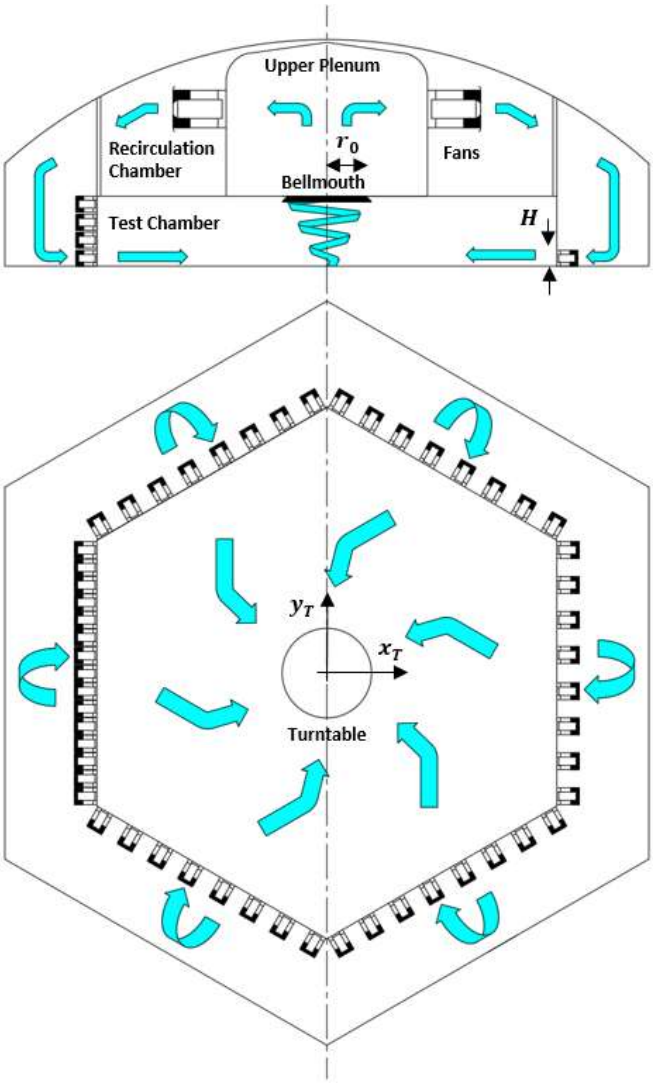

Figure 2.1: WindEEE Dome cross-section and plan view schematics demonstrating tornado-like vortex generation.

The main parameters that control the experimental tornado flow are the aspect ratio (a), the swirl ratio (S), and the radial Reynolds number (Re_r), which are all defined in Table 2.1. The swirl ratio was controlled by altering the angle of the inlet vanes located along the periphery walls of the test chamber, while the flow rate was controlled by altering the fan speed in the upper plenum. For this set of experiments, the lowest aspect ratio setting possible in the WindEEE Dome was used, corresponding to an inflow depth (H) of 0.8 m and an updraft radius (r_0) of 2.25 m. This was done in light of research indicating that naturally-occurring tornadoes have low-aspect ratios with a shallow inflow depth (Kosiba and Wurman, 2013). Further details pertaining to swirl ratio calculations and flow rate measurements are outlined in Refan and Hangan (2018).

Table 2.1: Controlling parameters for the experimental simulation of tornado flow.

Parameter	Equation	Terms
Aspect Ratio ($\boldsymbol{a}$)	$a = \frac{H}{r_0}$	r_0 = updraft radius (2.25 m) H = inflow depth (0.8 m) Γ_{max} = maximum circulation in the flow Q = flow rate per unit axial length ν = kinematic viscosity ρ = density of air (1.23 kg/m^3)
Swirl Ratio ($\boldsymbol{S}$)	$S = \frac{r_0 \Gamma_{\max}}{2QH}$	
Radial Reynolds Number ($\boldsymbol{Re_r}$)	$Re_r = \frac{Q}{2\pi\nu}$	

2.2.2 Target Tornado and Geometric Scaling

In order to obtain a representative geometric scale for the simulated tornado, the TLV was designed to target the characteristics of the 2009 Goshen County, Wyoming, tornado as closely as possible, which is depicted in Figure 2.2(a). The VORTEX2 project collected Doppler radar data for this event (Wakimoto et al., 2011), which was analyzed using the Ground-Based Velocity Track Display (GBVTD) method (Wakimoto et al., 2012; Refan et al., 2014). Using the Enhanced Fujita (EF) scale, the Goshen County tornado was rated as an EF2 by the National Weather service (NWS) based on a damage survey, but as an EF1 tornado by Refan et al. (2014) based on the maximum tangential velocity retrieved from the GBVTD analysis. Wind speed data were also collected using particle-image velocimetry (PIV) by Refan and Hangan (2018) for a series of stationary tornadoes produced in the WindEEE Dome with varying swirl ratios. From their study, it

was determined that a TLV with a swirl ratio of 0.76, core radius (R_C) of 0.60 m, aspect ratio of 0.35, and a radial Reynolds number equal to 10^6 provided a good match to the Goshen County Volume 3 (V3) tornado record. This relationship was established through a geometric length scale ($\lambda_{L,TLV}$), which was computed from two ratios corresponding to the radius (R_C) and height (z_{max}) of the maximum overall mean tangential velocity ($V_{tan,max}$) between the model-scale (MS) and full-scale (FS) tornado wind fields (Refan et al., 2014), as defined by Equation 2.1.

$$\lambda_{L,TLV_1} = \frac{R_{C,MS}}{R_{C,FS}};\ \lambda_{L,TLV_2} = \frac{z_{max,MS}}{z_{max,FS}} \tag{2.1}$$

Using this procedure, $\lambda_{L,TLV}$ was estimated as 1:200 for the experimental vortex, which demonstrates good agreement of the tangential velocity profiles near the core radius as shown in Figure 2.2(b). Further, at a swirl ratio of 0.76, it has been noted by Refan and Hangan (2018) and Kopp and Wu (2020) that the simulated tornado was two-celled, with multiple sub-vortices surrounding the central core of the vortex, which matched the observed characteristics of the Goshen County tornado (Wakimoto et al., 2012).

(a)

(b)

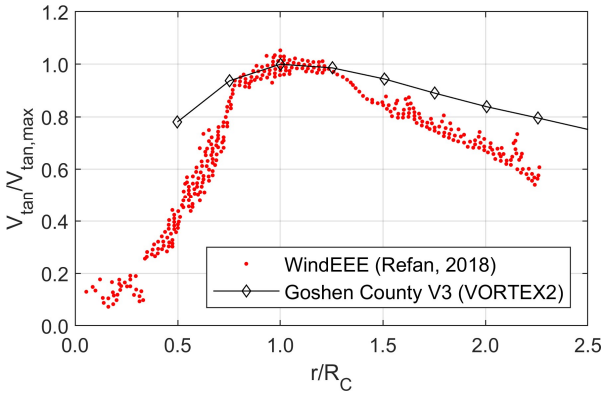

Figure 2.2: (a) 2009 Goshen County, Wyoming tornado shown in its mature phase (Fitts, 2009); (b) Comparison of the normalized tangential velocity profile between WindEEE PIV measurements of a stationary tornado with a swirl ratio of 0.76 and full-scale Doppler radar measurements from the Goshen County V3 tornado record (reproduced from Refan and Hangan, 2018).

2.2.3 Model Description and Experimental Setup

A single high-frequency pressure integration (HFPI) gable roof building model, based on the geometry from "Building 3" within the NIST database (Ho et al., 2005), was 3D printed using acrylic powder for the WindEEE tornado testing. In full-scale, the building had plan dimensions of 38.1 m by 24.4 m, an eave height of 12.2 m, and a roof pitch of 3:12 (14.4^{o}). The model was outfitted with 360 pressure taps, including 172 taps located on the roof and 188 distributed over the walls. The model was mounted on a 1118 mm diameter base plate, which contained 120 radially distributed taps used to measure ground surface pressures. The building model and base plate were both manufactured at University Machine Services at Western University. Each pressure tap was linked to one of sixteen available electronic pressure scanners using a tubing system similar to that employed by Refan and Hangan (2018), which consisted of "0.3 m long PVC tubes with 1.35 mm inner diameter, two restrictors and 0.33 m long PVC tubes with inner diameter of 0.9 mm". Diagrams of the building model and base plate with the tap layouts are provided in Figure 2.3 (a) and (b) respectively, while views of the experimental setup and pressure acquisition system are provided in Figure 2.4 and Figure 2.5.

Three scenarios were considered for the simulated tornado, with the test parameters summarized in Table 2.2. A schematic of the tornado test setup is also displayed in Figure 2.6. The tornado was translated past the building model at a speed, V_t, of 1.5 m/s, which is the fastest tornado translation speed attainable in the WindEEE Dome. The building was placed at the center of the test chamber and oriented in three directions, θ, relative to the translation direction of the tornado. Surface pressure measurements from Kassab (2021) identified that the tornado path in the WindEEE Dome at a translation speed of 1.5 m/s is curved, passing by the building at a distance equal to the core radius. This phenomenon is due to the asymmetry of the velocity field of the fast-translating tornado, which creates pressure imbalances on each side of the vortex (Kassab, 2021). The footprint area ratio, which represents the area of the building footprint relative to the area of the vortex bounded by the core radius, was determined to be 2.0%. The terrain surrounding the building was assumed to be flat and smooth, meaning that the roughness blocks (labeled in Figure 2.4) were lowered to be flush with the test chamber floor.

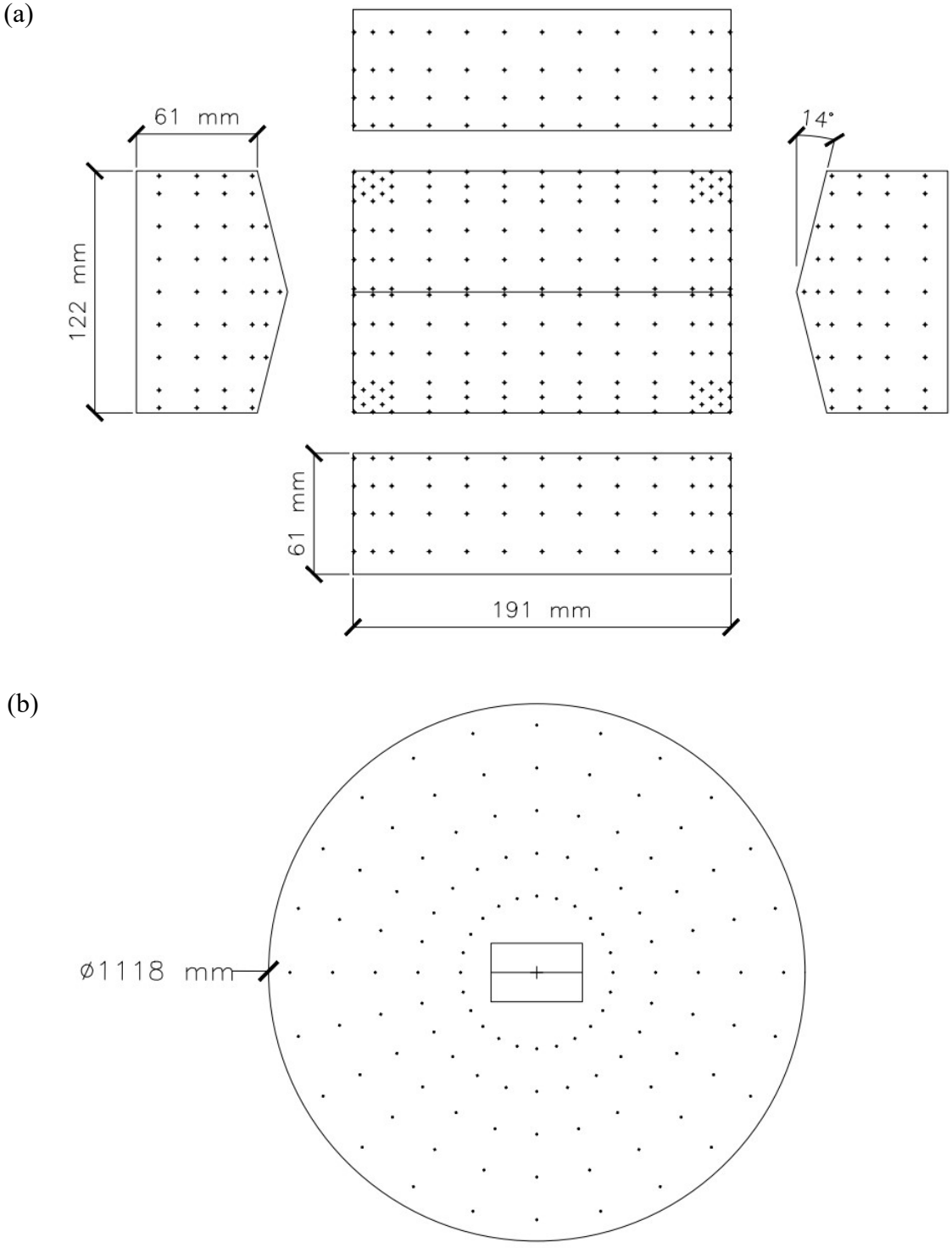

Figure 2.3: Layout of the (a) building model and (b) base plate for the WindEEE Dome tornado test.

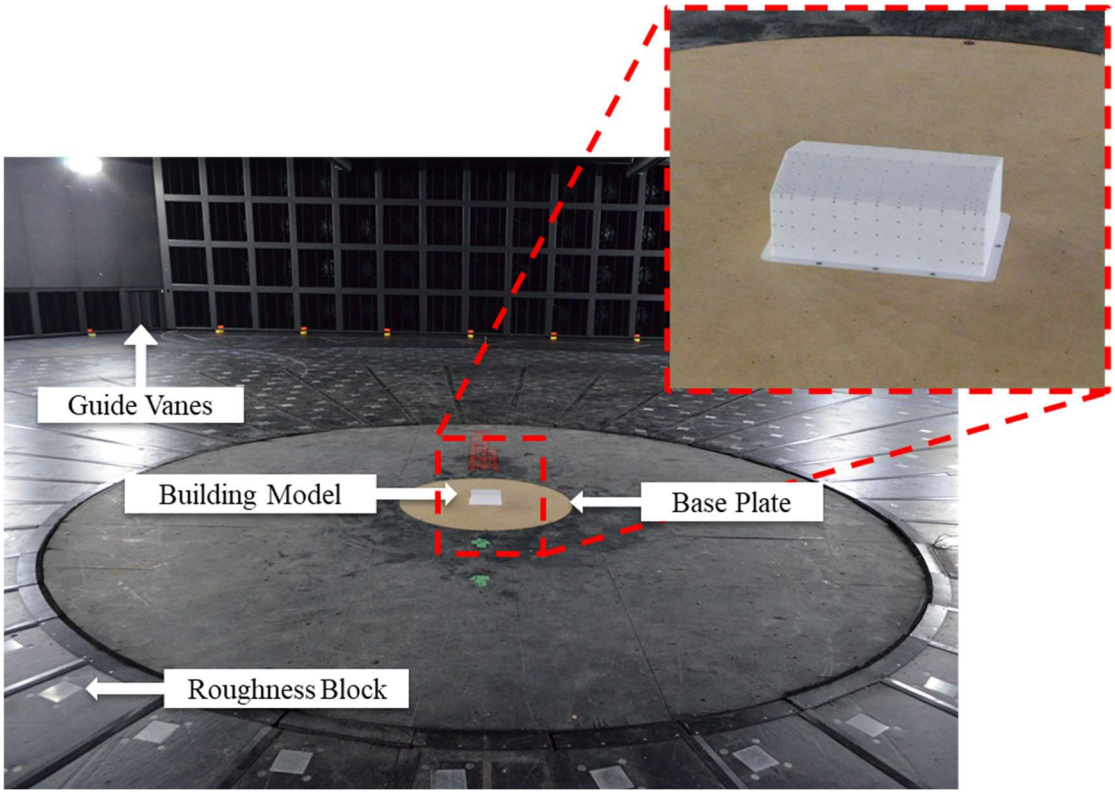

Figure 2.4: Low-rise building model and base plate installed at the WindEEE Dome.

Figure 2.5: View of the pressure tubing and acquisition system underneath the WindEEE Dome test chamber.

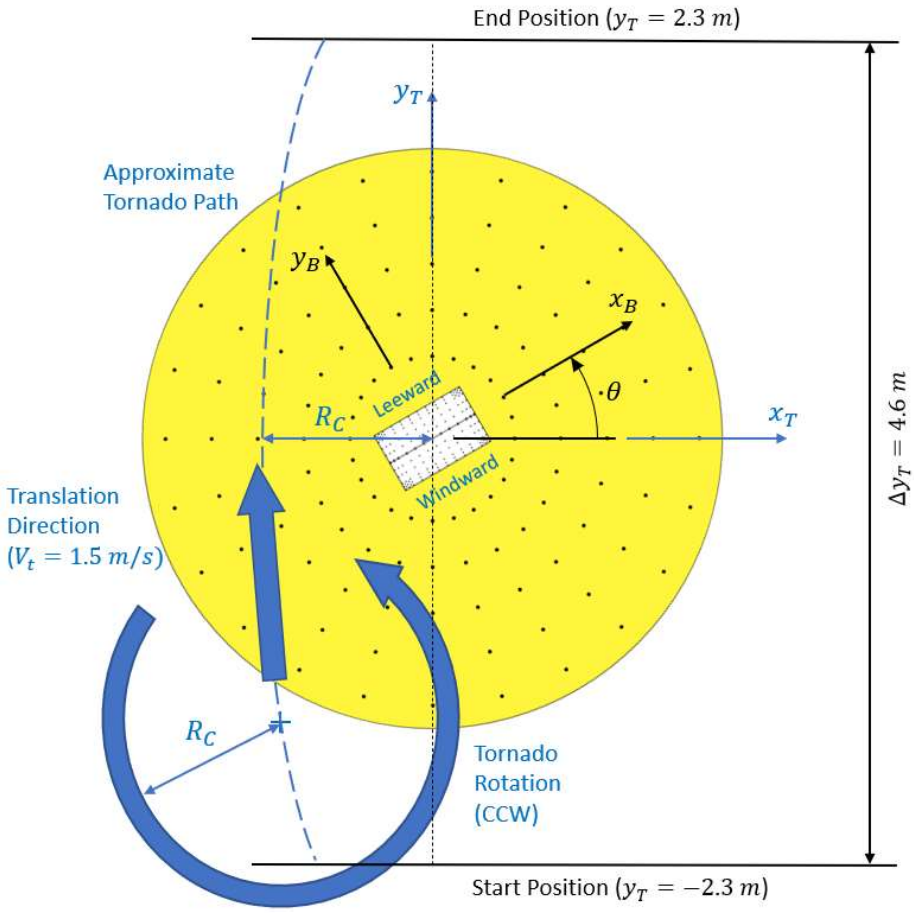

Figure 2.6: Test schematic for a translating tornado in the WindEEE Dome.

Table 2.2: Parameters of experimental tornado cases tested at the WindEEE Dome.

Vortex Characteristics	**Value**
Aspect Ratio ($\boldsymbol{a}$)	0.35
Swirl Ratio ($\boldsymbol{S}$)	0.76
Radial Reynolds Number ($\boldsymbol{Re_r}$)	1 x 10^6
Inlet Vane Angle	25°
Core Radius ($\boldsymbol{R_C}$)	0.60 m
Translation Speed ($\boldsymbol{V_t}$)	1.5 m/s
Translation Distance	4.6 m
Building Orientation ($\boldsymbol{\theta}$)	0°, 45°, 90°
Footprint Area Ratio	2.0 %

2.2.4 Pressure Coefficients and Reference Velocity

External pressure measurements were obtained at a sampling frequency of 500 Hz for a test duration of 15 seconds. 10 repeated runs were conducted for each building orientation in alignment with other studies in order to collect a representative sample of data (Haan et al., 2010; Case et al., 2014; Razavi and Sarkar, 2021). These raw pressure time series measurements were low-pass filtered at a cut-off frequency of 200 Hz before being used in the analysis. The aerodynamic data for each translating tornado run was non-dimensionalized into pressure coefficients, $C_{Pe,TLV}$, which were defined using Equation 2.2 as a function of time, t, and θ.

$$C_{Pe,TLV}(t,\theta) = \frac{p_e(t,\theta) - p_0}{\frac{1}{2}\rho V_{ref,TLV}^2} \tag{2.2}$$

In this formula, $p_e(t,\theta)$ is the measured pressure on the ground or building surface, p_0 is the ambient pressure measured outside of the test chamber, ρ is the density of air and $V_{ref,TLV}$ is the reference tornado wind speed. $V_{ref,TLV}$ was determined without the presence of the building model from separate wind speed measurements conducted by Kassab (2021) for the same tornado configuration. Cobra probes arranged in masts were used to obtain measurements of horizontal velocities at the centre of the test chamber. The cobra probes had a limited horizontal wind direction acceptance limit of ±30°, so they were re-oriented at six angles, α, to cover a wind direction range of $\pm 180^o$, as shown in Figure 2.7. For each cobra probe orientation, wind speed measurements were obtained at a sampling frequency, f_s, of 1250 Hz over five repeated tornado translation runs at heights of 10, 30, 60, 90, and 122 mm above the chamber floor. The reader can refer to Kassab (2021) for further details pertaining to the tornado wind speed experimental setup and measurements. To compute the reference tornado wind speed, first a profile of the peak gust velocity, $\hat{V}$, as a function of height from the ground, z, was determined using Equation 2.3:

$$\hat{V}_{TLV}(z) = \max_{\alpha=-150^o..150^o}\left(\frac{1}{N}\sum_{i=1}^{N}\left(\max_{t=\frac{t_s}{2}..(t_d-\frac{t_s}{2})}\left(\hat{V}_i(t,z,\alpha)\right)\right)\right) \tag{2.3a}$$

$$\hat{V}_i(t,z,\alpha) = \frac{1}{n_s}\sum_{j=1}^{n_s} V_i(j,z,\alpha) \qquad (2.3b)$$

Where α is the probe orientation (where $\alpha = \pm 30^o, \pm 90^o$ and $\pm 150^o$), N is the number of sample runs completed for each probe orientation, t_s is the wind gust averaging time, t_d is the test duration, and $\widehat{V_i}$ is the peak moving average horizontal wind speed for a given tornado translation run, i, at a specific time, t, measurement height, z, and probe orientation, α. $\widehat{V_i}$ was computed as a moving average based on a specific number of individual wind speed samples, n_s which relates to t_s via $n_s = t_s * f_s$. The moving average wind speed corresponded to a 3-second gust velocity at full-scale. An iterative procedure was implemented to determine the number of measurement samples needed to compute an equivalent full-scale 3-second moving average, since this value depended on the assumed velocity and time scales (discussed below), which conversely are influenced by the reference wind speed. A sample of the raw and moving average wind velocity time series is provided in Figure 2.8(a) for a probe orientation of $+30^o$ and height of 60 mm. The resulting profile of peak horizontal tornado wind speed constructed using Equation 2.3 is shown in Figure 2.8(b). From this peak gust velocity profile, $V_{ref,TLV} = \hat{V}(h)$, where h is the average roof height of the building model, which was computed as 16.3 m/s using linear interpolation.

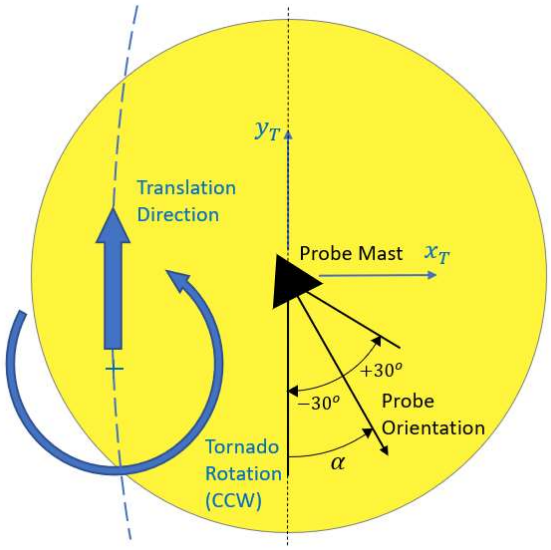

Figure 2.7: Cobra probe orientation and acceptance cone for wind speed measurements.

To estimate velocity and time scales for the tornado experiment, a full-scale reference wind speed needed to be established. In this case, it was assumed that the maximum horizontal wind speeds from the Goshen County tornado corresponded to the upper limit 3-second gust velocity for an EF1 tornado (V_{EF}), which is equal to 49.2 m/s. Therefore, the velocity scale, $\lambda_{V,TLV}$, was determined to be 1:3.0 using Equation 2.4.

$$\lambda_{V,TLV} = \frac{V_{ref,TLV}}{V_{EF1}} \tag{2.4}$$

Dividing the tornado length scale by the velocity scale, the time scale, $\lambda_{T,TLV}$, was determined to be 1:67, corresponding to t_s equal to 0.045 s.

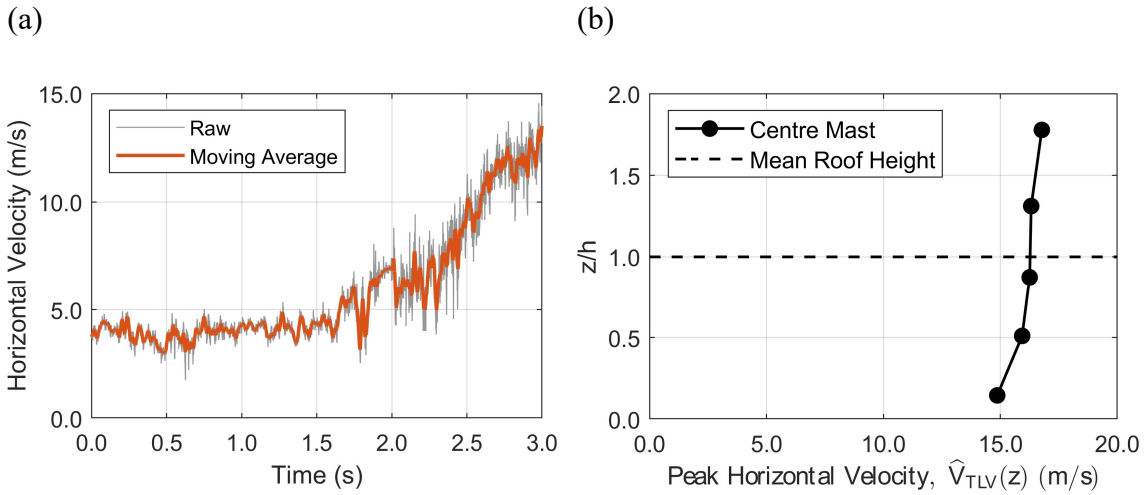

Figure 2.8: (a) Sample instantaneous and moving average (corresponding to 3 seconds in full-scale) horizontal wind speed time series measured at a probe orientation, α, of 30° and probe height, z, of 60 mm. The time axis is shown at model scale. (b) vertical profile of peak 3-second (full-scale) gust wind speeds for a cobra probe mast located at the centre of the WindEEE Dome test chamber.

2.3 Atmospheric Boundary Layer Wind Aerodynamic Database

The NIST aerodynamic database contains pressure measurements for 36 low-rise gable roof HFPI building models with varying rectangular plan dimensions, eave heights, and roof slopes (Ho et al., 2005). The database was developed from a series of experimental tests completed at the Boundary Layer Wind Tunnel (BLWT) II located on the campus of Western University. The wind tunnel measurements were archived on the NIST website (Ho et al., 2003a). Similar to the WindEEE tornado tests, "Building 3" was selected from the database for the comparison, with its geometry and tap layout depicted in Figure 2.9. Unlike the WindEEE Dome model, which was constructed at $\lambda_{L,TLV}$ of 1:200, the NIST database model corresponded to a length scale, $\lambda_{L,ABL}$ of 1:100. 677 pressure taps were distributed over the walls and roof of the building model. The building model was tested at orientations, θ, ranging between 180° to 345° in 15° increments. The symmetry of the building model was leveraged to simulate pressure data for building orientations between 0° and 165°. Only aerodynamic data from open terrain was used in the analysis,

corresponding to a roughness length, z_0, of 0.03 m. Figure 2.10(a) displays a view of the wind tunnel setup while Figure 2.10(b) shows the open-terrain profiles of the simulated mean wind speed and longitudinal turbulence intensity. Further details on the wind tunnel testing and database development are explained in Ho et al. (2005).

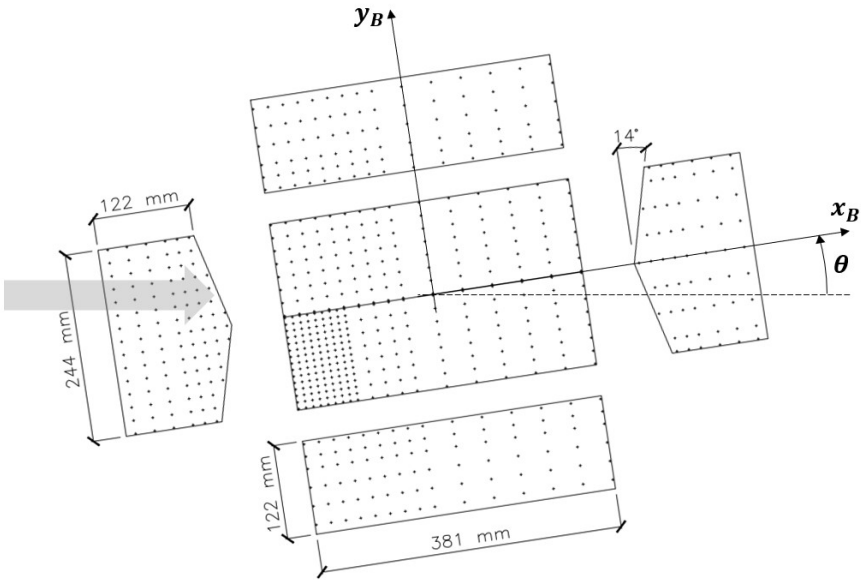

Figure 2.9: Layout of the "Building 3" model from the NIST ABL wind aerodynamic database. The grey arrow indicates the inflow ABL wind direction.

(a)

(b)

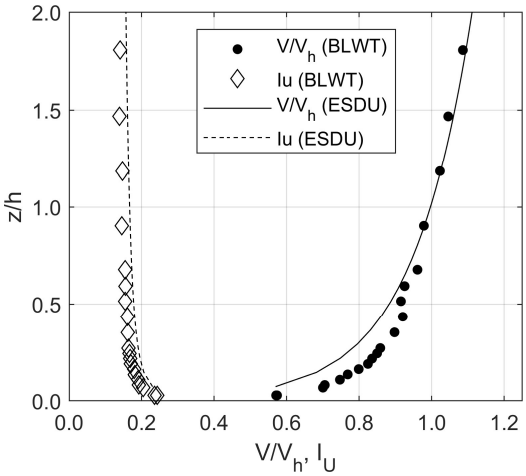

Figure 2.10: (a) View of the NIST database test setup at the Alan G. Davenport Boundary Layer Wind Tunnel on the campus of Western University. (b) Simulated mean wind speed and turbulence intensity profiles for open exposure terrain.

Pressure data were collected over a time period of 100 seconds at a sampling frequency of 500 Hz. Similar to the TLV pressure data, the ABL-induced pressure measurements were low-pass filtered at a cut-off frequency of 200 Hz before being used in the analysis. The external pressure times series were also non-dimensionalized into external pressure coefficients, $C_{Pe,ABL}$, in accordance with the definition in Equation 2.5:

$$C_{Pe,ABL}(t,\theta) = \frac{p_e(t,\theta) - p_0}{\frac{1}{2}\rho V_{ref,ABL}^2} \tag{2.5}$$

where $p(t,\theta)$ is the measured pressure on the building surface as a function of time and building orientation, p_0 is the reference ambient static pressure, and $V_{ref,ABL}$ is the reference velocity. For the ABL wind tunnel tests, $V_{ref,ABL}$ was defined as the mean hourly wind speed at the average roof height, in full-scale time dimensions. This reference wind speed was measured at an upper level in the wind tunnel where turbulence levels are relatively low and re-referenced to the roof height using a conversion factor based on the ABL wind profile (Ho et al., 2003b). It was assumed that each 100 second duration wind tunnel test corresponded to a length of 3600 s at full scale in order to represent a common storm length of one hour used for engineering design, which necessitated a time scale, $\lambda_{T,ABL}$, of 1:36. The velocity scale ($\lambda_{V,ABL}$) was therefore equal to 0.36 (or 1:2.8) via the relation stipulated by Equation 2.6.

$$\lambda_{V,ABL} = \frac{\lambda_{L,ABL}}{\lambda_{T,ABL}} \tag{2.6}$$

For comparison purposes, Table 2.3 contains relevant details of the NIST database BLWT test and the WindEEE Dome tornado test.

Table 2.3: Comparison of wind tunnel test parameters between the WindEEE Dome (TLV) and the NIST Aerodynamic Database (ABL Wind).

Parameter	WindEEE (TLV)	NIST (ABL)
Length Scale (λ_L)	1:200	1:100
Velocity Scale (λ_V)	1:3.0	1:2.8
Time Scale (λ_T)	3:200	1:36
Model Dimensions	191 mm x 122 mm x 61 mm eave height	381 mm x 244 mm x 122 mm eave height
Roof Shape	Gable, 14° roof slope	Gable, 14° roof slope
Sampling Frequency	500 Hz	500 Hz
Exposure	Open	Open ($z_0 = 0.03\ m$)
Number of Taps	360	677
Reference Velocity	3-sec gust horizontal velocity at mean roof height	3600-sec average velocity at mean roof height

2.4 Comparisons between Tornado and Straight-line Wind Pressures

To make comparisons between the WindEEE tornado experiments and the NIST straight-line wind aerodynamic database, which will be carried out in the subsequent chapters, equivalency and compatibility of the aerodynamic loads had to be addressed, using similar ideas and procedures to those outlined in St. Pierre et al. (2005) and Roueche et al. (2020).

2.4.1 Equivalent Pressure Coefficients

An equivalent pressure coefficient, $C_{Pe,eq}$, needed to be defined for comparison between tornado and ABL external pressure coefficients. Between the tornado and ABL tests, the equivalency of pressure coefficients was addressed through the reference velocities used in the calculations of dynamic pressure (i.e., $\frac{1}{2}\rho V_{ref}^2$). The standard reference velocity was taken as the definition employed for $V_{ref,TLV}$, which was a 3-second peak wind gust measured at the mean roof height in open terrain (which can be denoted generally as $V_{3\,s,h,open}$). Therefore, for the WindEEE pressure data, $C_{Pe,eq}(t,\theta) = C_{Pe,TLV}(t,\theta)$ as no adjustments to the experimental tornado pressure coefficients were

required. The NIST aerodynamic database pressure coefficients were originally referenced to a mean hourly wind speed at the mean roof height in open terrain ($V_{3600\,s,h,open}$). This hourly wind speed can be re-referenced to a 3-second wind gust by means of a wind tunnel factor, $F_{WT,NIST}$, as presented in St. Pierre et al. (2005).

$$C_{Pe,eq}(t,\theta) = F_{WT,NIST} * C_{Pe,ABL}(t,\theta) \tag{2.7a}$$

$$F_{WT,NIST} = \left(\frac{V_{3600\,s,h,open}}{V_{3\,s,h,open}}\right)^2 \tag{2.7b}$$

To calculate $F_{WT,NIST}$, the Durst Curve (Durst, 1960) was employed, resulting in $F_{WT,NIST} = \left(\frac{1}{1.52}\right)^2 = 0.43$.

2.4.2 Tap Layout and Density

As depicted by Figure 2.3(a) and Figure 2.9, there were variations in the tap layouts and densities between the WindEEE and NIST HFPI models. The WindEEE building model contained 360 pressure taps with a doubly symmetric distribution along with increased tap densities around the building wall edges, roof edges and roof corners. The NIST database model had 677 taps, with denser tap densities along the wall edges and towards one side of the roof. Since the NIST model had a denser tap layout, the pressure time series were interpolated and resampled to match the number and positions of the WindEEE building model pressure taps. Interpolation was carried out using the Nearest-Neighbour interpolation scheme implemented using the "*scatteredInterpolant*" function in MATLAB, with the interpolation theory outlined in Amidror (2002). After interpolation and resampling, the pressure distributions matched well with some minor distortions, which was deemed acceptable for this study. As an example, a comparison of the mean external pressure distributions between the original and resampled tap layouts of the NIST building for θ equal to 270° is shown in Figure 2.11.

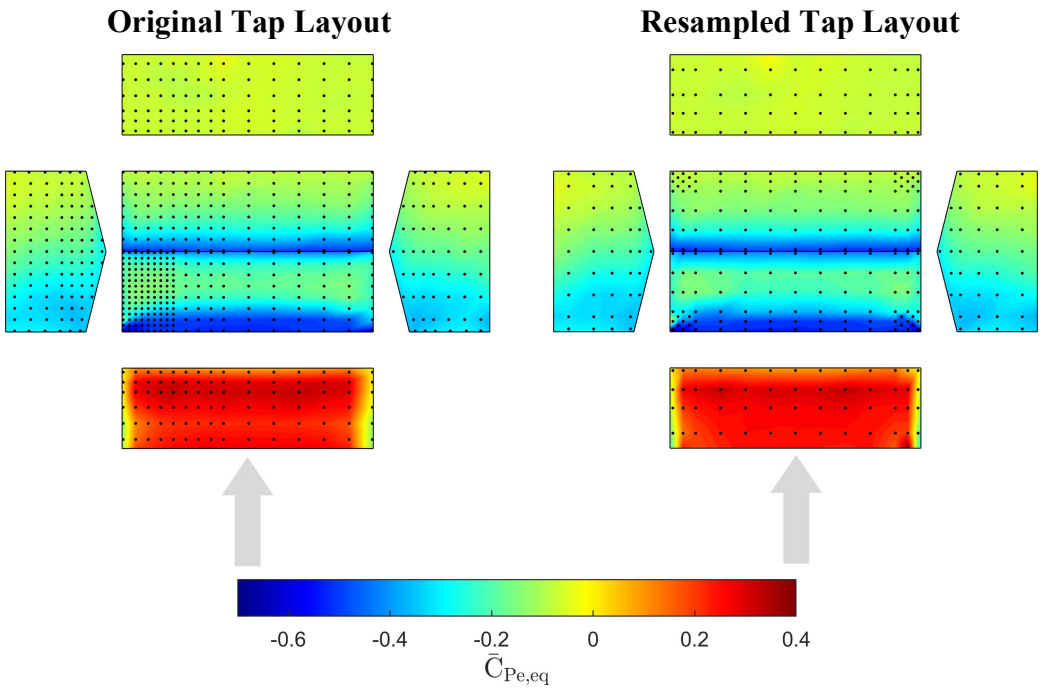

Figure 2.11: Effect of pressure time series interpolation and resampling between the original NIST tap layout (left) and the WindEEE tap layout (right), illustrated by the mean external pressure distribution for a building orientation, θ, of 270° where the inflow wind direction is shown with the grey arrow.

2.5 Internal Pressure

2.5.1 Model Description

Net pressure coefficients, $C_{P,eq}$, were utilized for analysis in Chapters 3 and 4, which are defined as follows:

$$C_{P,eq}(t,\theta) = C_{Pe,eq}(t,\theta) - c_{Pi,eq}(t,\theta) \tag{2.8}$$

where $C_{Pe,eq}(t,\theta)$ and $C_{Pi,eq}(t,\theta)$ are the time series of external and internal pressure coefficients for a specific building orientation. Therefore, considerations needed to be made for internal pressures. Three opening cases were assumed across the building envelope:

i) **Perfectly Sealed:** In this case, only external pressures are considered for the net loading. This case is applicable to buildings where special measures are taken to seal the interior of the building from atmospheric conditions (ASCE, 2021).

ii) **Enclosed:** This case represented the distributed leakage inherent in most buildings, which have a porosity ratio (defined as the ratio of the whole leakage area to the entire building surface area) typically on the order of 0.01% to 0.1% (Ginger et al., 1997). Openings were assumed to be located at 80 locations distributed over the building walls and roof as shown in Figure 2.12(a), each with an area of 0.032 m^2 in full-scale. This resulted in a porosity ratio of 0.1%, with the openings distributed such that the porosity ratio was equivalent on each building surface.

iii) **Partially Enclosed:** In accordance with the definition within Table 26.13-1 of the proposed ASCE 7-22 standard, a partially enclosed building has an opening that is at least 10% larger than the remaining balance of openings in the building envelope. In this study, a dominant opening, with full-scale dimensions of 8.13 m by 1.91 m, was assumed to be located on the predominantly windward wall of the building as shown in Figure 2.12(b). It was also assumed that the 80 small holes that represent the distributed leakage were also present. The dominant opening corresponded to a porosity ratio of 3.3%, defined as the ratio of the opening area to the single wall area, and typically represents the "worst-case" design scenario if the wind angle of attack aligns with the opening. The size and location of the opening matches that given for the NIST database tests for 12.2 m eave height buildings, as described in Oh et al. (2007).

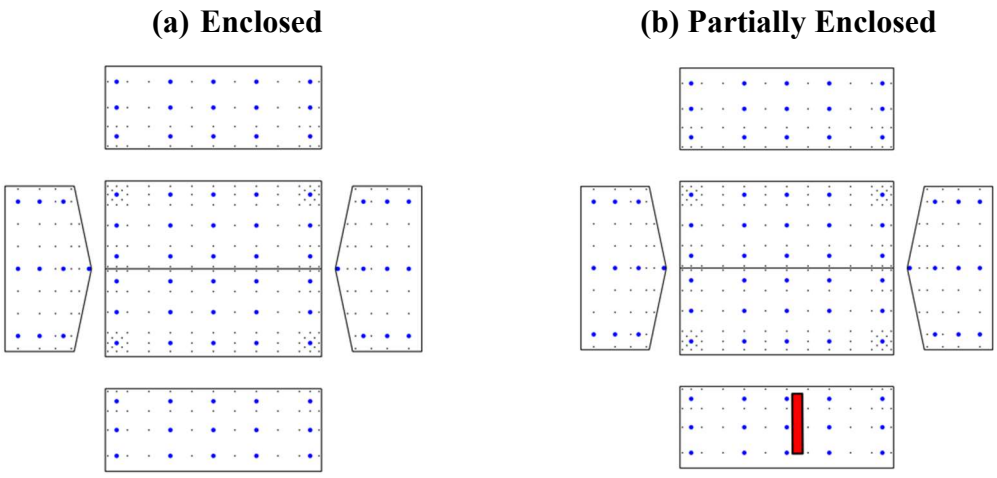

Figure 2.12: (a) Enclosed opening case with 80 holes distributed over the building walls (indicated by the blue dots). (b) Partially enclosed opening case with the 80 distributed leakage holes and an 8.13 x 1.91 m dominant opening on the predominantly windward face of the building (shown by the red rectangle).

Internal pressures were not directly measured in the WindEEE Tornado tests or NIST aerodynamic database for the defined opening cases due to the difficulties and cost associated with constructing building models to capture these measurements. As such, internal pressures were modeled using the external pressure distributions and assumptions about the locations of openings in the building envelope. The Multiple Discharge Equations (MDE's) for unsteady, incompressible flow were used to simulate the internal pressures, which is based on the classical Helmholtz resonator. The MDE's or similar models have been successfully utilized in the past to estimate internal pressures in synoptic wind flow (Holmes, 1980; Vickery, 1986; Oh et al., 2007; Tecle et al., 2015) and non-synoptic tornado winds (Roueche et al., 2020; Jaffe and Kopp, 2021). The MDE's take the following form at each assumed building opening:

$$\rho l_{e,m}\ddot{x}_m + \left(\frac{1}{k_m}\right)^{\frac{1}{n}}\left(\frac{\rho}{2}\right)^{\frac{1}{2n}}\dot{x}_m|\dot{x}_m|^{\left(\frac{1}{n}\right)-1} + \frac{32\mu l_0}{d^2}\dot{x}_m = (p_{e,m} - p_0) - p_i \qquad (2.9)$$

where m represents each opening on the exterior building surface, $l_{e,m}$ is the effective length of an air slug at opening m, x is the position of the air slug moving through opening m, k is the discharge coefficient, n is the flow coefficient, μ is the dynamic viscosity of

air, l_0 is the opening length, d is the hydraulic diameter of the opening (where $d = 2\sqrt{A/\pi}$), $p_{e,m}$ is the measured external pressure at opening m, p_0 is the ambient atmospheric pressure, and p_i is the computed internal pressure. Since the set of m MDE's contain $m + 1$ unknown quantities, x_m and p_i, the continuity equation is also invoked to provide an additional equation to solve for the internal pressure. Assuming the pressure-density relationship is governed by an isentropic process (i.e. $x = \frac{V_0}{A_0 \gamma p_0} p$), the continuity equation can be written as follows:

$$\rho(A_1 x_1 + A_2 x_2 + \cdots + A_m x_m) = \frac{\rho V_0}{\gamma p_0} p_i \tag{2.10}$$

where A_m is the area of building opening m, γ is the ratio of specific heats of air, and all other terms are previously defined.

The MDE's were solved at model scale for both the WindEEE tornado and NIST ABL data. In order to maintain dynamic similitude between full and model scales, the internal volume of the building needed to be scaled in accordance with Equation 2.11 below (Holmes, 1980).

$$V_{o,MS} = V_{o,FS}\left(\frac{\lambda_L^3}{\lambda_V^2}\right) \tag{2.11}$$

Coefficients terms for the MDE's or SDE's were taken following the recommendations of Vickery (1986) and Oh et al. (2007). Table 2.4 outlines these coefficients in addition to the model scale dimensions used in the equations. The non-linear MDE equations were solved using a backwards differencing scheme (Thomas, 1995) in conjunction with the Point-Jacobi iterative method (Black et al., 2021) to produce a time series of internal pressure for each opening configuration. The modeled time series of internal pressures for each building orientation (i.e. $p_i(t, \theta)$) were non-dimensionalized in pressure coefficient form, $C_{Pi,eq}(t, \theta)$, as follows:

$$C_{Pi,eq}(t, \theta) = \frac{p_i(t, \theta)}{\frac{1}{2}\rho V_{ref}^2} \tag{2.12}$$

where V_{ref}^2 is equivalent to $V_{ref,TLV}^2$ for the tornado internal pressures and is equal to $V_{ref,ABL}^2/F_{WT,NIST}$ for the ABL internal pressures.

Table 2.4: Model-Scale Parameters used in the SDE and MDE equations to numerically model internal pressure.

Variable Name	Symbol	TLV (1:200 Model Scale)	ABL (1:100 Model Scale)
Density of air	ρ	1.23 kg/m^3	1.23 kg/m^3
Wall thickness of building	l_0	7.60 x 10^{-4} m	1.52 x 10^{-3} m
Opening Area	a		
Leakage Taps		8.01 x 10^{-7} m^2	3.20 x 10^{-6} m^2
Large Opening		1.25 x 10^{-4} m^2	4.95 x 10^{-4} m^2
Effective Length	$l_e = 0.89\sqrt{a} + l_0$		
Leakage Taps		1.56 x 10^{-3} m	3.11 x 10^{-3} m
Large Opening		1.07 x 10^{-2} m	2.13 x 10^{-2} m
Internal volume of the building	V_0	1.44 x 10^{-2} m^3	9.85 x 10^{-2} m^3
Ambient atmospheric pressure	P_0	1.00 x 10^5 Pa	1.00 x 10^5 Pa
Ratio of specific heats of air	γ	1.40	1.40
Discharge coefficient	k		
Leakage Taps		0.38	0.38
Large Opening		0.63	0.63
Flow Coefficient	n		
Leakage Taps		0.70	0.70
Large Opening		0.50	0.50

2.5.2 Model Validation

As previously stated, the multiple-discharge equations have been well-verified against measured internal pressures from ABL wind flows, and initial steps were taken to validate the numerical model against data from the NIST database for enclosed and partially enclosed buildings with differing geometry from the model employed herein. Steps were also taken to verify the internal pressure model against common observations from literature for internal tornado-induced pressures in buildings with a single internal

volume. The first common observation is that the modeled internal pressure should have a value close to the weighted average of external pressures by pressure tap tributary area, denoted $E(C_{Pe,eq})$ (Letchford et al., 2015; Wang et al., 2018; Jaffe and Kopp, 2021; Kassab, 2021). This trend is clearly reflected in Figure 2.13(a), which compares the ensemble-averages of estimated internal pressures and weighted averaged external pressures for an enclosed building with an orientation of 0°. Further, it is commonly observed that the internal pressure in an enclosed building partially or fully equilibrates the atmospheric pressure drop (APD) across the building envelope (Kikitsu et al., 2011; Roueche et al., 2020). Figure 2.13(b) demonstrates the effect of the internal pressure to equilibrate most of the APD through a comparison of the internal pressures for an enclosed building to the ensemble-averaged surface pressure coefficients, $C_{P_{static}}$. In this comparison, the surface pressures were measured at taps upstream and in-line with the building model but were shifted to align with the drop in internal pressure.

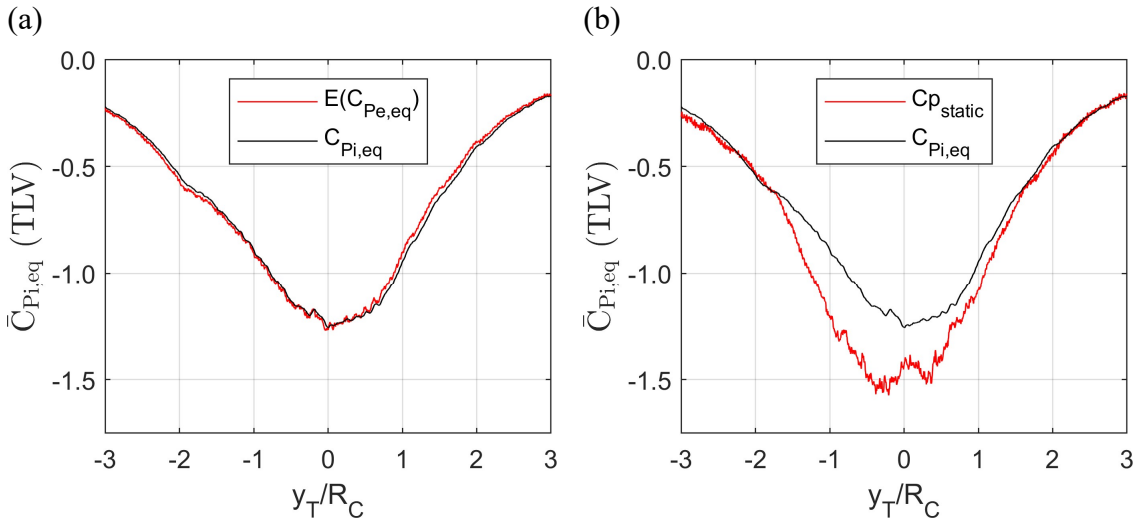

Figure 2.13: Comparison between (a) ensemble-averaged internal pressure and the spatial ensemble-average of external pressure over the building envelope and (b) ensemble-averaged internal pressure and the ensemble-average ground static pressure measured at a location upstream of the building for an enclosed building oriented at $\theta = 0^o$.

2.6 Conclusion

This chapter outlined the experimental methodology used to determine the aerodynamic data to be considered in the analyses conducted in the subsequent chapters. First, the tornado experiments conducted at the WindEEE Dome were presented, including details pertaining to the building model, vortex characteristics and external pressure data extraction. Next, the chapter explained the NIST aerodynamic database which was used to obtain external pressure measurements from an ABL wind field for the same low-rise building geometry. Modifications made to the ABL external pressure coefficients, including changes in the reference velocity and data resampling, were outlined so that the data could be compared to the tornado pressure coefficients. Finally, the multiple discharge equation numerical model was described as a method to estimate the internal pressures for the tornado and ABL wind aerodynamic data.

References

Amidror, I., 2002. Scattered data interpolation methods for electronic imaging systems: a survey. J. Electron. Imaging 11, 157–176. https://doi.org/10.1117/1.1455013

ASCE, 2021. Draft of minimum design loads and associated criteria for buildings and other structures (released for public comment). American Society of Civil Engineers, Reston, Virginia.

Baker, C., Sterling, M., 2019. Are tornado vortex generators fit for purpose? J. Wind Eng. Ind. Aerodyn. 190, 287–292. https://doi.org/10.1016/j.jweia.2019.05.011

Black, N., Moore, S., Weisstein, E.W., 2021. Jacobi Method [WWW Document]. MathWorld - A Wolfram Web Resour. URL https://mathworld.wolfram.com/JacobiMethod.html (accessed 1.30.21).

Case, J., Sarkar, P.P., Sritharan, S., 2014. Effect of low-rise building geometry on tornado-induced loads. J. Wind Eng. Ind. Aerodyn. 133, 124–134. https://doi.org/10.1016/j.jweia.2014.02.001

Durst, C.S., 1960. The statistical variation of wind with distance. Q. J. R. Meteorol. Soc. 86, 543–549.

Fitts, D., 2009. June 5, 2009 Goshen County, Wyoming Tornado [WWW Document]. NOAA Natl. Weather Serv. URL https://www.weather.gov/cys/GoshenCountyTornado#:~:text=The most photogenic tornado in,team and The Weather Channel.&text=The tornado remained in

open,Mature rain wrapped tornado.

Ginger, J.D., Mehta, K.C., Yeatts, B.B., 1997. Internal pressures in a low-rise full-scale building. J. Wind Eng. Ind. Aerodyn. 72, 163–174. https://doi.org/10.1016/S0167-6105(97)00241-9

Haan, F.L., Balaramudu, V., Sarkar, P.P., 2010. Tornado-induced wind loads on a low-rise building. J. Struct. Eng. 136, 106–116. https://doi.org/10.1061/(ASCE)ST.1943-541X.0000093

Ho, E., Surry, D., Morrish, D., Nywening, M., Kopp, G.A., Simiu, E., Main, J.A., Harris, G., 2003a. University of Western Ontario data sets [WWW Document]. Natl. Inst. Stand. Technol. Eng. Lab. URL https://www.nist.gov/el/materials-and-structural-systems-division-73100/nist-aerodynamic-database/university-western (accessed 1.15.21).

Ho, E., Surry, D., Morrish, D., 2003b. NIST/TTU cooperative agreement - windstorm mitigation initiative: wind tunnel experiments on generic low buildings, BLWT-SS20-2003.

Ho, E., Surry, D., Morrish, D., Kopp, G.A., 2005. The UWO contribution to the NIST aerodynamic database for wind loads on low buildings: Part 1. Archiving format and basic aerodynamic data. J. Wind Eng. Ind. Aerodyn. 93, 1–30. https://doi.org/10.1016/j.jweia.2004.07.006

Holmes, J.D., 1980. Mean and fluctuating internal pressures induced by wind, in: Fifth International Conference on Wind Engineering. Elsevier, Fort Collins, Colorado, pp. 435–450. https://doi.org/10.1016/B978-1-4832-8367-8.50046-2

Jaffe, A.L., Kopp, G.A., 2021. Internal pressure modelling for low-rise buildings in tornadoes. J. Wind Eng. Ind. Aerodyn. 209, 104454. https://doi.org/10.1016/j.jweia.2020.104454

Kassab, A., 2021. Experimental study of tornado-induced pressures. (Ph.D. Dissertation) Western University Electronic Thesis and Dissertation Repository.

Kikitsu, H., Sarkar, P.P., Haan, F.L., 2011. Experimental study on tornado-induced loads of low-rise buildings using a large tornado simulator, in: 13th International Conference on Wind Engineering. Amsterdam.

Kopp, G.A., Wu, C.H., 2020. A framework to compare wind loads on low-rise buildings in tornadoes and atmospheric boundary layers. J. Wind Eng. Ind. Aerodyn. 204, 104269. https://doi.org/10.1016/j.jweia.2020.104269

Kosiba, K.A., Wurman, J., 2013. The three-dimensional structure and evolution of a tornado boundary layer. Weather Forecast. 28, 1552–1561. https://doi.org/10.1175/WAF-D-13-00070.1

Letchford, C.W., Levitz, B., James, D.L., 2015. Internal pressure dynamics in simulated tornadoes, in: Structures Congress 2015. American Society of Civil Engineers, Reston, Virginia, pp. 2689–2701.

Oh, J.H., Kopp, G.A., Inculet, D.R., 2007. The UWO contribution to the NIST aerodynamic database for wind loads on low buildings: Part 3. Internal pressures. J. Wind Eng. Ind. Aerodyn. 95, 755–779. https://doi.org/10.1016/j.jweia.2007.01.007

Razavi, A., Sarkar, P.P., 2021. Effects of roof geometry on tornado-induced structural actions of a low-rise building. Eng. Struct. 226, 111367. https://doi.org/10.1016/j.engstruct.2020.111367

Refan, M., Hangan, H., Wurman, J., 2014. Reproducing tornadoes in laboratory using proper scaling. J. Wind Eng. Ind. Aerodyn. 135, 136–148. https://doi.org/10.1016/j.jweia.2014.10.008

Refan, M., Hangan, H., 2018. Near surface experimental exploration of tornado vortices. J. Wind Eng. Ind. Aerodyn. 175, 120–135. https://doi.org/10.1016/j.jweia.2018.01.042

Roueche, D.B., Prevatt, D.O., Haan, F.L., 2020. Tornado-induced and straight-line wind loads on a low-rise building with consideration of internal pressure. Front. Built Environ. 6, 1–18. https://doi.org/10.3389/fbuil.2020.00018

St. Pierre, L.M., Kopp, G.A., Surry, D., Ho, E., 2005. The UWO contribution to the NIST aerodynamic database for wind loads on low buildings: Part 2. Comparison of data with wind load provisions. J. Wind Eng. Ind. Aerodyn. 93, 31–59. https://doi.org/10.1016/j.jweia.2004.07.007

Tecle, A.S., Bitsuamlak, G.T., Chowdhury, A.G., 2015. Opening and compartmentalization effects of internal pressure in low-rise buildings with gable and hip roofs. J. Archit. Eng. 21, 04014002. https://doi.org/10.1061/(asce)ae.1943-5568.0000101

Thomas, J.W., 1995. Numerical partial differential equations: finite difference methods, 1st ed. Springer-Verlag, New York.

Vickery, B.J., 1986. Gust-factors for internal-pressures in low rise buildings. J. Wind Eng. Ind. Aerodyn. 23, 259–271. https://doi.org/10.1016/0167-6105(86)90047-4

Vickery, P., Banik, S., Twisdale, L., 2020. Development of Tornado Design Criteria for Buildings and Shelters Subject to Tornado Induced Loads, in: NIST National Resilience Symposium. U.S. Department of Commerce, Gaithersburg, MD.

Wakimoto, R.M., Atkins, N.T., Wurman, J., 2011. The Lagrange Tornado during VORTEX2. Part I: Photogrammetric analysis of the tornado combined with single-Doppler radar data. Mon. Weather Rev. 139, 2233–2258. https://doi.org/10.1175/2010MWR3568.1

Wakimoto, R.M., Stauffer, P., Lee, W.C., Atkins, N.T., Wurman, J., 2012. Finescale structure of the Lagrange, Wyoming, Tornado during VORTEX2: GBVTD and photogrammetric analyses. Mon. Weather Rev. 140, 3397–3418. https://doi.org/10.1175/MWR-D-12-00036.1

Wang, J., Cao, S., Pang, W., Cao, J., 2018. Experimental study on tornado-induced wind pressures on a cubic building with openings. J. Struct. Eng. 144, 04017206. https://doi.org/10.1061/(asce)st.1943-541x.0001952

Chapter 3

3 Tornado Load Considerations for the Main Wind Force Resisting System of a Low-Rise Building

3.1 Introduction

Communities in Canada and the United States incur significant damage and economic loss due to tornadoes on an annual basis. The desire to improve community resilience against tornadoes, which was accelerated after the wave of severe tornado events in 2011 (NOAA, 2012), have caused a paradigm shift in the engineering community concerning the design of low-rise buildings to withstand tornado-induced wind loads (Prevatt et al., 2012a). From collected tornado data in the United States, 94% of tornadoes have been rated EF2 or less (NOAA, 2021) based on wind speed estimations from the Enhanced Fujita (EF) Scale (McDonald et al., 2006). Further, it has been shown that for severe tornadoes, such as the EF4 Tuscaloosa, AL and EF5 Joplin, MO tornadoes in 2011, over 80% of the structures in the tornado damage path experienced wind intensities of EF2 or less (Prevatt et al., 2012b). In light of this, Van De Lindt et al. (2013) proposed a dual-objective framework for the tornado-resilient design of buildings, where minimizing structural damage is the design goal for low-intensity tornadoes ranging from EF0 to EF2, while ensuring life safety (such as through the use of a tornado shelter or safe room) is the objective for stronger EF3 through EF5 tornadoes. This approach to minimize building damage for most tornado events is currently applied in tornado wind load provisions within the American Society of Civil Engineers (ASCE) building standards. The current standard, ASCE 7-16, contains tornado wind load recommendations within the commentary C26.14, which applies adjustment factors to the design wind pressures derived for atmospheric boundary layer (ABL) winds to estimate the tornado wind loads (ASCE, 2017). Further, the current draft of the ASCE 7-22 standard contains a new chapter for the treatment of tornado loads separate from ABL wind loads (ASCE, 2021).

Loads induced by ABL winds are a function of external pressures caused by wind-structure interaction effects and the internal pressure within the building. In contrast, tornado wind load studies (e.g. Haan, 2017; Roueche et al., 2020) have outlined that

tornado loads on a building are a function of the external aerodynamic pressures, the internal pressure within the building volume, and the atmospheric pressure drop (APD) found in the core of a tornado vortex. The presence of the APD has been confirmed by in-situ (Lee et al., 2004), computational (Nasir, 2017; Gairola and Bitsuamlak, 2019), and experimental observations (Mishra et al., 2008; Haan et al., 2010; Sabareesh et al., 2012; Refan et al., 2014). The differences between tornado and ABL wind load characteristics raises questions about the applicability of adapting the latter to derive tornado-induced load models (Peng et al., 2016; Kopp and Wu, 2020), which is the current methodology used in the ASCE 7 building standards. Mishra et al. (2008b) studied the simulated tornado loading on a cubic building model, highlighting the importance of the APD on tornado-induced loading while also demonstrating the differences in pressure magnitudes and distributions between tornado-induced and ABL winds. Hu et al. (2011) used particle-image velocimetry (PIV) to study the tornado flow field and its interaction with a low-rise gable roof building, showing that the mean flow field around the building is significantly different than the ABL-induced flow when the building is located near or within the vortex core.

Due to the differences in flow characteristics and aerodynamic effects on buildings between tornadoes and ABL winds, there has been an increased number of studies addressing the impact tornadoes have on the overall and local loads acting on the primary structural system of low-rise buildings. The bulk of this research initially focused on overall lateral and uplift loads for relatively small building models exposed to a tornado-like vortex (TLV) in physical simulators (Haan et al., 2008; Mayer, 2009; Sabareesh et al., 2012; Hangan, 2014; Wang et al., 2016). Haan et al. (2010) showed using a laboratory simulation on a sealed gable roof building that overall uplift loads exceed ABL wind loads calculated using the envelope method in ASCE 7-05 by a factor of 3, and lateral loads by a factor of 1.6. Haan (2017) analytically removed the APD from the same experimental data and found that the aerodynamic loading was closer to those calculated from ASCE 7, but still with local variations. Kopp and Wu (2020) found that the tornado wind field alters the local pressure distributions compared to ABL wind flow, but that it did not lead to substantial differences in the integrated wind forces when the aerodynamic and APD effects were separated. Wang and Cao (2021) studied the effect of net pressures on a cubic building with both distributed and dominant openings subjected to a scaled stationary

tornado, finding that the current tornado load provisions in ASCE 7-16 were able to conservatively evaluate the overall uplift and lateral base forces on the building without dominant openings while underestimating the uplift forces by 21% when a dominant opening is considered.

A limited number of studies have investigated the impact of tornado-induced winds on localized structural loading of low-rise buildings, such as on building frames or at critical member connections. Roueche et al. (2015) utilized tornado data from Haan et al. (2010) in combination with experimentally-determined structural influence functions for a one-third-scale, fully-sealed light-frame timber building to predict the structural reactions. For a peak full-scale tornado wind speed of 135 mph (i.e. EF2-rated tornado), peak vertical uplift tornado loads were found to be four-times greater than those predicted by ASCE 7-10 (although as much as 60% of this load could have been caused by the APD), while peak lateral forces were 1.8 times stronger for roof-to-wall connections and twice as strong for wall-to-foundation connections. Feng and Chen (2018) analyzed an interior moment frame for a perfectly sealed gable roof building and compared the results to ASCE 7-10, similarly finding that overall uplift on the frame was almost six-times larger under tornado-induced loading, while bending moments at the frame knees and ridge were underpredicted by ASCE 7-10. Razavi and Sarkar (2021) further investigated the lateral load, uplift, and bending moments on low-rise building frames with flat, gable, and hip roof geometries in a translating tornado. With respect to the gable roof geometry, their study showed that the tornado provisions of ASCE 7-16 underpredicts overall and local uplifts on a gable roof building by 41% and 55% respectively, underpredicts bending moments up to 9% for interior gable roof frames, and overpredicts overall lateral forces by up to 81%.

From the outlined literature on tornado loads on the main wind force resisting system (MWFRS), the following major observations can be made:

i) Uplift forces are highly dependent on the influence of the APD, which can cause significantly large uplift forces in the case of a perfectly sealed building. If the APD is analytically removed from the tornado loading or is equalized by the internal pressure, then the uplift loads fall closer to those caused by ABL winds.

ii) Lateral forces tend to be similar to those caused by ABL wind, but there is no consistent trend in terms of over- or under-exceedance as compared to loads from building codes and standards.

iii) Bending moments in building frames tend to exceed those induced by ABL winds, but the impact of net loading through the consideration of internal pressure has not been extensively studied.

The variance in the results of the studies discussed could be attributed to a variety of factors, including differing experimental simulators, tornado structures, scaling assumptions, tornado motions, consideration of internal pressure, choices for reference velocities, and evolutions in the building standards to which the results were compared, which are outlined in Table 3.1.

It is clear from the current research that there are significant differences in the structural loading induced by tornadoes versus ABL winds. However, there are several limitations and aspects of this body of literature that require further study:

i) Most of the studies outlined used aerodynamic data derived from relatively small-scale tornado simulators, which raises questions about their ability to replicate tornadic wind fields from nature (Baker and Sterling, 2019; Kopp and Wu, 2020), which will have a direct impact on the resulting structural loads.

ii) The majority of the current work considered only external tornado-induced loading rather than net loads determined through either direct measurement or numerical estimations of internal pressures.

Table 3.1: Summary of recent tornado experimental studies regarding overall structural loading and responses.

Reference	Tornado Motion	Swirl Ratio*	Building Model	Geometric Scale	Reference Velocity^{+}	Internal Pressure	Building Standard Comparison
Haan et al. (2010)	Translating (0.15 m/s to 0.61 m/s)	0.08 to 1.14	9.1 m x 9.1 m x 3.6 m, 35^{o} gable roof	1:100	Mean horizontal velocity at the building height of a stationary vortex	Not considered	ASCE 7-05
Roueche et al. (2015)	Translating (0.15 m/s)	0.08	12.2 m x 9.1 m x 2.4 m, 35^{o} gable roof	1:100	Peak 3-second gust velocity at the mean roof height in open exposure	Not Considered	ASCE 7-10
Feng and Chen (2018)	Translating (0.15 m/s to 0.61 m/s)	0.08	9.1 m x 9.1 m x 3.6 m, 35^{o} gable roof	1:100	Mean horizontal velocity at the building height of a stationary vortex	Not Considered	ASCE 7-10
Kopp and Wu (2020)	Translating (0.057 m/s)	0.76	13.8 m x 9.2 m x 4.0 m, 1.2^{o} gable roof	1:50	Simultaneous measurement of velocity components at 1.23 times the roof height	Not Considered (but APD is analytically removed from data)	N/A
Razavi and Sarkar (2021)	Translating (0.5 m/s)	0.85	18 m x 9 m x 3 m, 35^{o} gable roof, 35^{o} hip roof, and flat roof	1:100	Mean 3600-second wind speed, converted to a 3-second gust speed using the Durst Curve	Not directly measured, $GC_{P_i} = \pm 0.55$ was assumed	ASCE 7-16
Wang and Cao (2021)	Stationary	0.15 to 0.72	150 m x 150 m x 150 m, flat roof	1:3000	Maximum time-averaged horizontal velocity at model height	Considered: enclosed and partially enclosed configurations	ASCE 7-16

**Swirl ratio definition varies depending on the study. It is used here to give a sense of the range of tornado-like vortices studied.*

$^{+}$All reference velocities were measured at the building location, without the presence of the building.

iii) Many studies compared global tornado-induced structural loads to the loads derived from building codes and standards, with limited direct comparisons made with loading derived from ABL aerodynamic data under different opening configurations, as was done by Roueche et al. (2020) to assess differences in localized mean and peak pressures. Further, in light of the proposed tornado wind load chapter in ASCE 7-22, it would be useful for the engineering community if an independent analysis and comparison of the tornado-induced structural loads from experimental tornado tests and the ASCE provisions was conducted.

In an attempt to address these gaps, there are two objectives of the analysis conducted in this chapter. The first is to evaluate the differences in tornado and ABL wind-induced structural loads for the design of the MWFRS of a single low-rise, gable roof building with consideration of internal pressure. The second objective is to assess the ability of tornado load provisions in building codes, specifically the proposed tornado load provisions in ASCE 7-22, to determine suitable loads for the tornado-resistant structural design of low-rise buildings. Tornado wind load data was obtained from experiments conducted at the WindEEE Dome facility, which were compared to both ABL wind loads obtained from the National Institute of Standards and Technology (NIST) aerodynamic database and the tornado design loads derived from ASCE 7-22. The external pressure data was coupled with a numerical model for internal pressure to determine net pressures acting on the building. Three building envelope opening configurations, corresponding to a perfectly sealed, enclosed, and partially enclosed structure, were considered for the comparison of net loads. In the section “External Wind Pressure Data”, the tornado external pressure measurement and ABL aerodynamic database will be briefly described, with mean pressure distribution results displayed. The internal pressure model is outlined in the “Internal Pressure” section. It should be noted that the prior two sections described are discussed in detail within Chapter 2 of this thesis. The section “Structural System Analysis” describes the methodology for obtaining the structural wind load responses. The structural actions from each wind load source will be analyzed in the “Results and Discussion” section, and a summary of the major findings is provided in the “Conclusion”.

3.2 External Wind Pressure Data

3.2.1 Tornado External Pressures

External tornado pressures were measured on a gable roof building model using the WindEEE Dome facility at Western University, which can simulate tornado-like vortices (TLVs) with various flow characteristics and at translation speeds up to 1.5 m/s over a distance of 4.6 m. Note that the terms "TLV" and "tornado" are used interchangeably in this chapter for conciseness and ease of reading. One tornado structure with a swirl ratio ($S = \frac{r_0 \Gamma_{max}}{2Qh}$) of 0.76, core radius ($R_C$) of 0.60 m, aspect ratio ($a = \frac{h}{r_0}$) of 0.35, and radial Reynolds number ($Re_r = \frac{Q}{2\pi\upsilon}$) of 10^6 was simulated, where r_0 is the updraft radius, h is the inflow depth, Γ_{max} is the maximum circulation in the flow, Q is the flow rate per unit axial length, υ is the kinematic viscosity, and ρ is the density of air. For the simulated tornado with these characteristics, it has been noted by Kopp and Wu (2020) as well as Refan and Hangan (2018) that the TLV is two-celled, with multiple sub-vortices surrounding the central vortex core. Further, by assuming a geometric length scale, $\lambda_{L,TLV}$, of 1:200, the simulated vortex had a scaled wind field that closely resembled the 2009 Goshen County, Wyoming V3 full-scale tornado record (Wakimoto et al., 2012; Refan et al., 2014). A high-frequency pressure integration (HFPI) gable roof building model was developed with model-scale plan dimensions of 191 mm by 122 mm, an eave height of 61 mm, and roof pitch of 3:12 (14.4°), as shown in Figure 3.1(a). The building model was outfitted with 360 pressure taps and was mounted on a 1118 mm diameter base plate, which contained 120 radially distributed taps to measure ground surface pressures. Three test cases, shown schematically in Figure 3.1(b), were considered for the tornado pressure analysis corresponding to a vortex translation speed of approximately 1.5 m/s, smooth surrounding terrain, and three building orientations, θ, of 0°, 45° and 90°. In all three test cases, the vortex took a curved trajectory and translates past the building model at a distance approximately equal to R_C (i.e. 0.6 m) due to velocity and pressure imbalances.

(a)

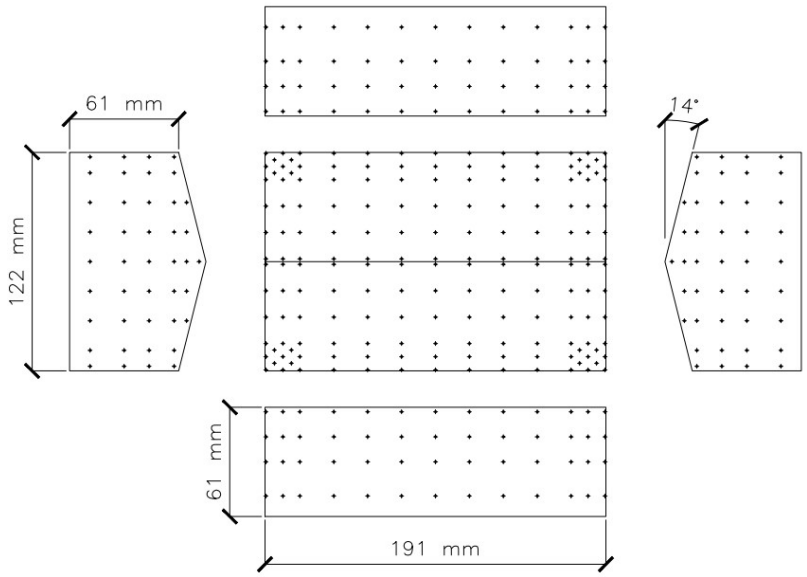

(b)

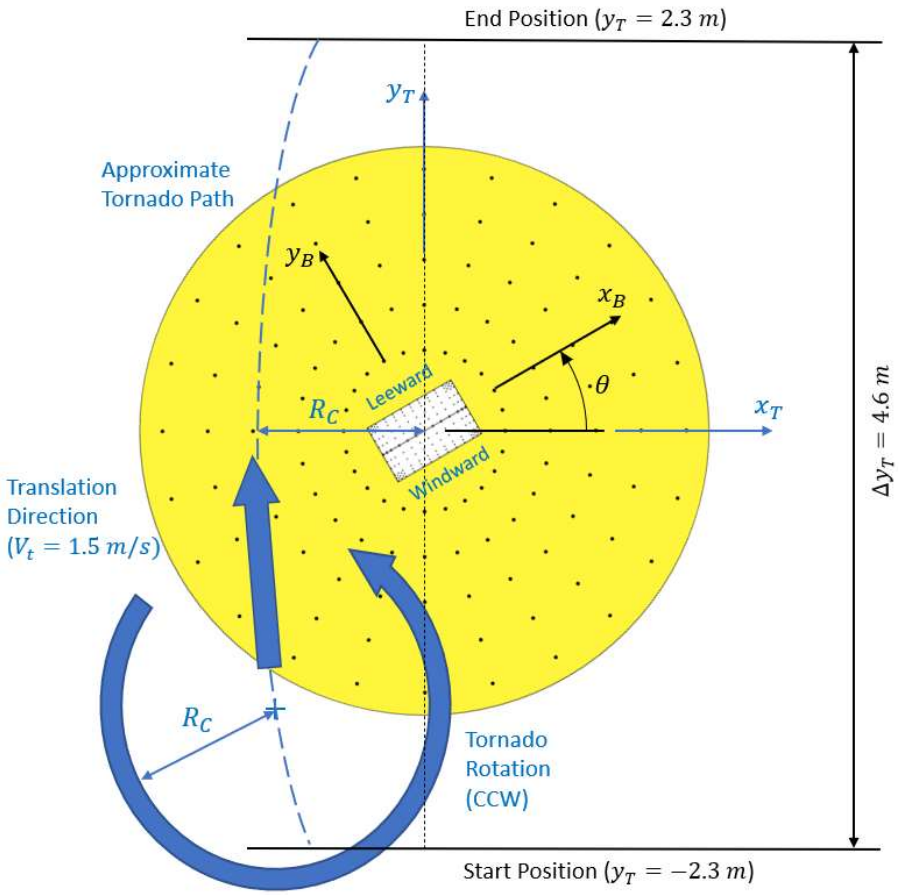

Figure 3.1: (a) Pressure tap layout for the WindEEE test building model. (b) Test schematic for a translating tornado in the WindEEE Dome.

Pressure measurements were obtained at a sampling frequency of 500 Hz for a duration of 15 seconds, with 10 repeated runs conducted for each building orientation. The obtained time series of external pressures, $p_e(t,\theta)$, were non-dimensionalized using pressure coefficients, $C_{Pe,TLV}(t,\theta)$, which were defined in Equation 3.1 as follows:

$$C_{Pe,TLV}(t,\theta) = \frac{p_e(t,\theta) - p_0}{\frac{1}{2}\rho V_{ref,TLV}^2} \tag{3.1}$$

where p_0 is the ambient pressure measured outside of the test chamber, ρ is the density of air, and $V_{ref,TLV}$ is the reference velocity, defined herein as the peak 3-second gust (in full-scale time) horizontal velocity at the mean roof height, h, measured at the location of the building in a separate empty chamber test (i.e. $V_{ref,TLV} = \hat{V}_{TLV}(h)$). The reference velocity was determined to be 16.3 m/s using wind speed data measured by Kassab (2021). Assuming that the reference full-scale 3-second gust velocity was equivalent to the upper limit of an EF1 tornado (i.e. 49.2 m/s), the velocity scale ($\lambda_{V,TLV}$) was computed to be 1:3.0. A profile of the peak vertical profile of horizontal velocity, $\hat{V}(z)$ is shown in Figure 3.2.

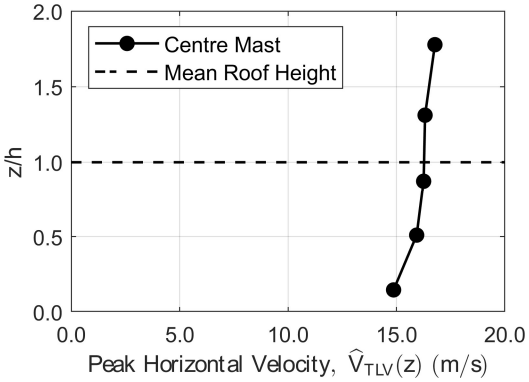

Figure 3.2: Vertical profile of peak gust horizontal velocities measured at the centre of the WindEEE Dome chamber.

3.2.2 ABL Wind External Pressures

In the early 2000's, an ABL wind aerodynamic database was developed under a cooperation between NIST and the Alan G. Davenport Boundary Layer Wind Tunnel Laboratory for low-rise, gable roof buildings of various dimensions located in different

terrain exposures (Ho et al., 2005). From this database, "Building 3" was selected for analysis as shown in Figure 3.3, which at a length scale, $\lambda_{L,ABL}$, of 1:100 had model-scale plan dimensions of 382 mm by 244 mm, an eave height of 122 mm, and a roof pitch of 3:12 (14.4°). Wind pressure data utilized from the database corresponded to building orientations, θ, ranging between 180° to 345° in 15° increments, and building symmetry was invoked to simulate pressure data for wind angles between 0° and 165°. 677 pressure taps were distributed over the walls and roof of the building model. Only aerodynamic data from open terrain (i.e. roughness length, z_0, of 0.03 m) was used in the analysis, with the corresponding mean velocity and turbulence intensity profiles shown in Figure 3.7.

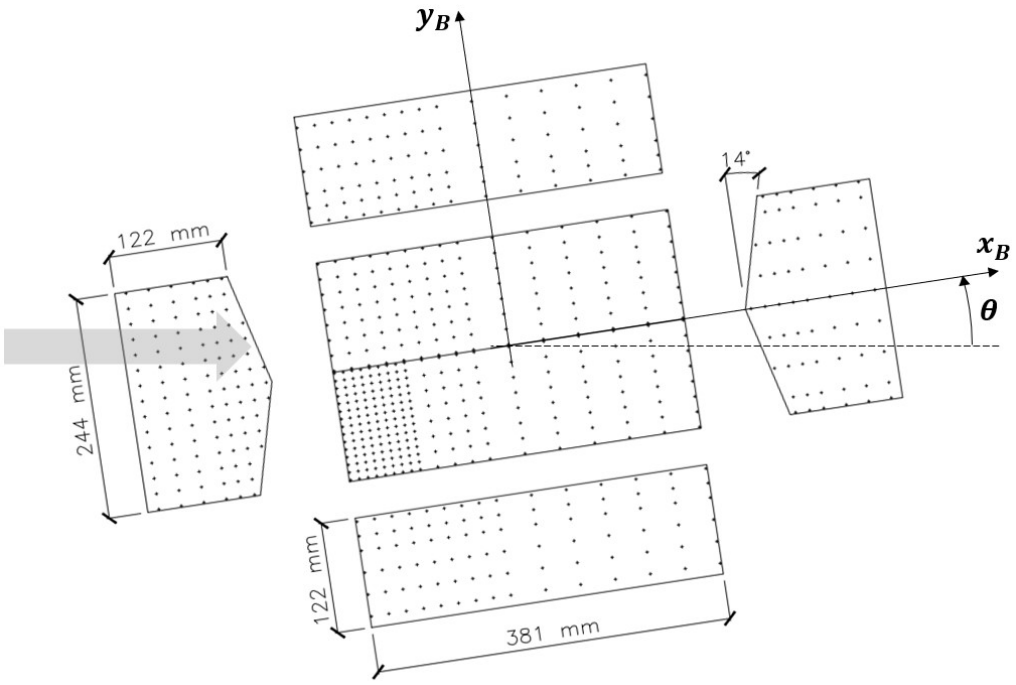

Figure 3.3: Layout of the "Building 3" model from the NIST ABL wind aerodynamic database. The grey arrow indicates the inflow ABL wind direction.

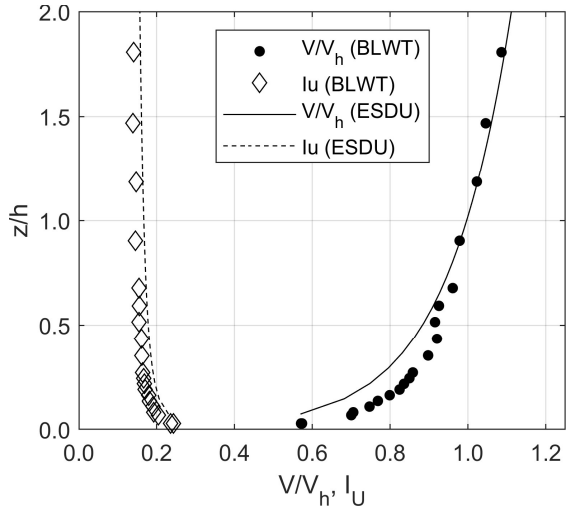

Figure 3.4: Comparison of the simulated mean wind speed and turbulence intensity in the Western University BLWT II to the Engineering Science Data Unit (ESDU) profiles for open exposure terrain (Ho et al., 2003).

External pressure data, $p_e(t,\theta)$, was collected over a time period of 100 seconds at a sampling frequency of 500 Hz and was non-dimensionalized as external pressure coefficients, $C_{Pe,ABL}(t,\theta)$, in accordance with Equation 3.2:

$$C_{Pe,ABL}(t,\theta) = \frac{p_e(t,\theta) - p_0}{\frac{1}{2}\rho V_{ref,ABL}^2} \tag{3.2}$$

where p_0 is the reference static pressure and V_{ref} is the mean hourly (i.e. 3600 seconds in full-scale time) wind velocity referenced to the mean roof height of the model. The velocity scale of the database, $\lambda_{V,ABL}$, was assumed to be 1:2.8 so that each 100-second wind tunnel record for a given building orientation represents a one-hour storm at full scale.

The full-scale building dimensions from both the WindEEE and NIST wind tunnel tests were identical, thus enabling a comparison between the two. In order to directly compare the external aerodynamic data between these two tests, adjustments were required to address compatibility issues related to the reference velocity and tap distribution. The standard reference velocity used for defining equivalent external pressure coefficients, $C_{Pe,eq}$, in this study was a 3-second gust horizontal velocity at mean roof height in open

terrain, $V_{3\ s,h,open}$. Since the tornado pressure coefficients were originally referenced to a 3-second gust velocity, $C_{Pe,eq}(t,\theta) = C_{Pe,TLV}(t,\theta)$ for the WindEEE data. In contrast, the NIST aerodynamic database pressure coefficients were referenced to a mean hourly wind speed at the mean roof height in open terrain, so they needed to be converted to a 3-second gust velocity. This averaging time adjustment was made using the Durst Curve (Durst, 1960). In order to account for the new reference wind speed, a wind tunnel factor, $F_{WT,NIST}$, defined by St. Pierre et al. (2005) was used to modify the NIST external pressure coefficients from their original form, $C_{Pe,ABL}$, to the equivalent form:

$$C_{Pe,eq}(t,\theta) = F_{WT,NIST} * C_{Pe,ABL}(t,\theta) = \left(\frac{V_{3600\ s,h,open}}{V_{3\ s,h,open}}\right)^2 * C_{Pe,ABL}(t,\theta) \qquad (3.3)$$

In this case, the resulting wind tunnel factor was equal to 0.43, with no further adjustments needed to account for differences in terrain or wind speed reference heights between the two tests. With respect to tap density, the NIST aerodynamic pressures were interpolated and resampled to match the tap layout from the WindEEE Dome model using the Nearest-Neighbour interpolation scheme and implemented through the "*scatteredInterpolant*" function in MATLAB (Amidror, 2002).

3.2.3 Mean External Pressure Distributions

A comparison of the exterior mean pressure distributions on the low-rise building between ABL and tornado wind fields is useful at this stage to illustrate the differences in fluid-structure interactions between the two flow regimes. As a common convention in wind engineering, a positive pressure coefficient indicates that the wind pressure is acting towards the surface (commonly referred to as a pressure load) while a negative coefficient indicates the wind pressure is directed away from the surface (referred to as a suction load). Figure 3.5 and Figure 3.6 depict the mean ground and building exterior pressure coefficients for the tornado-like wind flow measured at the WindEEE Dome. The mean of the translating tornado-induced pressures was obtained at six tornado positions along the y-axis of the simulator, denoted y_T, which are normalized by R_C. The mean external pressure distributions were calculated by ensemble-averaging pressures between positions of $y_T - 0.1R_C$ to $y_T + 0.1R_C$ over all 10 repeated runs for each building θ. The tornado

core location was determined using the bellmouth position as a reference with an offset applied to account for a vortex tilt of approximately 18^{o}, which is in line with observations of the same simulated vortex from Kassab (2021). It should be noted that phenomenon of vortex wandering was not addressed when computing the pressure distributions. For most tornado positions, the effective wind angle of attack changed rapidly with vortex position and typically produced a "cornering" wind load case, with a quick transition period in wind direction as the tornado core passed by the building. Further, the external pressures were negative due to the APD that was present in the core of the tornado, which can be seen from the ground pressure profiles. The highest mean suction pressures were observed at the roof edge and corner regions. There are also high suction pressure regions on the leeward walls, which could have been induced by the curvature of the tornadic wind field. In contrast, the mean wind pressure distribution under ABL winds is provided in Figure 3.7 for building orientations of 180^{o}, 225^{o}, and 270^{o}. The mean pressure distribution was symmetric when the wind direction was normal to the windward building surface, while the highest mean suction pressures were associated with cornering wind cases, as shown for $\theta = 225^{o}$ in Figure 3.7. Further, the inflow wind was assumed to be stationary for each building orientation, simplifying the process for obtaining design wind loads.

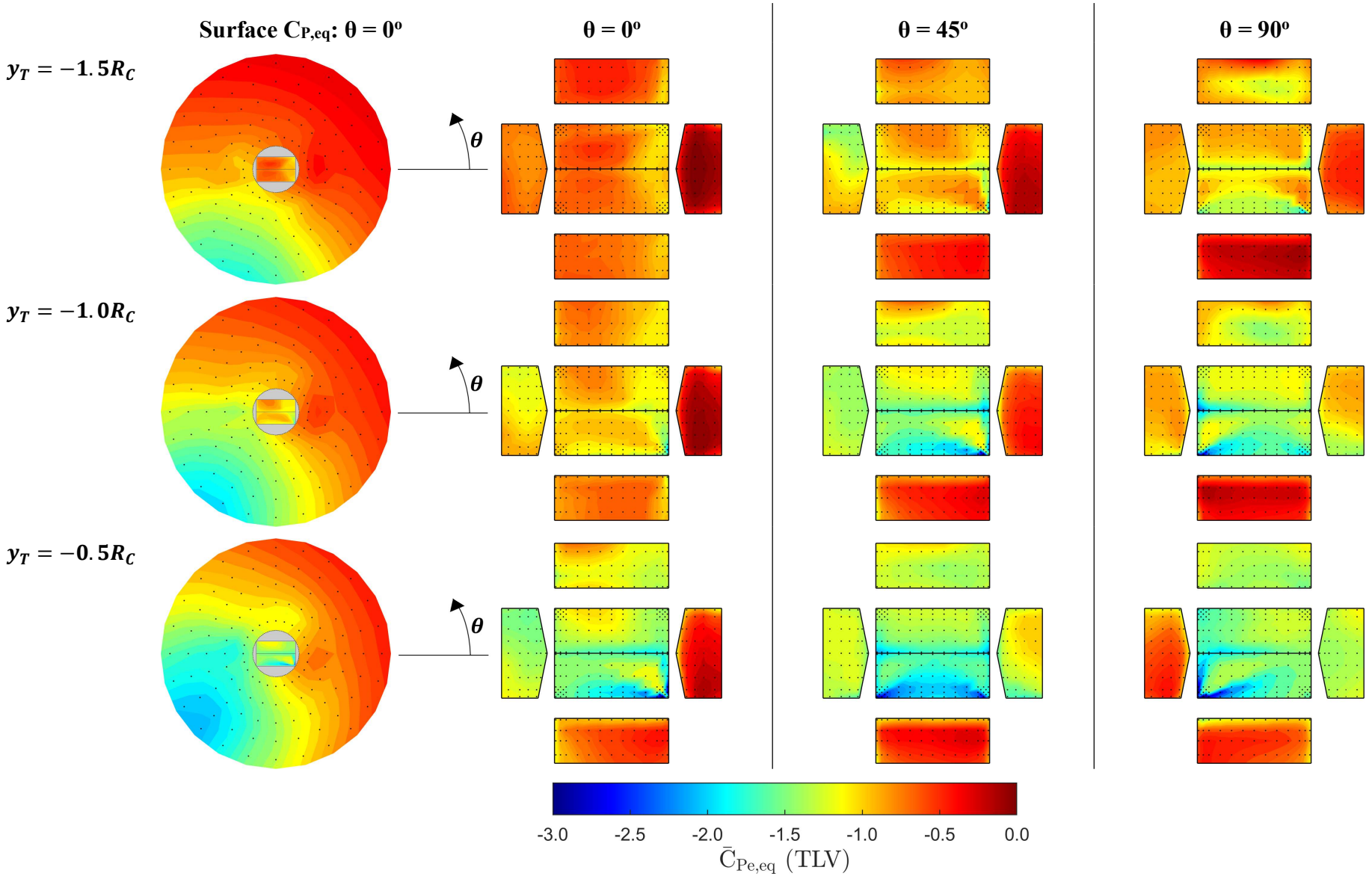

Figure 3.5: Ensemble-averaged ground surface pressures and external building pressures for building orientations of 0°, 45°, and 90° at tornado positions, y_T, of -1.5R_C to -0.5R_C.

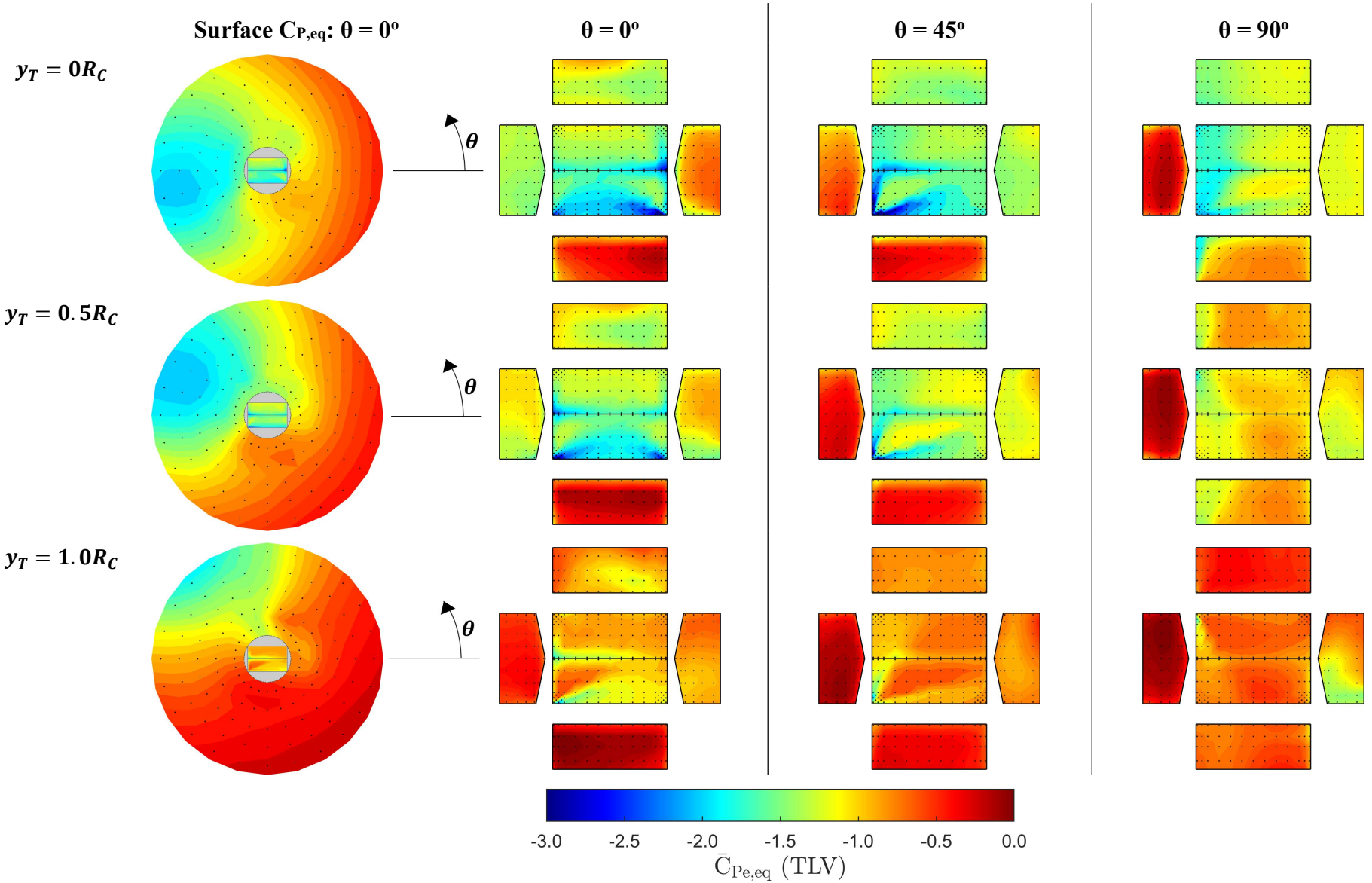

Figure 3.6: Ensemble-averaged ground surface pressures and external building pressures for building orientations of 0°, 45° and 90° at vortex positions, y_T, of $0R_C$ to $1.0R_C$.

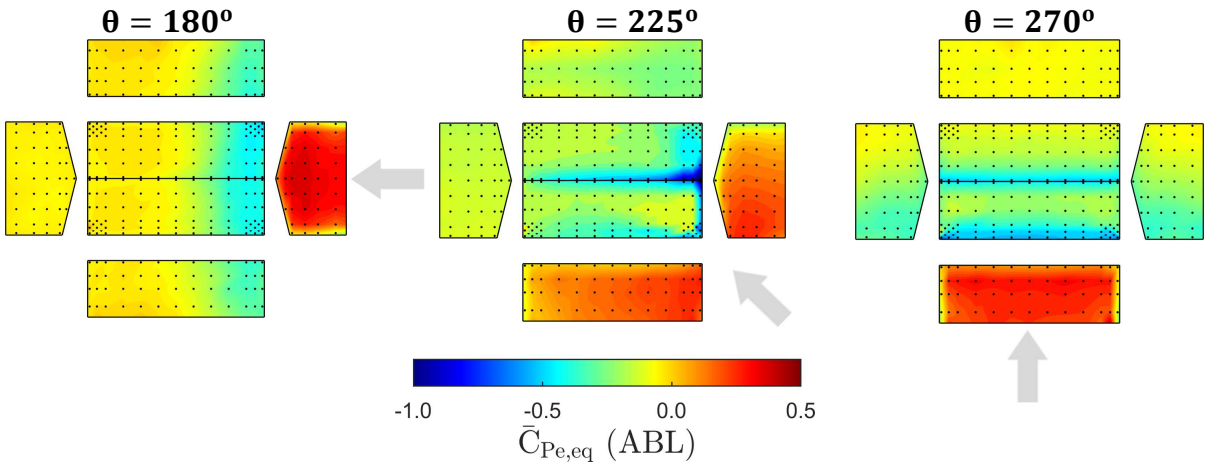

Figure 3.7: Mean external pressure distributions for the resampled NIST ABL wind data at building orientations, θ, of 180°, 225°, and 270°, with the tap layout matching the WindEEE building model. The grey arrow indicates the inflow ABL wind direction.

3.3 Internal Pressure

Three opening cases were assumed over the building envelope to determine internal pressures, corresponding to the definitions provided in the proposed ASCE 7-22 for a perfectly sealed building, enclosed building, and partially enclosed building (ASCE, 2021), with details provided in Table 3.2 and schematically in Figure 3.8. For the enclosed building, 80 holes were distributed over the walls and roof of the building, while the dominant opening dimensions and position utilized to represent a partially enclosed building were the same as those used in the NIST database by Oh et al. (2007) for models of comparable dimensions. The leakage induced by the distributed openings was also assumed to be present with the dominant opening for the partially enclosed configuration.

Table 3.2: Summary of the internal pressure opening cases for the low-rise building.

Opening Description	Dimensions (Full-Scale)	Porosity Ratio*
Perfectly Sealed	No openings	0 %
Enclosed	80 holes, $d = 0.202$ m	0.1 %
Partially Enclosed	8.13 m x 1.91 m (L x W)	3.3 %

** Porosity Ratio corresponds to the opening area divided by the corresponding building surface area.*

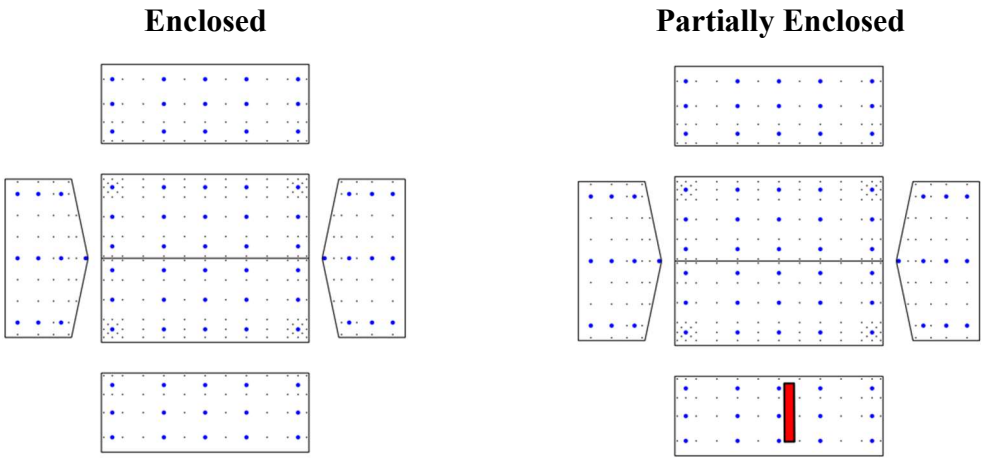

Figure 3.8: Schematics of the enclosed opening case with 80 holes distributed over the building walls (indicated by the blue dots) and the partially enclosed case with an 8.13 x 1.91 m dominant opening on the predominantly windward face of the building (shown by the red rectangle).

The internal pressures for the different opening configurations needed to be estimated using a numerical model since they were not directly measured in either the tornado or ABL wind tunnel tests. In this case, the Multiple Discharge Equations (MDE's) for unsteady, incompressible flow were used to simulate the internal pressures for both the enclosed and partially enclosed opening cases, which is based on the conventional Helmholtz Resonator model (Holmes, 1980). The MDE's or similar models have been successfully utilized in the past to estimate internal pressures in synoptic wind flow (Vickery, 1986; Oh et al., 2007; Tecle et al., 2015) and non-synoptic tornado winds (Roueche et al., 2020; Jaffe and Kopp, 2021). Time histories of net pressure coefficients, $C_{P,eq}(t,\theta)$, required for the analysis were computed from the external and internal pressure coefficients as follows:

$$C_{P,eq}(t,\theta) = C_{Pe,eq}(t,\theta) - C_{Pi,eq}(t,\theta) \tag{3.4}$$

There were significant differences in the internal pressures induced by tornado versus ABL winds. Figure 3.9 shows a comparison between the ensemble-averaged internal pressures in an enclosed versus partially enclosed building exposed to tornado

winds at the WindEEE Dome for all three building orientations. The internal pressure for an enclosed building was found to drop as the tornado passed by the building, which can be attributed to the APD near the core of the vortex (Sabareesh et al., 2012; Letchford et al., 2015; Roueche et al., 2020; Kassab, 2021). For the case of a partially enclosed structure with a dominant opening, the internal pressure rose relative to the enclosed building case when the resultant wind direction was impinging on the windward wall containing the opening. Once the opening was on the sidewall or leeward side of the building relative to the tornado flow, the internal pressure dropped back down in line with the enclosed building internal pressure, which was behaviour consistent with findings from literature (Letchford et al., 2015; Wang et al., 2018; Sabareesh et al., 2019; Roueche et al., 2020). It was also observed that the time histories of internal pressure for a partially enclosed building varied significantly with respect to the tornado position depending on the building orientation.

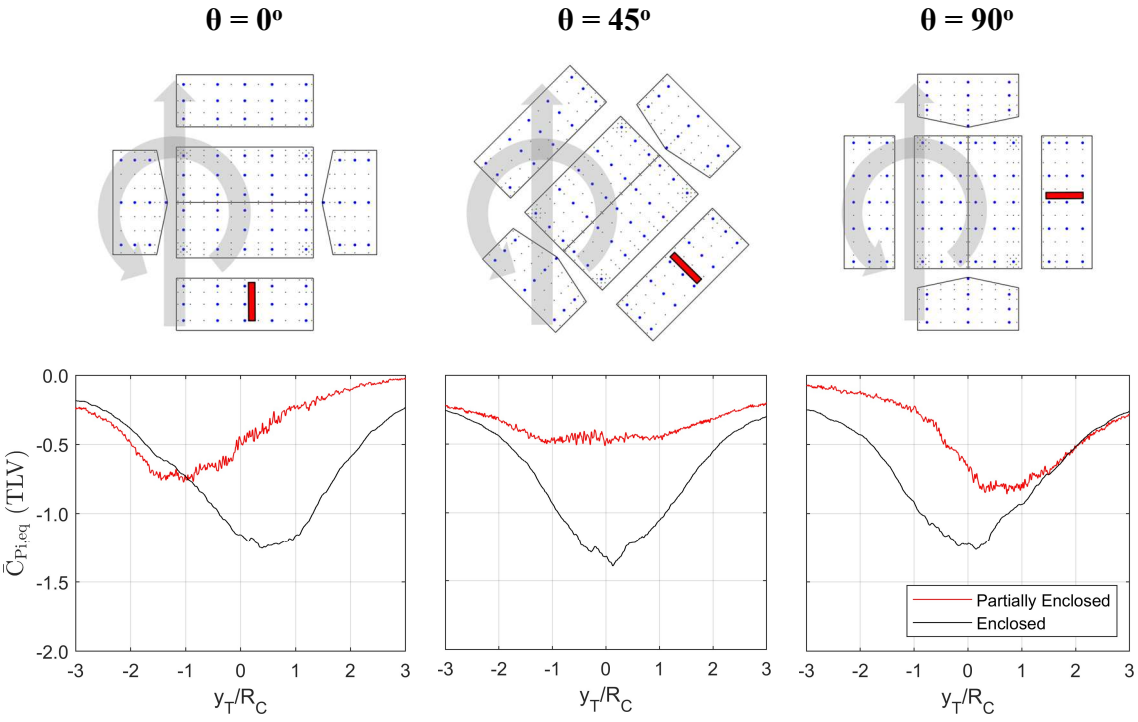

Figure 3.9: Comparison between ensemble-averaged tornado internal pressures between the enclosed and partially enclosed opening configurations.

Figure 3.10 depicts the mean and peak internal pressure coefficients for the ABL wind cases. The peak internal pressures were estimated using the "*maxminest*" MATLAB

function developed by the NIST statistical engineering division (Main, 2011) and derived from the theory outlined in Sadek and Simiu (2002), which corresponds to a 57.7% non-exceedance probability from the Type-I (Gumbel) Extreme Value distribution. Unlike the tornado-induced internal pressures, the ABL-induced internal pressures were stationary with a mean that varies with building orientation, but not with time. For the enclosed building, the magnitudes of internal pressure were slightly negative and did not vary significantly with respect to building orientation. This is in strong contrast to the tornado-induced internal pressures for an enclosed building, which dropped significantly as the core passed by the structure. When considering a partially enclosed building with a dominant opening, the internal pressure varied significantly depending on the wind direction. In this case, the internal pressure coefficient reached a maximum mean of 0.3 and peak of around 1.0 when the dominant opening was directly exposed to the wind inflow and dropped to a mean of -0.1 and minimum peak of -0.6 when the opening was located on the side or leeward walls. These observations are similar to the tornado internal pressures for a partially enclosed building, which were the largest as the inflow wind direction was in-line with the opening.

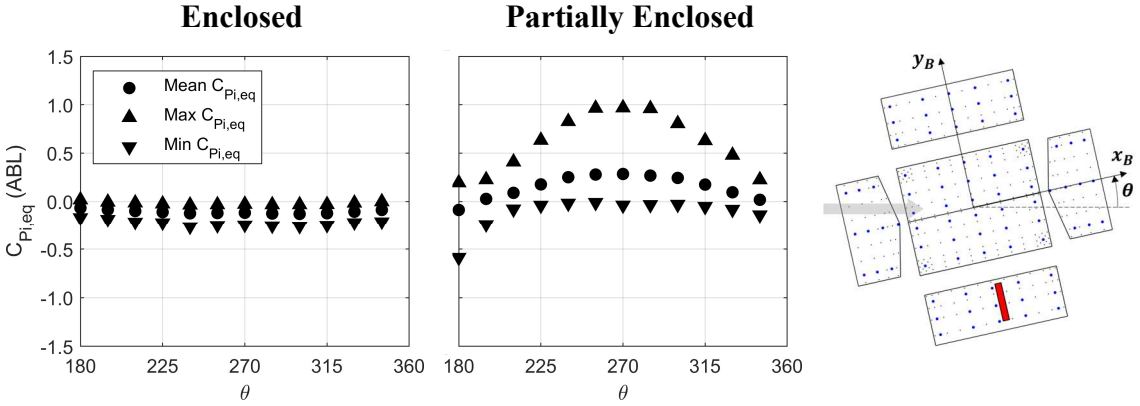

Figure 3.10: Mean and peak internal pressure coefficients under ABL wind flow as a function of building orientation for the enclosed and partially enclosed building opening cases.

3.4 Main Wind Force Resisting System (MWFRS) Analysis

3.4.1 Structural Model Description and Assumptions

To analyze the MWFRS of the selected low-rise building model, assumptions had to be made pertaining to the structural system. The structural form utilized herein resembled the system utilized in Main and Fritz (2006), which is representative of a typical steel-framed commercial building. Since the building was a low-rise with a natural frequency ≥ 1 Hz, it was classified as a "rigid" structure (ASCE, 2021), thus meaning that structural response at each time step was linear-static with negligible dynamic effects.

As shown in Figure 3.11, the primary system consisted of frames, spaced at 7.6 m (25 ft), spanning the building width, with the columns of the frames pin-connected at their base. Girts and purlins, referring to cross-members on the walls and roof respectively (but referred to jointly as purlins herein for conciseness), spanned between the primary frames at a spacing of 1.5 m (5 ft). Roof and wall panels (commonly referred to as cladding panels), which form the exterior envelope of the building, were attached to the purlins. A series of simplifying assumptions applied to the structural model were made as follows:

- Only the frames were explicitly modeled, with the purlins and cladding panels not included.
- Responses to loads along the x_B–axis (i.e. parallel to the roof ridge) were not considered.
- The coupling between frames introduced by the cladding system was neglected.

Since the purlins and cladding elements were not included in the model, the load path for the wind pressures needed to be accounted for to determine the correct load distribution on the frames. The wind pressures were applied normal to the cladding panels. The cladding acted as a one-way system (due to panel ribs that are aligned perpendicular to the purlins) to transfer the load to the purlins, which then carry the load to the frames. The connections between the cladding panels and purlins as well as between the purlins and frames were assumed to be hinged. The load sharing and structural responses were calculated assuming that the building will remain intact when exposed to either tornado or ABL wind loads.

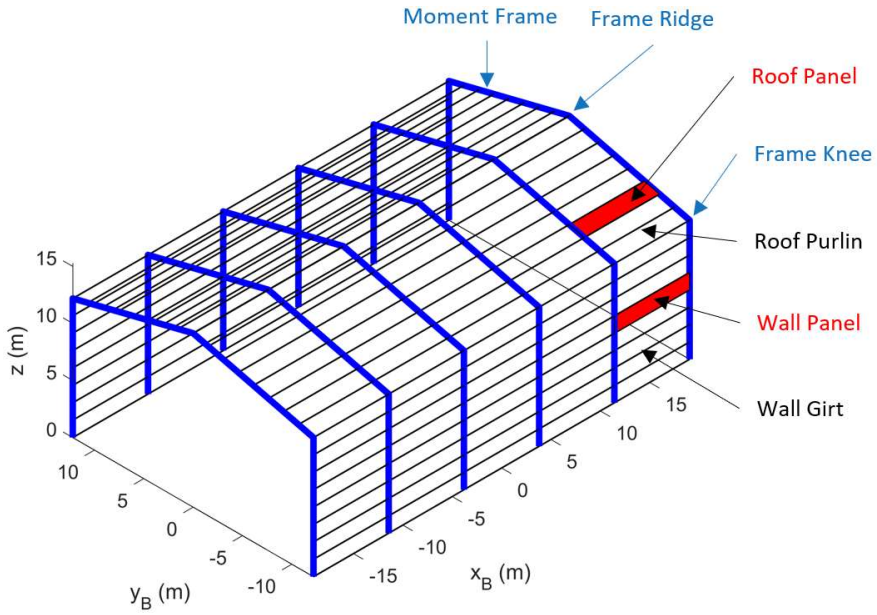

Figure 3.11: Structural system layout for the gable roof building model.

3.4.2 Structural Actions and Load Coefficients

Seven structural responses were computed to envelope the major structural actions important to the design of the MWFRS of low-rise buildings with uniformly spaced frames (ASCE, 2017). The selected structural responses and their load coefficients were similar to the definitions employed by St. Pierre et al. (2005) and were analyzed by bay or frame location as shown in Figure 3.12.

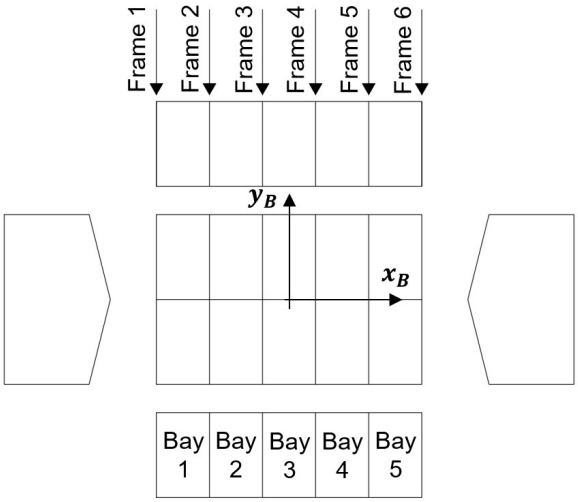

Figure 3.12: Plan view of building model with frame and bay definitions.

Two area-averaged global actions were calculated, which do not depend on any structural system since they act on bay areas between the frames. The area-averaged load response coefficients were determined by integrating the pressure time series at each tap location weighted by the ratio of the tap tributary area to the total projected area being considered. The time series of uplift coefficients at each building bay for a given building orientation, $C_Z(t,\theta)$, was the projected vertical component of the wind load acting on the building roof as defined by Equation 3.5.

$$C_Z(t,\theta) = \frac{\sum_{i=1}^{m} l_i w_i C_{P,eq,i}(t,\theta)\, cos\beta_i}{WB} \tag{3.5}$$

The lateral force coefficient at each bay acting along the y_B–axis of the building, $C_Y(t,\theta)$, was the net lateral force acting on opposite planes of the structure, including the horizontal projection of the roof, which is calculated using Equation 3.6.

$$C_Y(t,\theta) = \frac{\sum_{i=1}^{m} l_i w_i C_{P,eq,i}(t,\theta) sin\beta_i}{H_R B} \tag{3.6}$$

In these two equations for the area-averaged responses, l_i and w_i are the tributary length and width associated with each pressure tap, i, located within each bay, $C_{P,eq,i}(t,\theta)$ is the net pressure coefficient time series associated with each tap i, W is the building width (24.4 m), B is the bay width (7.6 m), and H_R is the ridge height (15.2 m). β_i is the angle between a vector normal to the building surface associated pressure tap i and the z–axis, depicted in Figure 3.13 with the positive direction defined as counter-clockwise form the z-axis.

Five bending moment response coefficients were calculated for each frame, covering two major types of structural systems: the moments at the ridge and both knees of a frame pinned at its base (referred to herein as a two-pin frame for conciseness), and the moments at the frame knees for a frame pinned at both its base and its ridge (referred to as a three-pin frame). Moment responses were computed using the "*windPRESSURE*" MATLAB-based program (Main, 2005) and modified into non-dimensional coefficients by combining the response equations from Main and Fritz (2006) and St. Pierre et al. (2005):

$$C_{M,j}(t,\theta) = \frac{\sum_{k=1}^{n}\sum_{i=1}^{m} N_k^j A_{ik} C_{P,eq,i}(t,\theta)}{W^2 B} \tag{3.7}$$

where N_k^j is the influence coefficient that represents the bending moment at cross section j of each frame due to a unit force applied at the k-th purlin attachment point to the frame, A_{ik} specifies how the surface pressure applied over the tributary area of tap i is distributed to the k-th attachment point, B is equal to 7.6 m for the end frames or 15.2 m for the interior frames (which identifies the width contributing to the moment response on a particular frame), and all other terms were previously defined. Figure 3.13 demonstrates the influence coefficient concept, with the arrows indicating the relative magnitude of a moment response caused by a unit load applied at a particular location on the frame. The N_k^j values were computed using stiffness matrix methods. The three-pin frame is a determinant frame, so the moment responses are independent of the stiffness properties. However, to calculate the moment influence coefficients for the two-pin frame, the stiffness of the frame girders relative to the frame columns was assumed to be unity, as was done in St. Pierre et al. (2005). In order to maintain this ratio, the ratio of the girder moment of inertia, I_g, to the column, I_C, was taken as the ratio of the building width to eave height, meaning $\frac{I_g}{I_c} = 2.0$.

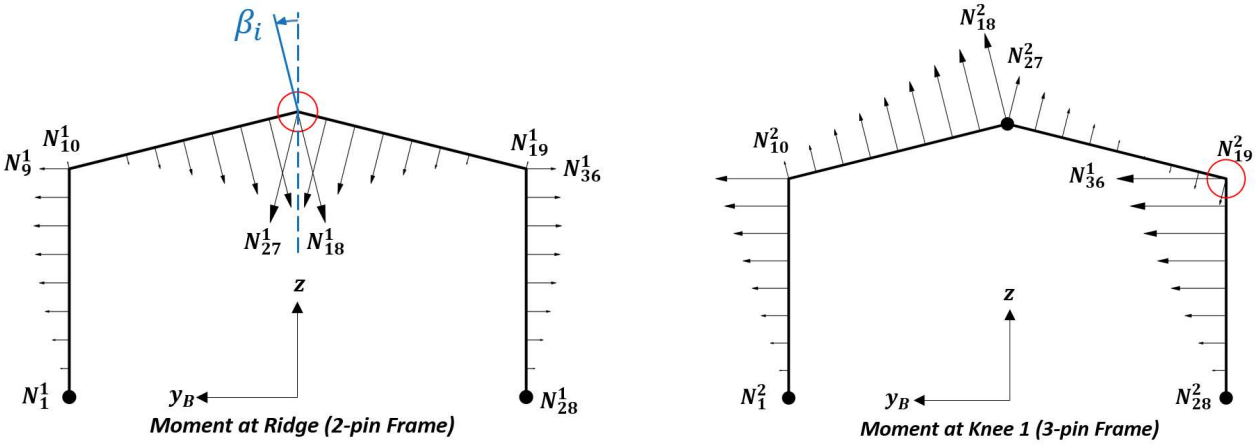

Figure 3.13: Cross sections of the moment frames and influence coefficients for the moment at the ridge of the two-pin frame and the moment at the knee of the three-pin frame system. An arrow pointing towards the centre of the building indicates a positive N_k^j value.

Statistical methods were utilized for the estimation of the peak load coefficients, which provide more stable peak values than using the observed maxima or minima from a time series. For the WindEEE tornado test data, the peak uplift, lateral, or moment coefficient for a given building orientation, denoted generally as $\hat{C}_{TLV}(\theta)$, were defined by Equation 3.8:

$$\hat{C}_{TLV}(\theta) = \underset{r=1..10}{\text{median}}\, \hat{C}_{r,TLV}\,(\theta) \tag{3.8}$$

where $\hat{C}_{r,TLV}(\theta)$ is the ordered set of the peak observed uplift, lateral, or moment coefficients for each tornado translation run, r. The peak uplift, lateral, or moment coefficients from the ABL wind data, $\hat{C}_{ABL}(\theta)$, were estimated using a Type I (Gumbel) Extreme Value distribution, which takes the following form:

$$\hat{C}_{ABL}(\theta) = F(C_{ABL}(\theta) = 0.577) \tag{3.9a}$$

$$F\big(C_{ABL}(\theta)\big) = exp\left(-exp\left(-\frac{C_{ABL}(\theta) - \mu_g}{\beta_g}\right)\right) \tag{3.9b}$$

where μ_g is the location parameter and β_g is the scale parameter. These parameters were obtained using the general translation method proposed by Sadek and Simiu (2002) which was implemented using the NIST "*maxminest"* MATLAB function developed by Main (2011). In this study, $\hat{C}_{ABL}(\theta)$ was taken as the mean of the Gumbel Distribution, which corresponds to a 57.7% non-exceedance probability, for a full-scale storm duration of one hour (i.e. meaning an assumed duration ratio of 1.0). The subsequent sections compare enveloped peak load coefficients. In the case of the tornado loads, this meant enveloping the set of peak load coefficients, $\hat{C}_{TLV}(\theta)$, over the three building orientations with measured data (0°, 45°, and 90°) and the building orientations with reflected data (180°, 225°, and 270°), For the ABL winds, $\hat{C}_{ABL}(\theta)$ corresponded to enveloping the peaks over the original building orientations (180° to 345°) and reflected orientations (0° to 165°). Schematics of the enveloping assumptions are shown in Figure 3.14 for both the tornado and ABL flows, with the additional consideration of the reflected dominant opening for the partially enclosed building also depicted.

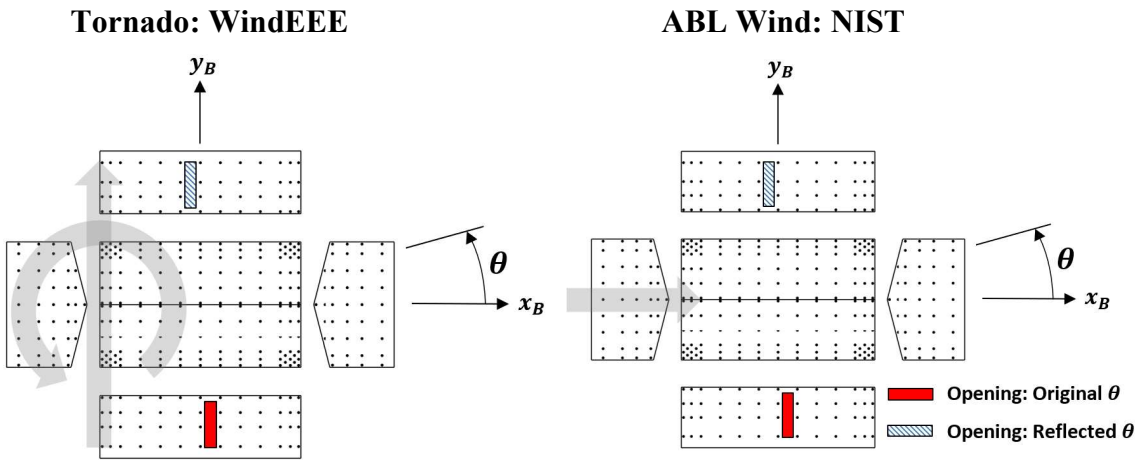

Figure 3.14: Diagram showing position of dominant opening for original (i.e. measured) and reflected building orientations for determining enveloped peak load coefficients for a partially enclosed building.

3.5 Results and Discussion

3.5.1 Tornado Load Coefficients

Figure 3.15 shows the distributions of the peak uplift, lateral, and moment coefficients for each building orientation and the three opening assumptions. The results are divided by either bay (uplift and lateral forces) or frame number (moments), as indicated in Figure 3.12.

The peak uplift force coefficients, $\hat{C}_Z$, are highly dependent on the opening configuration. The largest uplifts are observed for a perfectly sealed building, where both the aerodynamic forces and APD contribute to the overall uplift force. In the case of an enclosed building with distributed leakage, the uplift coefficients are reduced by approximately 65% relative to the sealed building, which is due to the effect of the internal pressure to equalize the APD over the building envelope (although the degree to which the full APD is equalized by the internal pressure was not investigated). Once a dominant opening corresponding to a partially enclosed building is also considered in addition to the distributed leakage, the resulting uplift coefficients fell in-between the sealed and distributed leakage opening cases, with approximately a 20% reduction versus the perfectly sealed building case. The distribution of peak uplift coefficients is relatively uniform across

all five bays of the building, however, there is a slight trend for the highest uplift forces to occur within the end Bay 1, which is subjected to the highest suction forces due to flow separations as depicted previously by the mean pressure distributions in Figure 3.5 and Figure 3.6.

In contrast to the uplift coefficients, the peak lateral force coefficients, $\hat{C}_Y$, are independent of the internal pressure since its effect is canceled out when the net force over the "windward" and "leeward" faces is calculated. The $\hat{C}_Y$ coefficients also trend upwards from Bay 1 to Bay 5 in an opposing manner to the pattern observed for $\hat{C}_Z$. From the mean pressure distributions displayed in Figure 3.5 and Figure 3.6, it was observed that the Bay 5 region is subjected to a combination of pressure from the impinging radial and tangential components of the vortex on the windward face in addition to high suctions on the leeward face that would have resulted in a large net lateral force as the tornado passed by the building. This phenomenon is particularly noticeable for the 0° and 45° building orientations, which are associated with larger peak $\hat{C}_Y$ coefficients at Bay 5.

The peak moment coefficients, $\hat{C}_M$, at the frame ridge and "Knee 1" behave in a similar fashion to the uplift coefficients with respect to the influence of internal pressures. The perfectly sealed building case produces the largest moments at all the investigated frame locations while the moment coefficients are the lowest for the enclosed building condition. The influence of internal pressures on the bending moments is revealed through the influence coefficient diagrams shown for the frame ridge and knee in Figure 3.13. From the distribution of influence coefficients, it is clear that the loads acting on the roof, whose magnitudes are highly susceptible to internal pressure conditions, are the largest contributors to the bending moments. As generally observed with the uplift and lateral force coefficients, the largest moment coefficients occur at the end frames as well. The moment coefficients for a building orientation of 90° are also noted to be slightly lower than the other two building orientations.

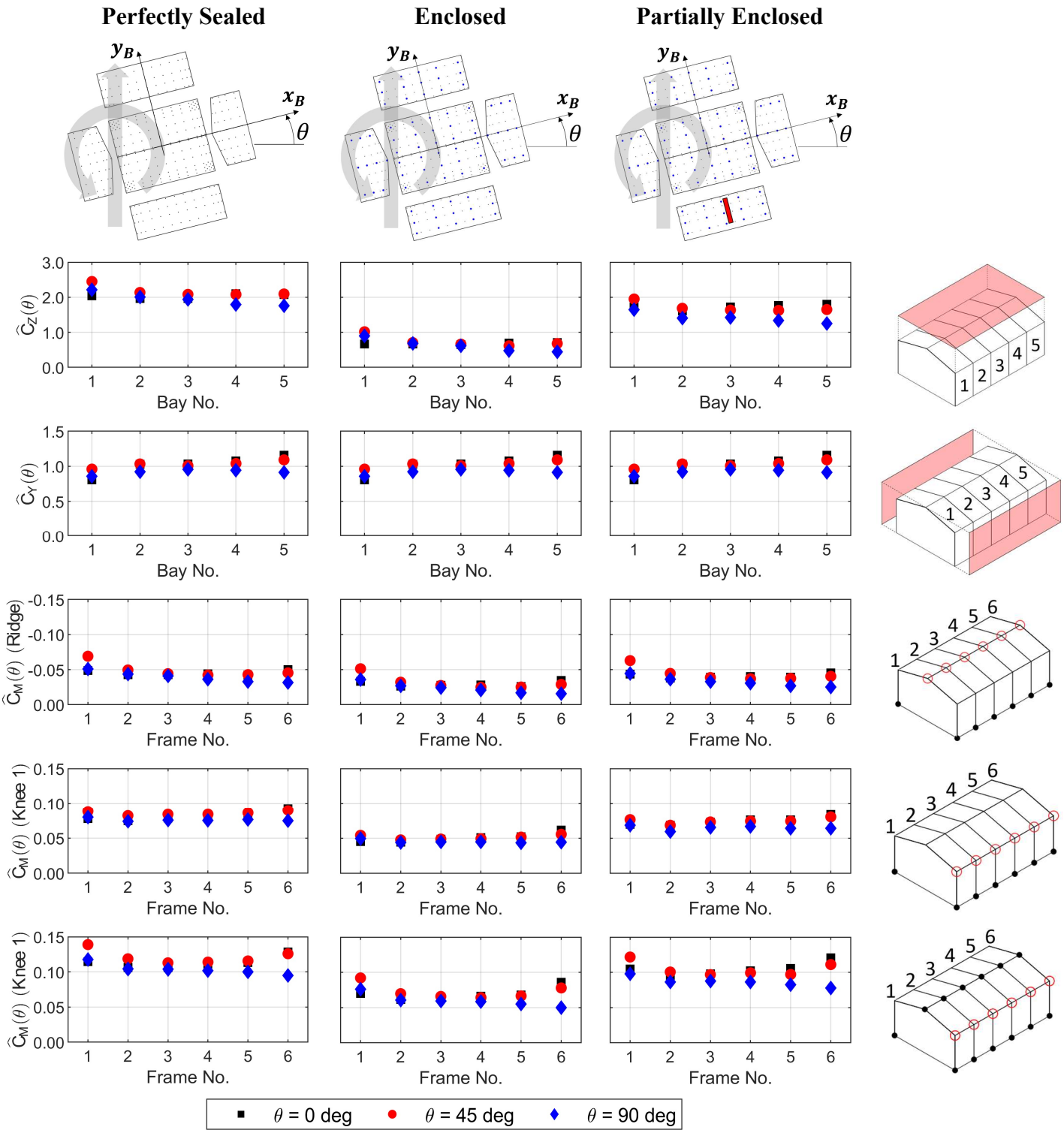

Figure 3.15: Load coefficients induced by tornado-like winds for building orientations, θ, of 0º, 45º, and 90º considering perfectly sealed, enclosed, and partially enclosed opening configurations.

As a supplement to Figure 3.15, the variations of peak load coefficients over all ten repeated runs are depicted in Figure 3.16 for the enclosed building. In the figure, the median peak value is plotted alongside bars that represent the 10^{th} and 90^{th} percentiles of the sample peaks from the ten repeated runs. Significant variations are observed in the peak values of the uplift and lateral force coefficients across all five bays of the building. This spread in the peak data could have been influenced by a variety of factors, including variations in the vortex path over each of the repeated runs, slight differences in vortex translation speeds, and the highly turbulent winds found near the core of the simulated tornado. The large suction pressures observed in Figure 3.5 and Figure 3.6 at the windward roof corner and edge regions can also be used to help explain the high variability of peak moment coefficients shown for end Frame 1 versus the smaller bending moment variations observed at the other frames.

As an additional measure of the variability of the peak load coefficients, Figure 3.17 depicts the normalized vortex position corresponding to the peak load coefficients for the enclosed building. As explained in Section 3.2.3 for the mean pressure coefficient distributions, the normalized vortex position was determined based on the position of the bellmouth which is much simpler to measure, with an offset applied to account for vortex tilting, which was estimated as 18^{o}. It is clearly shown that there is significant variability in the vortex position that causes the peak load over the ten repeated runs, which can possibly be attributed to the turbulence in the wind field found near the vortex core. There is, however, a consistent trend in vortex positions related to the building orientation. In general for the uplift, lateral force, and bending moments, the peak forces occur when the vortex is beside or just past the model at a building orientation of 0^{o}, while conversely the peak loads occur as the vortex is approaching the building model for an orientation of 90^{o}. Figure 3.5 Figure 3.6 can also be used in combination with Figure 3.17 to give a general sense of the pressure distributions that caused the peak load responses.

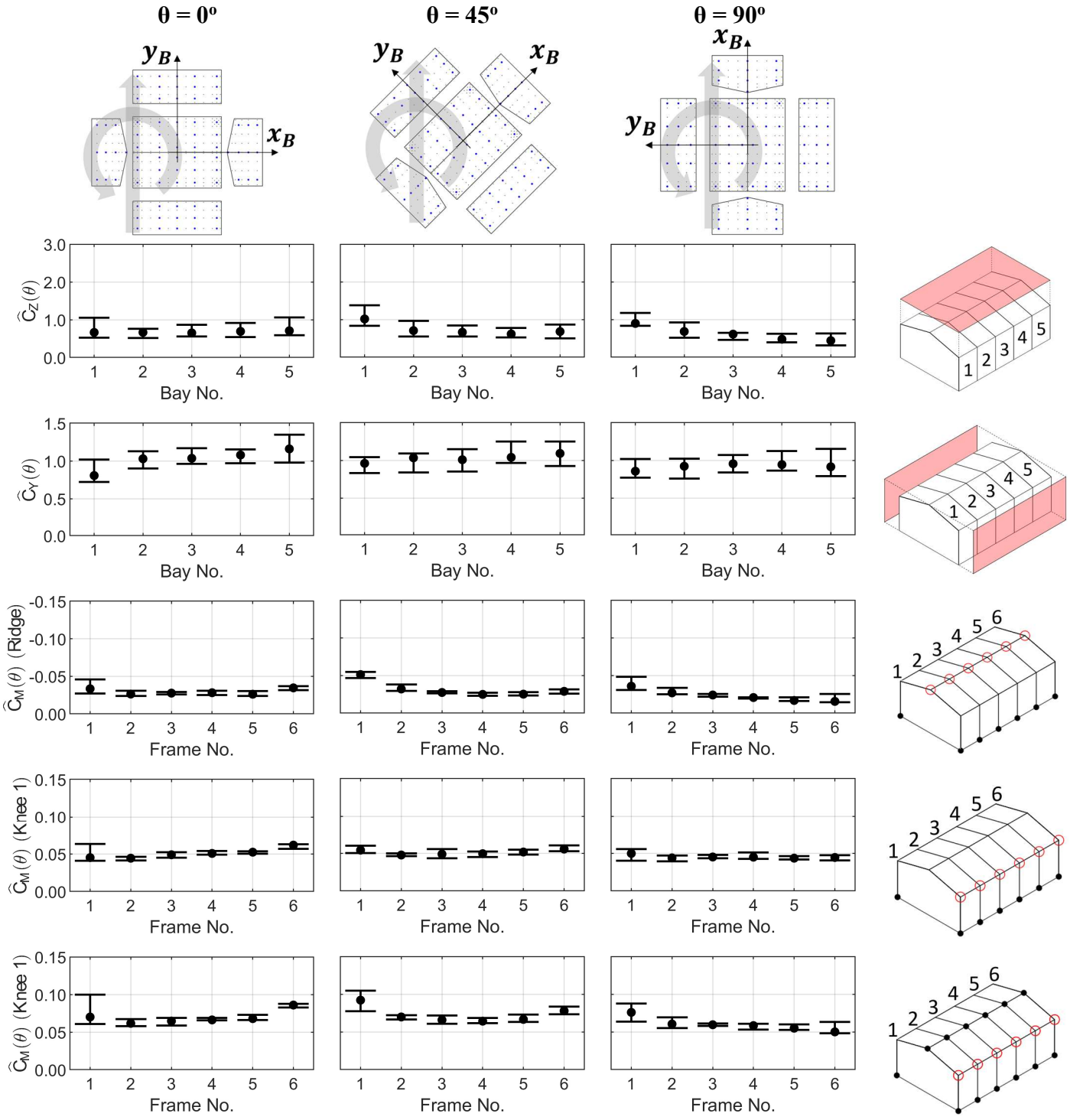

Figure 3.16: Load coefficients induced by tornado-like wind for an enclosed building at orientations, θ, of 0°, 45°, and 90°. The median peak values are plotted with bars corresponding to the 10th and 90th percentiles of the set of observed peaks for each building orientation.

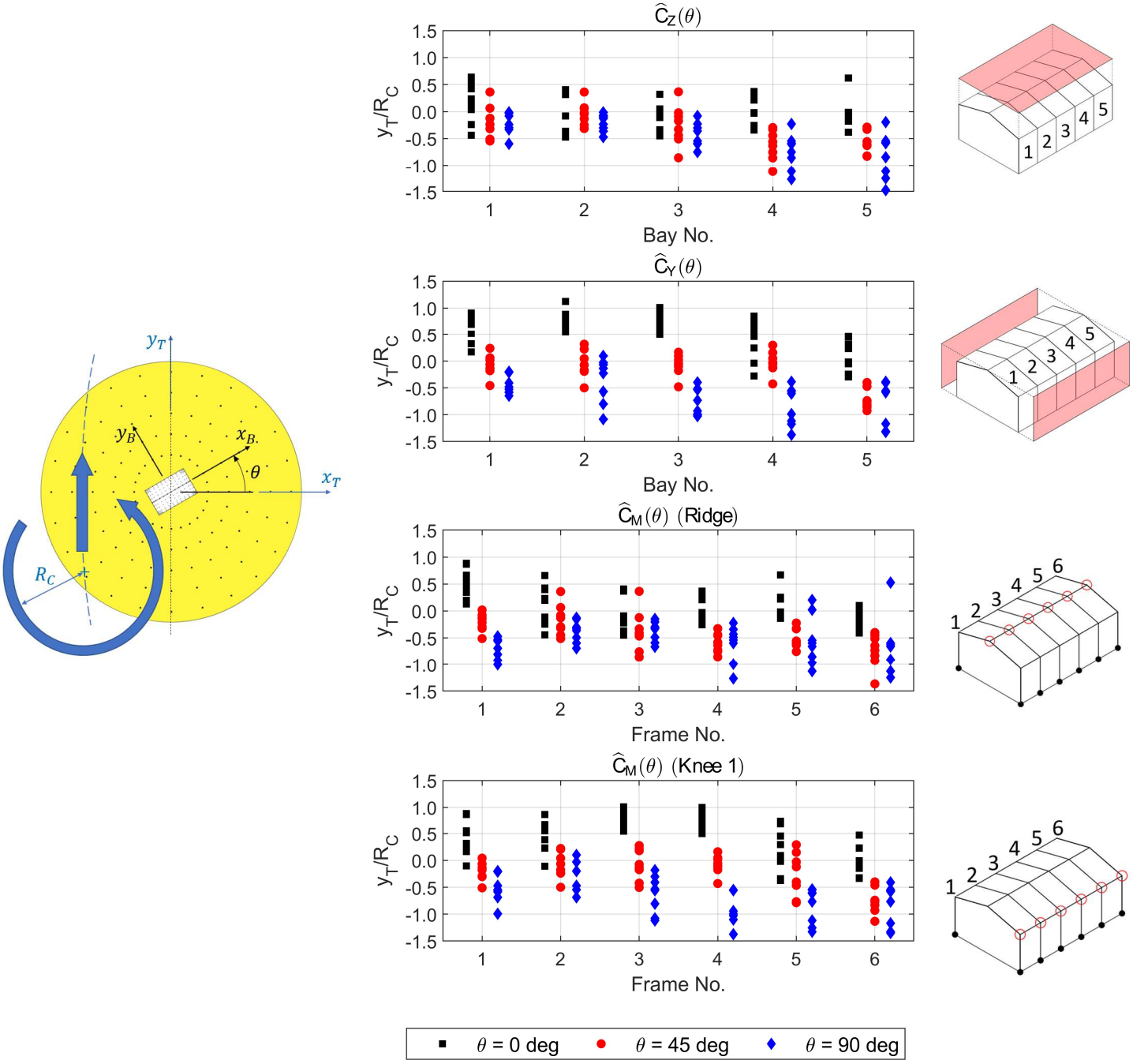

Figure 3.17: Normalized vortex position, y_T/R_C, corresponding to select peak observed load coefficients of each translation run for a building at orientations of 0°, 45°, and 90°.

3.5.2 WindEEE Tornado versus NIST ABL Wind Load Coefficients

The enveloped tornado-induced load coefficients have been compared to the enveloped load coefficients from ABL winds, as shown graphically in Figure 3.18 and numerically in Table 3.3, which are located near the end of Chapter 3. Relative differences were computed to compare the peak enveloped load coefficients from the tornado flow, $\hat{C}_{TLV}$, to the ABL peak load coefficients, $\hat{C}_{ABL}$, using Equation 3.10.

$$Relative\ Difference\ (ABL, \%) = \frac{\hat{C}_{ABL} - \hat{C}_{TLV}}{\hat{C}_{TLV}} * 100\ \% \tag{3.10}$$

The largest differences between the load coefficients from tornado and ABL winds occur for the perfectly sealed building. In this case, ABL-induced uplift coefficients are 64% lower on average across all five bays than the average tornado uplift coefficients. Further, moment coefficients from the ABL winds are 44% lower on average over all six of the two-pin frames at their ridges and 36% lower at the knees considering an average over all six frames of both the two-pin and three-pin frame systems. Once openings in the building envelope are considered via either an enclosed or partially enclosed internal pressure condition, the differences in load coefficients induced by the two different flow regimes are much smaller. For instance, the ABL-induced uplift forces are on average only 16% lower than those caused by tornado loads for both opening cases across all bays, while similarly the average relative differences in moment coefficients at the frame ridge and knees indicate the ABL-induced moments are 22% and 7% lower, respectively. The large differences in load coefficients between the two wind flow regimes for a perfectly sealed building demonstrate the additional contribution of the APD to the tornado-induced external loads that was not present for the ABL wind loads, while the influence of the APD is diminished once building openings are present, bringing the loads from the two datasets closely in line with each other. The enveloped ABL lateral force coefficients are found to be 19% lower than the tornado-induced lateral loads, with the largest differences highlighted at the interior bays.

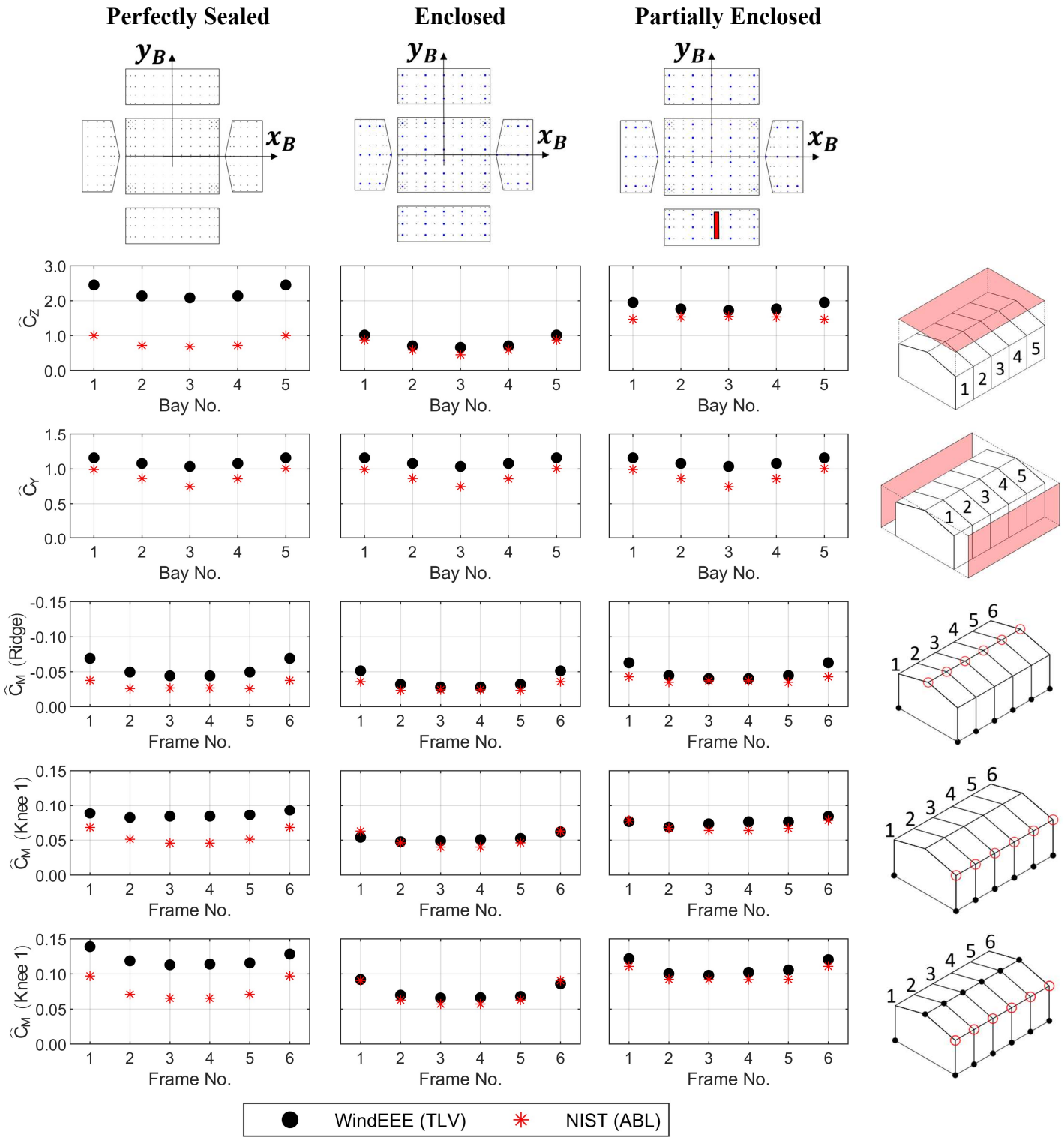

Figure 3.18: Comparison of enveloped peak load coefficients between the tornado WindEEE experimental data and ABL NIST aerodynamic data for the perfectly sealed, enclosed, and partially enclosed opening configurations.

In order to further understand the differences in peak load coefficients between the tornado and ABL wind fields, instantaneous net pressure coefficient distributions corresponding to the time step of the observed peak enveloped uplift and lateral forces are displayed in Figure 3.19 and Figure 3.20 for the enclosed opening configuration. In this case, the tornado instantaneous pressure distributions corresponded to one of the two observed peak loads that made up the median peak enveloped force coefficient, while the ABL pressure distributions reflected the time step and building orientation where the peak observed force coefficient occurred. The peak uplift pressure distributions in Figure 3.19 show variations between the tornado and ABL winds. This is especially evident within Bay 1 where the tornado pressure distribution has high suction loads in the lower roof corner while the ABL-induced pressures are nearly symmetrical under wind flow that is parallel to the roof ridge. This result demonstrates that even though the difference in peak uplift coefficients at Bay 1 between the tornado and ABL winds is only 14%, the pressure distributions that produce these peak forces have different characteristics from each other. Further, Figure 3.20 also reveals significant differences in the pressure distributions producing the peak horizontal forces. There are noticeably larger suction loads on the leeward walls in the case of the tornado pressures, which may help to explain the larger horizontal load coefficients observed for the tornado winds.

A similar approach is taken to understand the differences in load distributions on the primary frames that produce the peak bending moment coefficients. Figure 3.21 shows the instantaneous load distributions at the purlin attachment points producing the peak moment coefficients at the frame ridge. In this case, it appears that the uplift forces are more evenly distributed over the frame girders (i.e. roof) in the case of tornado-induced loads, while they are concentrated at the frame ridge and windward knee for the case of ABL winds. A similar trend can be seen in Figure 3.22 for the moment coefficient at the frame knee. There are also some variations in the load distributions on the frame columns between both wind fields, which are most noticeable for the peak moments at the knee. It is important to note that all of these figures show instantaneous load distributions that are highly variable due a variety of factors, including turbulence intensities or vortex position (in the case of tornado winds). Therefore, caution should be taken in using them to widely interpret the differences between tornado and ABL wind loads.

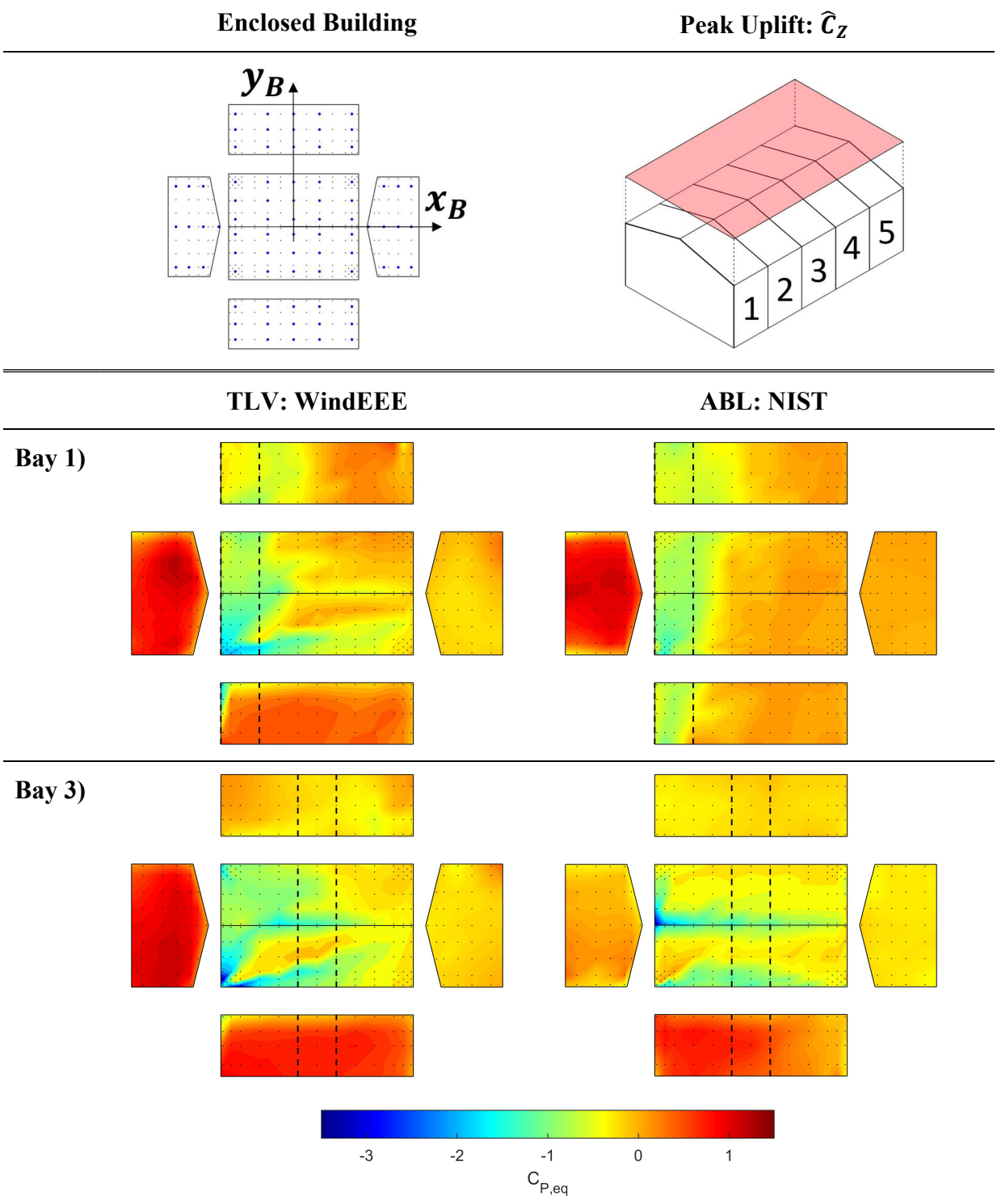

Figure 3.19: Instantaneous pressure distributions for an enclosed building corresponding to the peak enveloped uplift coefficients for both tornado and ABL winds.

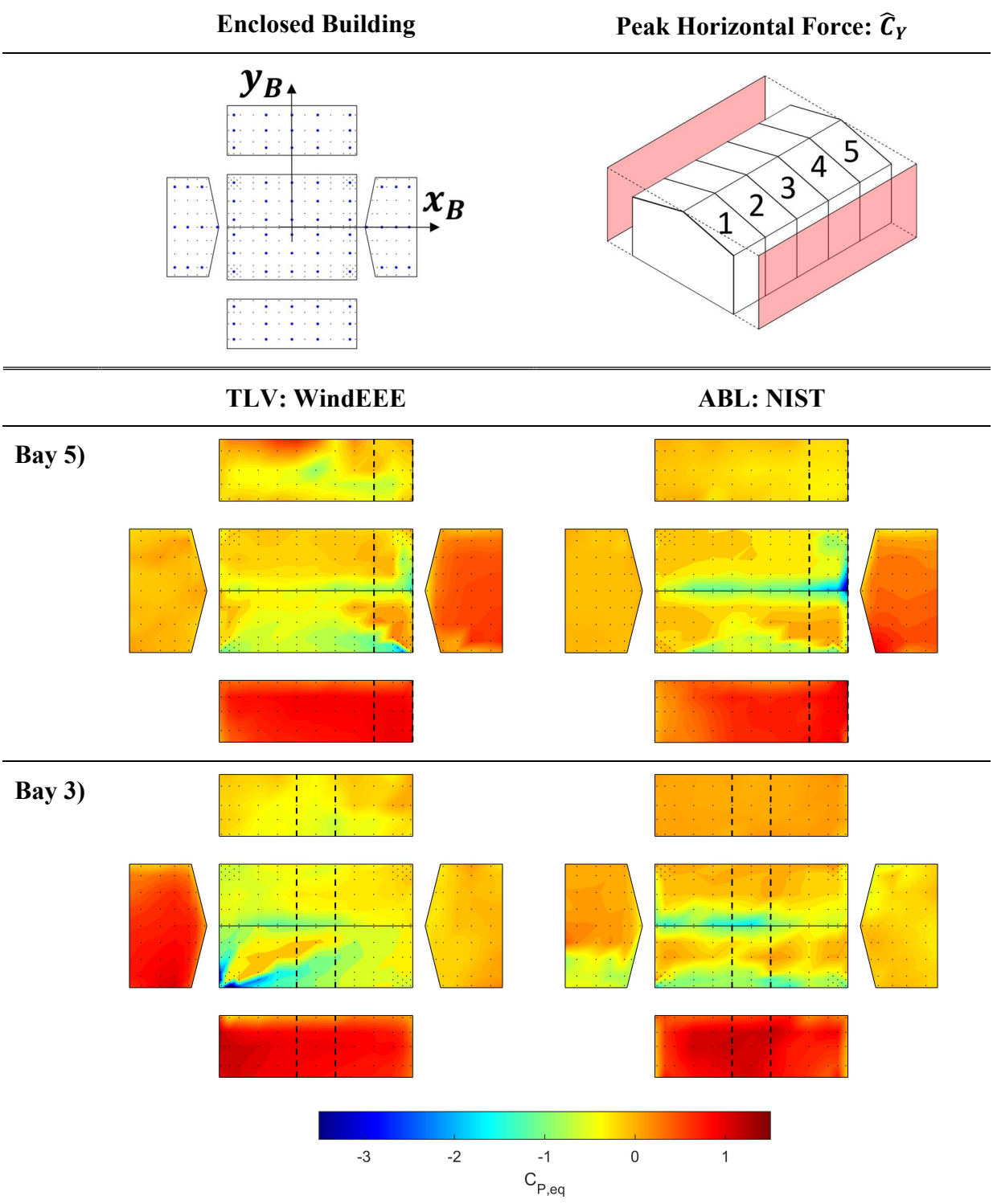

Figure 3.20: Instantaneous pressure distributions for an enclosed building corresponding to the peak enveloped horizontal force coefficients for both tornado and ABL winds.

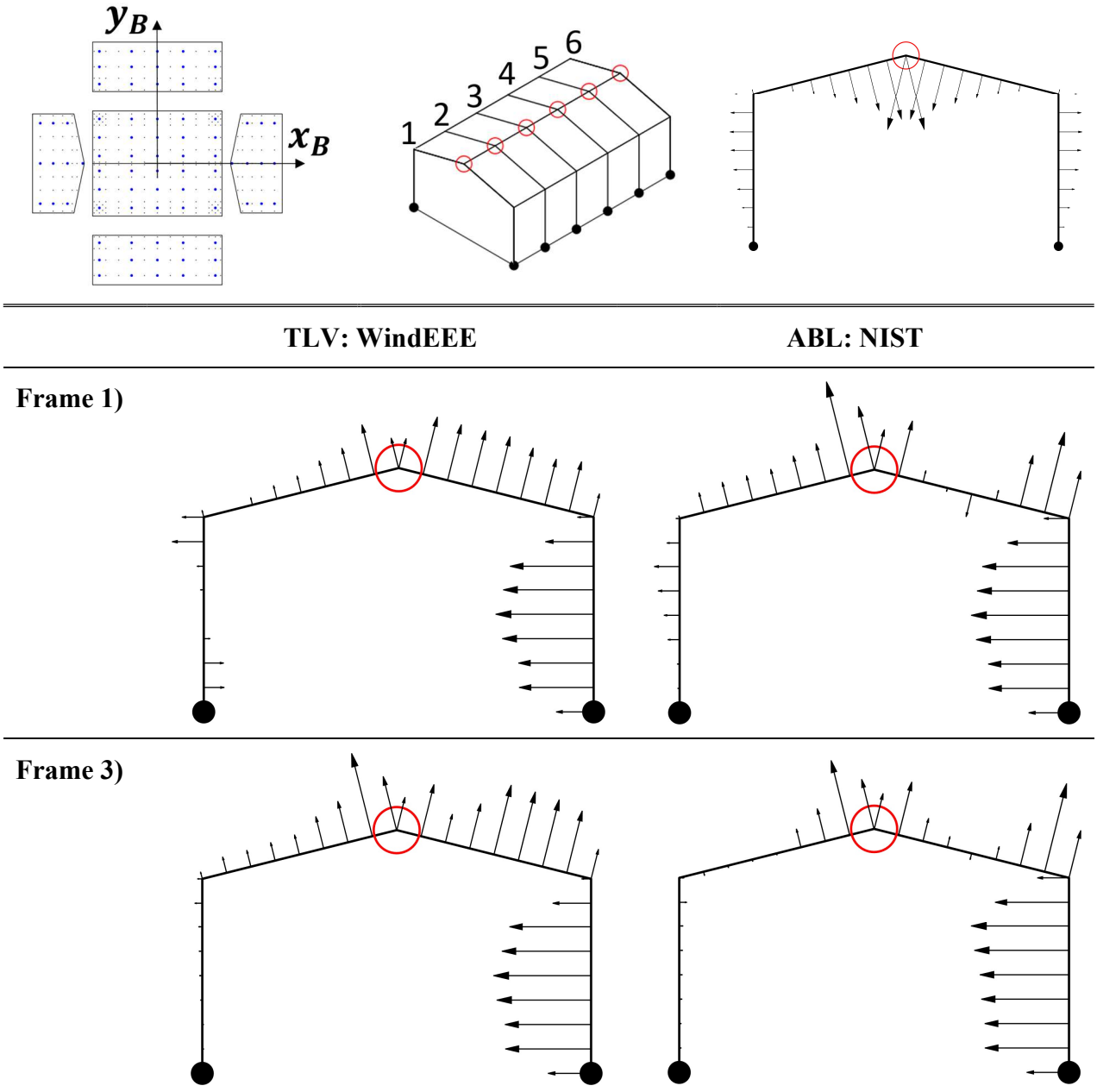

Figure 3.21: Instantaneous frame load distributions for an enclosed building corresponding to the peak enveloped moment coefficients at the ridge of a frame pined at the base for both tornado and ABL winds.

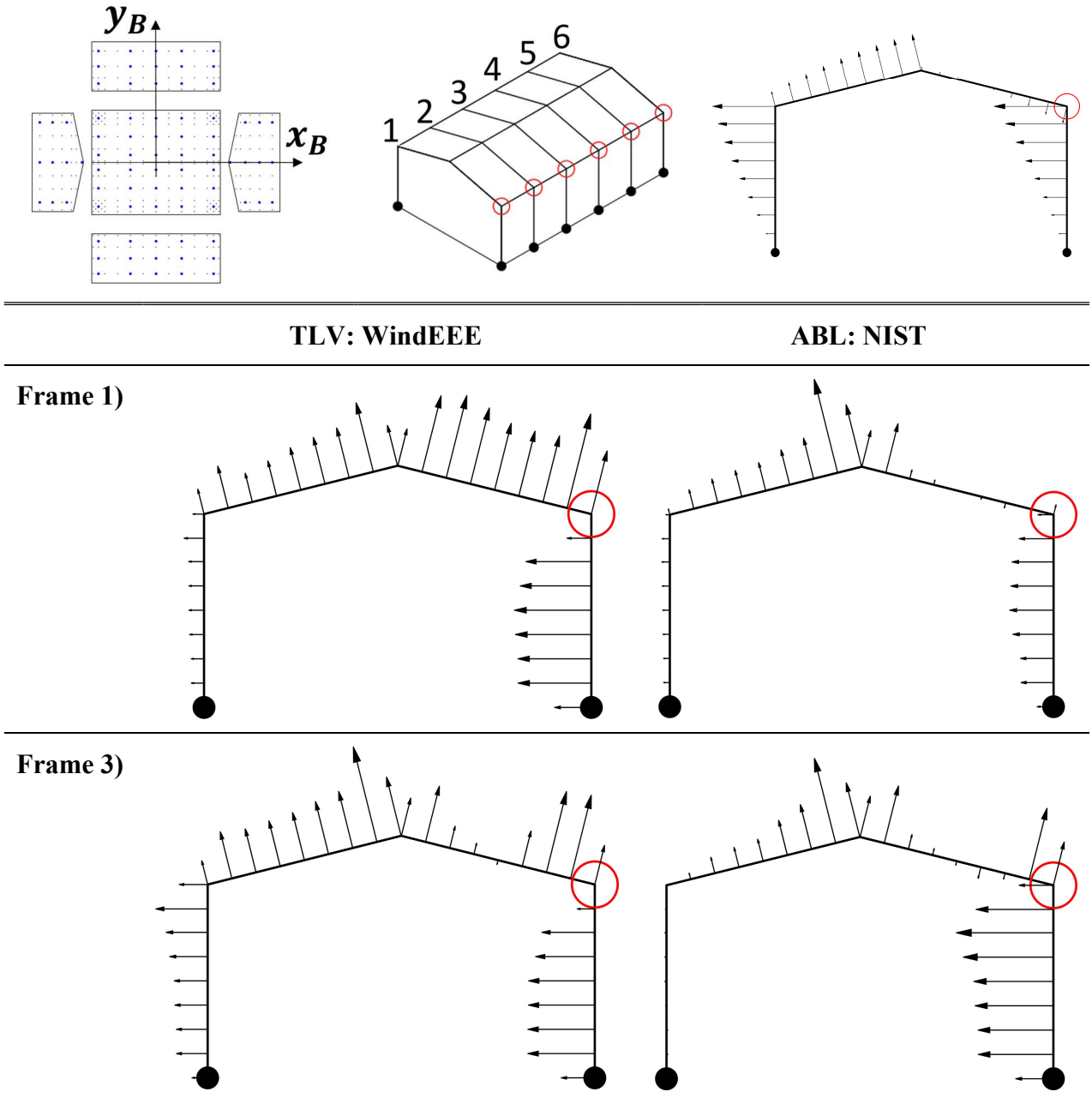

Figure 3.22: Instantaneous frame load distributions for an enclosed building corresponding to the peak enveloped moment coefficients at Knee 1 of a frame pined at the base for both tornado and ABL winds.

3.5.3 WindEEE Tornado versus ASCE 7-22 Tornado Load Coefficients

3.5.3.1 ASCE 7-22 Tornado Wind Loads

A new chapter is being proposed within the wind load section of the ASCE 7-22 "Minimum Design Loads and Associated Criteria for Buildings and Other Structures" to address tornado-induced loads on buildings. This new section of the standard will replace the current tornado load commentary found in Chapter C26 of ASCE 7-16 (ASCE, 2017). At the time of writing, a draft of the ASCE 7-22 standard has been released for public comment, therefore it is acknowledged that the new tornado load provisions are still preliminary.

The design tornado wind pressures, p, for the design of the MWFRS of a low-rise building are defined in ASCE 7-22 as follows:

$$p = \left(\frac{1}{2}\rho K_{zTor} K_e V_T^2\right)\left(K_{dT} K_{vT} G_T C_p - GC_{piT}\right) \tag{3.11}$$

where ρ is the air density, V_T^2 is the 3-second gust tornado wind speed obtained at a height of 10 m independent of terrain, K_{zTor} is the tornado velocity pressure exposure coefficient, K_e is the ground elevation factor, K_{dT} is the tornado directionality factor, and GC_{piT} is the tornado internal pressure coefficient. K_{vT} is a pressure coefficient adjustment factor to account for the significant vertical component of tornado winds that occur near the core of the vortex, which result in increased uplift forces on the roof. For the design of the MWFRS, C_p is the external pressure coefficient for the building surface zones specified by Figure 27.3-1 in ASCE 7-22 and G_T is the tornado gust-effect factor. Based on the tornado wind load provisions and considering the dimensions of the building used in this study, the design wind pressure factors were determined to be the following:

- K_{zTor} was 1.0 at mean roof height of 13.7 m for the proposed tornado wind profile in the standard.
- K_e equaled 1.0 as no adjustment was needed for air density.

- K_{dT} was taken as 1.0 for the MWFRS tornado pressures in contrast to a value of 0.8 recommended in ASCE 7-22. This was done as a conservative approach until further information on the tornado directionality factor is published.
- K_{vT} equaled 1.1 for negative roof pressures, and 1.0 for negative wall pressures and all positive pressures on the roof and walls.
- G_T was equal to 0.85, which is the same for typical low-rise buildings subjected to ABL winds.

The external pressure coefficients were the same as those derived for ABL winds, which vary depending on the building surface zone and predominant wind direction considered as shown in Figure 3.23. The internal pressure coefficients provided in ASCE 7-22 include the effects of both aerodynamically induced internal pressures and the atmospheric pressure drop. Therefore, $GC_{P_i} = +1.0$ for a perfectly sealed building, $GC_{P_i} = -0.18$ to $+0.55$ for an enclosed building, and $GC_{P_i} = \pm 0.55$ for a partially enclosed building.

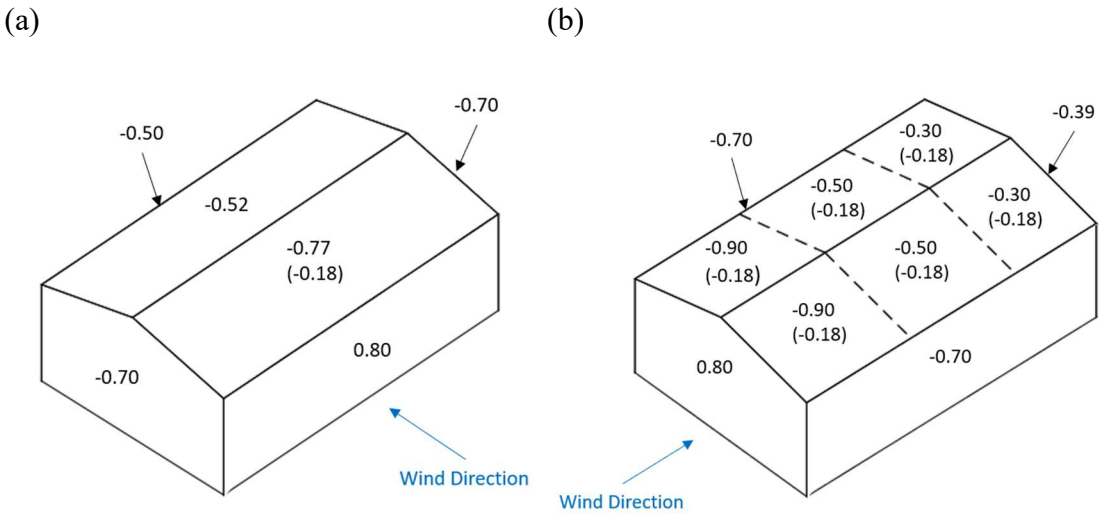

Figure 3.23: C_P values from ASCE 7-22 Figure 27.3-1 for the design of the MWFRS using the Directional procedure for (a) wind direction predominately normal to the roof ridge and (b) wind direction predominately parallel to the roof ridge.

3.5.3.2 Tornado Wind Load Coefficient Comparisons

To assess the current tornado wind load provisions in ASCE 7-22, the load coefficients derived from the standard were compared to the tornado load coefficients

obtained from the WindEEE Dome testing. To facilitate these comparisons, modifications to the ASCE 7-22 pressure coefficients were made in a similar fashion to the ABL wind data through the application of a wind tunnel factor, $F_{WT,ASCE}$, as shown in Equation 3.12.

$$C_{P,eq} = \frac{\left(\frac{1}{2}\rho K_{zTor} K_e V_T^2\right)\left(K_{dT} K_{vT} G_T C_p - G C_{piT}\right)}{\frac{1}{2}\rho V_{ref,TLV}^2} \tag{3.12a}$$

$$C_{P,eq} = F_{WT,ASCE}\left(K_{dT} K_{vT} G_T C_p - G C_{piT}\right) \tag{3.12b}$$

In this formulation, $C_{P,eq}$ is the net pressure equivalent design coefficient, $V_{ref,TLV}^2$ is the 3-second gust reference wind velocity measured at the mean roof height from the tornado wind test, and all other terms are defined as previous. By substituting the design tornado pressure factors outlined in previous section, $F_{WT,ASCE}$ was calculated to be 1.0.

Comparisons between the enveloped tornado-induced peak load coefficients to those from ASCE 7-22 are shown graphically in Figure 3.24 and numerically alongside the comparisons to the NIST ABL data in Table 3.3. Relative differences between the peak enveloped load coefficients from WindEEE ($\hat{C}_{TLV}$) and ASCE 7-22 ($\hat{C}_{ASCE}$) were computed using Equation 3.13.

$$Relative\ Difference\ (ASCE, \%) = \frac{\hat{C}_{ASCE} - \hat{C}_{TLV}}{\hat{C}_{TLV}} * 100\ \% \tag{3.13}$$

The differences in the peak uplift and moment coefficients between the tornado WindEEE test and those computed from ASCE 7-22 again depends on the opening condition. For the perfectly sealed building, the peak ASCE-derived uplift coefficients are 20% lower than the average tornado uplift. Considering that the relative difference in uplift loads was 64% when comparing the experimental tornado uplift loads to the ABL wind-induced uplift, this result demonstrates the impacts of the K_{vT} factor and internal pressure of $+1.0$ specified in the standard to represent the effects of the enhanced vertical winds and APD present in the tornado vortex flow. Further, the average relative differences in moment coefficients at the frame ridge and knees reveals that the ASCE coefficients are

36% and 13% lower, respectively, than the tornado-induced moments, which is also a smaller difference versus the comparisons made to the ABL wind-induced moments.

In the case of the enclosed building with distributed leakage, the ASCE 7-22 tornado loads appear to quite effectively envelope the uplift and moment coefficients observed from the tornado test data. For this opening configuration, the ASCE-derived loads exceed the tornado loads by 65% for the uplift and 20% for the moments at the frame knees, while they are 20% lower at the frame ridge. The generally observed conservativeness of the ASCE tornado loads can be attributed to the internal pressure coefficient of $+0.55$ used in this case, which is an increase from the typical value of $+0.18$ used by the standard for enclosed buildings. This increase in internal pressure was done to account for the increased effects of the APD on the apparent internal pressure, although its effect appeared to be negligible from the comparisons made with the NIST ABL data. That said, this may not be the case for larger building footprint ratios greater than the 2.0% used in this study (ASCE, 2021; Kassab, 2021).

For the final opening configuration, which involves a partially enclosed building with a dominant opening, the ASCE 7-22 loads are slightly lower than the WindEEE tornado-induced loads, with average relative differences of 28%, 42%, and 17% for the uplift, ridge moment, and knee moment coefficients, respectively. These differences are very comparable to those seen for the perfectly sealed building. In this case, no adjustment is made to the internal pressure coefficient in ASCE 7-22, which remained at $+0.55$. This contrasts with observations from the tornado loads which showed an increase in uplift and moment coefficients due to further pressurization of the internal volume of the building as winds impinged on the dominant wall opening, a behaviour that was also reflected in the NIST ABL data. Again, since the WindEEE testing considered only one building size, opening location, and tornado structure, the tested case may have been more critical than other possible scenarios of tornado-induced loading. However, these results suggest that further modifications to the positive bounds of the ASCE design internal pressure coefficients may be necessary to better reflect the net pressures observed for the tornado winds.

For the lateral force coefficients, which did not depend on opening conditions, the ASCE loads are 14% lower than those from tornadoes, which are slightly closer than the differences noted between the tornado and ABL-induced lateral loads. This is an expected result since the tornado design lateral forces are very similar to those used for ABL winds. This suggests that an increase in the external suction pressure coefficients on the leeward walls in ASCE 7-22 may be necessary to rectify the observed differences, which is informed by the enhanced tornado-induced wall suctions shown in Figure 3.20.

As an overall observation, it appears that the proposed ASCE 7-22 tornado load provisions are effective for the design of this particular case study building with an enclosed opening condition, as the ASCE-derived loads generally tend to envelope the uplift and moment coefficients. As noted in the commentary of the proposed tornado load chapter, it is very unlikely that a building can be designed to be perfectly sealed, while a critical case was assumed for the partially enclosed structure, in which a single internal volume and a large windward wall opening were used. Further, this study considers a "worst-case" scenario where the building was located close to the core region of the vortex, subjecting it to the highest tornado wind speeds, enhanced wind curvatures from the vortex, large turbulence intensities, and large vertical wind speed components that a building located further from the core of the tornado would likely not experience. Finally, the large exceedances in moment coefficients over ASCE 7-22 at the end frames could have been partially caused by the assumption that neglected any additional support provided by the end walls or additional framing, which is not realistic in engineering practice.

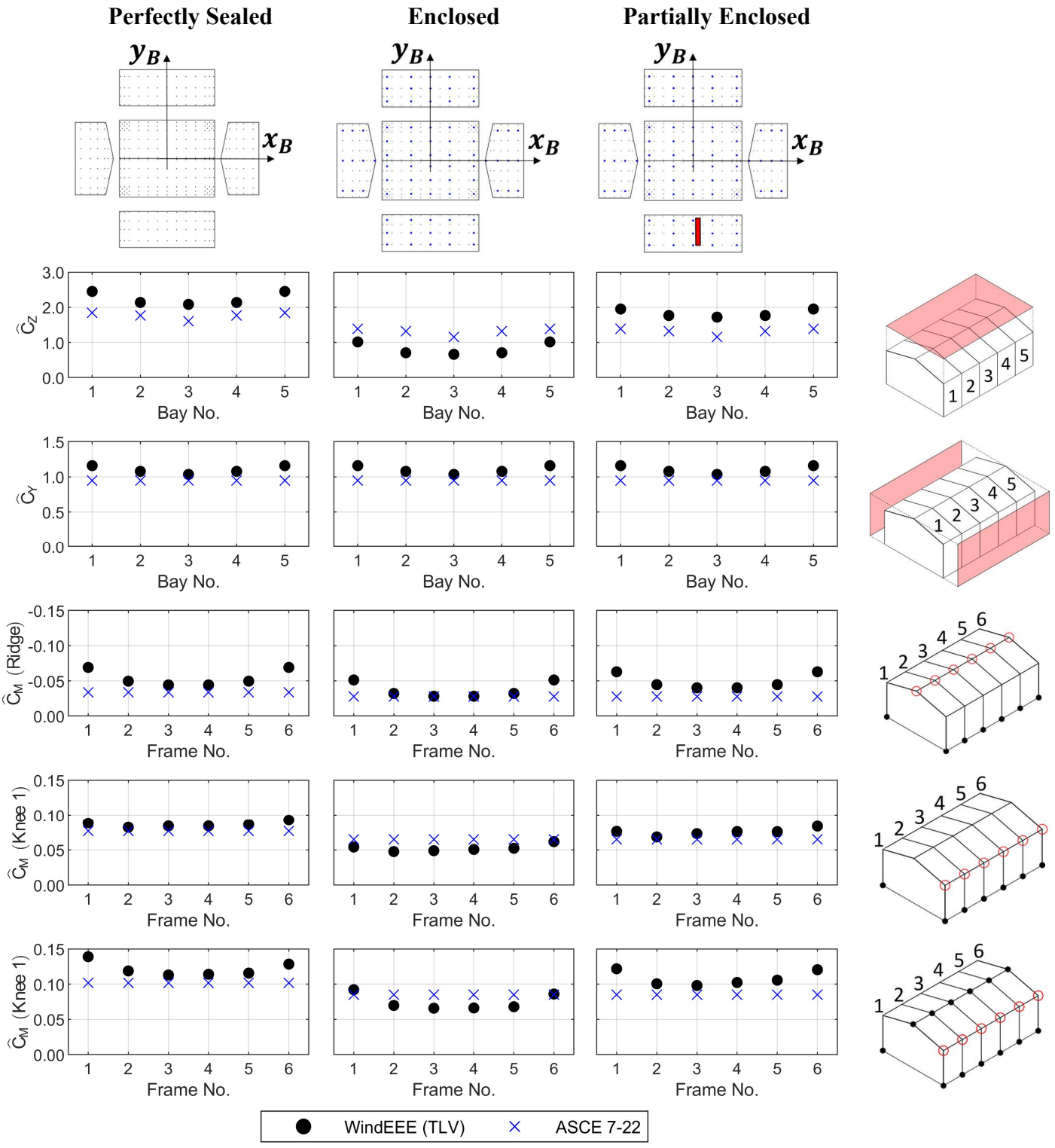

Figure 3.24: Comparison of enveloped peak load coefficients between the tornado WindEEE experimental data and ASCE 7-22 design pressures for the perfectly sealed, enclosed, and partially enclosed opening configurations.

Table 3.3: Load coefficient comparison between the tornado WindEEE experimental data, ABL NIST aerodynamic data and ASCE 7-22 design pressures for a perfectly sealed, enclosed and partially enclosed building.

Response	*Frame/ Bay No.*	*WindEEE TLV*	*NIST ABL*	*Relative Difference (%)*	*ASCE 7-22*	*Relative Difference (%)*
Opening Condition: Perfectly Sealed						
Uplift ($\hat{C}_Z$)	1	2.451	1.005	-59	1.842	-25
	2	2.137	0.714	-67	1.767	-17
	3	2.082	0.687	-67	1.602	-23
Lateral force ($\hat{C}_Y$)	1	1.159	0.993	-14	0.947	-18
	2	1.079	0.862	-20	0.947	-12
	3	1.035	0.746	-28	0.947	-8
Moment at ridge: 2-pin frame ($\hat{C}_M$)	1	-0.069	-0.038	-45	-0.034	-51
	2	-0.050	-0.026	-48	-0.034	-32
	3	-0.044	-0.027	-39	-0.034	-24
Moment at knee 1: 2-pin frame ($\hat{C}_M$)	1	0.089	0.068	-23	0.077	-13
	2	0.082	0.051	-38	0.077	-6
	3	0.084	0.046	-45	0.077	-8
Moment at knee 2: 2-pin frame ($\hat{C}_M$)	1	0.093	0.068	-27	0.077	-17
	2	0.086	0.051	-41	0.077	-11
	3	0.084	0.046	-46	0.077	-9
Moment at knee 1: 3-pin frame ($\hat{C}_M$)	1	0.139	0.097	-30	0.102	-27
	2	0.119	0.071	-40	0.102	-14
	3	0.113	0.065	-42	0.102	-10
Moment at knee 2: 3-pin frame ($\hat{C}_M$)	1	0.128	0.097	-24	0.102	-21
	2	0.116	0.071	-39	0.102	-12
	3	0.114	0.065	-43	0.102	-11
Opening Condition: Enclosed						
Uplift ($\hat{C}_Z$)	1	1.016	0.872	-14	1.392	37
	2	0.706	0.586	-17	1.317	87
	3	0.662	0.452	-32	1.153	74
Lateral force ($\hat{C}_Y$)	1	1.159	0.993	-14	0.947	-18
	2	1.079	0.862	-20	0.947	-12
	3	1.035	0.746	-28	0.947	-8
Moment at ridge: 2-pin frame ($\hat{C}_M$)	1	-0.051	-0.036	-30	-0.028	-46
	2	-0.032	-0.023	-28	-0.028	-14
	3	-0.028	-0.024	-13	-0.028	-2
Moment at knee 1: 2-pin frame ($\hat{C}_M$)	1	0.054	0.063	16	0.065	20
	2	0.048	0.046	-4	0.065	37
	3	0.049	0.040	-18	0.065	33

Response	***Frame/ Bay No.***	***WindEEE TLV***	***NIST ABL***	***Relative Difference (%)***	***ASCE 7-22***	***Relative Difference (%)***
Moment at knee 2: 2-pin frame ($\hat{C}_M$)	1	0.062	0.063	2	0.065	6
	2	0.052	0.046	-12	0.065	24
	3	0.051	0.040	-21	0.065	29
Moment at knee 1: 3-pin frame ($\hat{C}_M$)	1	0.092	0.091	-1	0.085	-8
	2	0.070	0.063	-10	0.085	22
	3	0.066	0.057	-13	0.085	29
Moment at knee 2: 3-pin frame ($\hat{C}_M$)	1	0.086	0.091	6	0.085	-1
	2	0.068	0.063	-7	0.085	25
	3	0.066	0.057	-14	0.085	29
Opening Condition: Partially Enclosed						
Uplift ($\hat{C}_Z$)	1	1.950	1.464	-25	1.392	-29
	2	1.766	1.533	-13	1.317	-25
	3	1.720	1.555	-10	1.153	-33
Lateral force ($\hat{C}_Y$)	1	1.159	0.993	-14	0.947	-18
	2	1.079	0.863	-20	0.947	-12
	3	1.035	0.746	-28	0.947	-8
Moment at ridge: 2-pin frame ($\hat{C}_M$)	1	-0.063	-0.043	-32	-0.028	-56
	2	-0.045	-0.035	-21	-0.028	-38
	3	-0.040	-0.037	-8	-0.028	-31
Moment at knee 1: 2-pin frame ($\hat{C}_M$)	1	0.076	0.078	2	0.065	-15
	2	0.068	0.067	-3	0.065	-5
	3	0.073	0.064	-13	0.065	-11
Moment at knee 2: 2-pin frame ($\hat{C}_M$)	1	0.084	0.078	-7	0.065	-22
	2	0.076	0.067	-12	0.065	-14
	3	0.076	0.064	-16	0.065	-14
Moment at knee 1: 3-pin frame ($\hat{C}_M$)	1	0.122	0.111	-9	0.085	-30
	2	0.101	0.092	-8	0.085	-15
	3	0.098	0.092	-6	0.085	-13
Moment at knee 2: 3-pin frame ($\hat{C}_M$)	1	0.120	0.111	-8	0.085	-29
	2	0.106	0.092	-12	0.085	-19
	3	0.102	0.092	-10	0.085	-17

3.5.3.3 Case Study

The new tornado chapter in ASCE 7-22 will contain tornado hazard maps that can be used to determine tornado design wind speeds based on the building's location, size, and exceedance probability (as determined by the structure's risk category). As an added level of interpretation of the load coefficient data comparisons between the WindEEE experiments and tornado design loads from ASCE 7-22, dimensionalized peak forces and moments were calculated assuming the studied building model was located near Chicago, Illinois. The loads coefficients calculated using ASCE 7-22 shown in Figure 3.25 were multiplied by the velocity pressure, $\frac{1}{2}\rho K_{zTor} K_e V_T^2$, using tornado wind speeds of 35.8 m/s, 49.2 m/s, and 68.4 m/s, which correspond to mean recurrence intervals (MRIs) of 3,000, 10,000, and 100,000 years. For comparison, the WindEEE tornado loads were multiplied by the reference dynamic pressure, $\frac{1}{2}\rho V_{ref}^2$, corresponding to the assumed full-scale horizontal wind speed of 49.2 m/s, which is the upper-limit wind speed of an EF1 tornado. Further, the uplift and lateral force coefficients are reported herein as a load per unit area (i.e. kPa) while the moment coefficients are multiplied by their normalizing dimensions, $W^2 B$, so that the results are reported in units of kN*m.

From the comparisons depicted in Figure 3.25, it is first clear that the loads are heavily tied to the MRI-specific wind speeds that depend on the risk designation of the structure. Considering an MRI of 10,000 years, which uses the same tornado wind speed as the EF1 design tornado used for this analysis, there are no differences in the trends observed from the load coefficient analysis. It is important however to note that the bending moments at the end frames, which are associated with the largest moment coefficients, are much lower in magnitude than those from the interior frames due to their tributary areas of the end frames being half as wide. The design loads are much lower than those from the case study EF1 tornado when an MRI of 3,000 years is considered. This result is sensible since the design wind speed is significantly reduced to account for the unlikelihood that the building will be close to the core of the vortex during a tornado event. At the other extreme, the 100,000-year MRI design wind speed completely envelops the WindEEE-derived wind loads from an EF1 tornado, aside from the calculated moments at the ridge of the end frames.

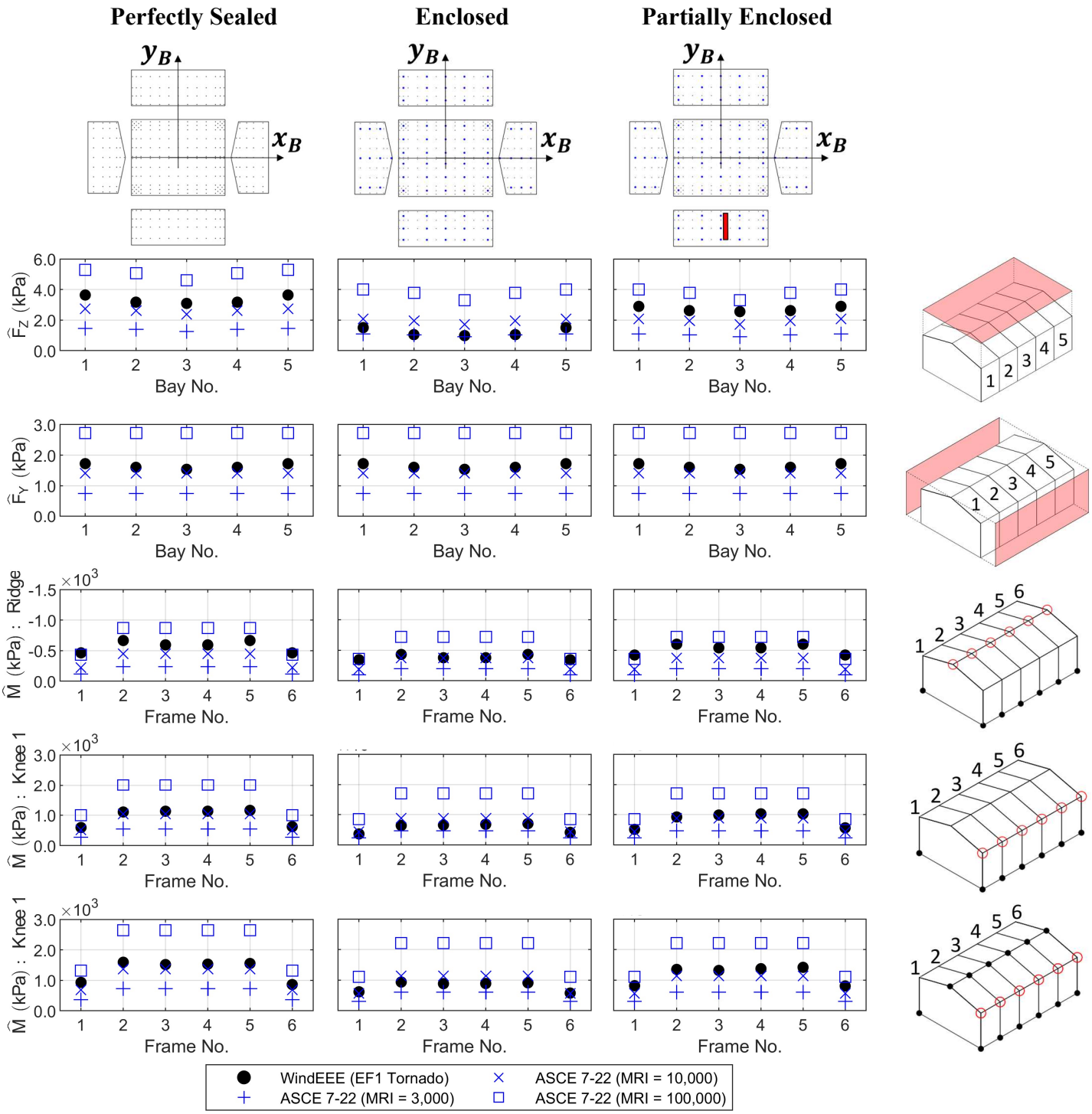

Figure 3.25: Case study comparison of enveloped peak loads based on a EF1 tornado reference wind speed (49.2 m/s) between the tornado experimental data and ASCE 7-22 design pressures for a perfectly sealed, enclosed, and partially enclosed building corresponding to three mean recurrence intervals (MRIs).

3.6 Conclusions

This chapter aimed at investigating the differences between tornado-induced and atmospheric boundary layer (ABL) wind pressures on the main wind force resisting system (MWFRS) loads of a low-rise, rectangular, gable roof building consisting of equally spaced frames. This investigation was then elaborated by comparing the design tornado loads provided in the proposed ASCE 7-22 standard, which have their basis in ABL wind aerodynamics, to the design loads obtained from experimental tornado tests. High Frequency Pressure Integration (HFPI) tests were conducted at the Wind Engineering, Energy, and Environment (WindEEE) Dome to assess the complex fluid-structure interactions between the building and a translating tornado-like vortex. These experiments captured the changes in pressure distributions for three different building orientations with respect to the translating tornado. Internal pressures were estimated using the established Helmholtz resonator model for two simple opening configurations: distributed leakage to represent an enclosed building and a dominant opening on the predominantly windward wall to simulate a partially enclosed building. Comparisons were made to ABL wind pressures obtained from the National Institute of Standards and Technology (NIST) database for a building with the same full-scale dimensions (Ho et al., 2005), and to the tornado pressures computed from the new tornado load chapter that is expected to be a part of the new ASCE 7-22 standard (ASCE, 2021).

The important observations made from the analysis of the MWFRS include the following:

i) Peak enveloped uplift and moment coefficients from the tornado-induced loading were largest for the case of a perfectly sealed building. Comparisons revealed that the measured ABL wind-induced uplift forces were on average 64% lower than the tornado uplift, while moments at the frame knees were 36% lower. These differences highlighted the impact of the atmospheric pressure drop (APD) on the resulting tornado loads.

ii) The assumed opening conditions representing an enclosed or partially enclosed building led to reductions in the net tornado uplift and moment coefficients, closely

aligning them with the ABL wind-induced net loads for the same enclosure classifications.

iii) The proposed tornado loads from ASCE 7-22 effectively enveloped the peak tornado uplift and moment coefficients for the enclosed building configuration but were unconservative for the perfectly sealed and partially enclosed buildings.

iv) Horizontal forces from the WindEEE-produced tornado exceeded those from both the NIST straight-line aerodynamic data and the ASCE 7-22 tornado load provisions by average relative differences of 19% and 14%, respectively.

v) Modifications to the design internal pressure coefficients and leeward wall suction external pressure coefficients may help to resolve the differences between the ASCE 7-22 and tornado structural wind load coefficients.

Overall, it appears that once net pressures are considered to account for leakage or dominant openings in the building envelope, the structural loads are reasonably close between the tornado experimental pressures and the NIST aerodynamic database. Further, the ASCE 7-22 load provisions performed well considering the simulated tornado and building size corresponded to one of the worst-case loading conditions (Razavi and Sarkar, 2018). However, there are important limitations of the results that need to be considered as they are interpreted. First, the tornado pressure coefficients were tied to the reference velocity selected for normalization, for which there are currently no broadly accepted standard definitions. Second, the study only investigated one building geometry and a limited range of building orientations, due to time and economic constraints. Finally, assumptions regarding the tornado scaling were susceptible to limitations of both the collected full-scale tornado data and the physical limits of the WindEEE Dome facility. Continued work by the research community on the experimental simulation of tornado-like vortices in conjunction with field observations (e.g. Lombardo, 2018) and computational fluid dynamic simulations (e.g. Nasir and Bitsuamlak, 2016; Gairola and Bitsuamlak, 2019) will help to further refine tornado wind load models for the design of low-rise buildings.

References

Amidror, I., 2002. Scattered data interpolation methods for electronic imaging systems: a survey. J. Electron. Imaging 11, 157–176. https://doi.org/10.1117/1.1455013

ASCE, 2017. Minimum design loads and associated criteria for buildings and other structures. American Society of Civil Engineers, Reston, Virginia.

ASCE, 2021. Draft of minimum design loads and associated criteria for buildings and other structures (released for public comment). American Society of Civil Engineers, Reston, Virginia.

Baker, C., Sterling, M., 2019. Are tornado vortex generators fit for purpose? J. Wind Eng. Ind. Aerodyn. 190, 287–292. https://doi.org/10.1016/j.jweia.2019.05.011

Durst, C.S., 1960. The statistical variation of wind with distance. Q. J. R. Meteorol. Soc. 86, 543–549.

Feng, C., Chen, X., 2018. Characterization of translating tornado-induced pressures and responses of a low-rise building frame based on measurement data. Eng. Struct. 174, 495–508. https://doi.org/10.1016/j.engstruct.2018.07.082

Gairola, A., Bitsuamlak, G.T., 2019. Numerical tornado modeling for common interpretation of experimental simulators. J. Wind Eng. Ind. Aerodyn. 186, 32–48. https://doi.org/10.1016/j.jweia.2018.12.013

Haan, F.L., Sarkar, P.P., Gallus, W.A., 2008. Design, construction and performance of a large tornado simulator for wind engineering applications. Eng. Struct. 30, 1146–1159. https://doi.org/10.1016/j.engstruct.2007.07.010

Haan, F.L., Balaramudu, V., Sarkar, P.P., 2010. Tornado-induced wind loads on a low-rise building. J. Struct. Eng. 136, 106–116. https://doi.org/10.1061/(ASCE)ST.1943-541X.0000093

Haan, F.L., 2017. An examination of static pressure and duration effects on tornado-induced peak pressures on a low-rise building. Front. Built Environ. 3, 1–11. https://doi.org/10.3389/fbuil.2017.00020

Hangan, H., 2014. The Wind Engineering Energy and Environment (WindEEE) Dome at Western University, Canada. Japan Assoc. Wind Eng. 39, 350–351. https://doi.org/10.5359/jawe.39.350

Ho, E., Surry, D., Morrish, D., Nywening, M., Kopp, G.A., Simiu, E., Main, J.A., Harris, G., 2003. University of Western Ontario data sets [WWW Document]. Natl. Inst. Stand. Technol. Eng. Lab. URL https://www.nist.gov/el/materials-and-structural-systems-division-73100/nist-aerodynamic-database/university-western (accessed 1.15.21).

Ho, E., Surry, D., Morrish, D., Kopp, G.A., 2005. The UWO contribution to the NIST aerodynamic database for wind loads on low buildings: Part 1. Archiving format and basic aerodynamic data. J. Wind Eng. Ind. Aerodyn. 93, 1–30. https://doi.org/10.1016/j.jweia.2004.07.006

Holmes, J.D., 1980. Mean and fluctuating internal pressures induced by wind, in: Fifth International Conference on Wind Engineering. Elsevier, Fort Collins, Colorado, pp. 435–450. https://doi.org/10.1016/B978-1-4832-8367-8.50046-2

Hu, H., Yang, Z., Sarkar, P.P., Haan, F.L., 2011. Characterization of the wind loads and flow fields around a gable-roof building model in tornado-like winds 835–851. https://doi.org/10.1007/s00348-011-1102-6

Jaffe, A.L., Kopp, G.A., 2021. Internal pressure modelling for low-rise buildings in tornadoes. J. Wind Eng. Ind. Aerodyn. 209, 104454. https://doi.org/10.1016/j.jweia.2020.104454

Kassab, A., 2021. Experimental study of tornado-induced pressures. (Ph.D. Dissertation) Western University Electronic Thesis and Dissertation Repository.

Kopp, G.A., Wu, C.H., 2020. A framework to compare wind loads on low-rise buildings in tornadoes and atmospheric boundary layers. J. Wind Eng. Ind. Aerodyn. 204, 104269. https://doi.org/10.1016/j.jweia.2020.104269

Lee, J.J., Samaras, T.M., Young, C.R., 2004. Pressure measurements at the ground in an F-4 tornado. 22nd Conf. Sev. Local Storms.

Letchford, C.W., Levitz, B., James, D.L., 2015. Internal pressure dynamics in simulated tornadoes, in: Structures Congress 2015. American Society of Civil Engineers, Reston, Virginia, pp. 2689–2701.

Lombardo, F.T., 2018. Engineering analysis of a full-scale high-resolution tornado wind speed record. J. Struct. Eng. (United States) 144, 1–9. https://doi.org/10.1061/(ASCE)ST.1943-541X.0001942

Main, J.A., 2005. windPRESSURE - DAD software for rigid, gable-roofed buildings [WWW Document]. Natl. Inst. Stand. Technol. Build. Fire Res. Lab. URL https://www.itl.nist.gov/div898/winds/wind_pressure/wind_pressure.htm (accessed 1.15.21).

Main, J.A., Fritz, W.P., 2006. Database-assisted design for wind: Concepts, software, and examples for rigid and flexible buildings. National Institute of Standards and Technology Building and Fire Research Laboratory, Gaithersburg, Maryland.

Main, J.A., 2011. Special-purpose software: MATLAB functions for estimation of peaks from time series [WWW Document]. URL www.itl.nist.gov/div898/winds/homepage.htm (accessed 1.15.21).

Mayer, L.J., 2009. Development of a large-scale tornado simulator. (M.Sc. Dissertation) Texas Tech University.

McDonald, J.R., Mehta, K.C., Mani, S., 2006. A recommendation for an Enhanced Fujita Scale (EF-Scale), Revision 2, Wind Science and Engineering Center, Texas Tech University. Lubbock, Texas.

Mishra, A.R., James, D.L., Letchford, C.W., 2008. Physical simulation of a single-celled tornado-like vortex, Part B: Wind loading on a cubical model. J. Wind Eng. Ind. Aerodyn. 96, 1258–1273. https://doi.org/10.1016/j.jweia.2008.02.027

Nasir, Z., Bitsuamlak, G.T., 2016. Computational modeling of hill effects on tornado like vortex. Proceedings, Annu. Conf. - Can. Soc. Civ. Eng. 3, 1844–1854.

Nasir, Z., 2017. Numerical modeling of tornado-like vortex and its interaction with bluff-bodies 123.

NOAA, 2012. State of the climate: Tornadoes for annual 2011 [WWW Document]. NOAA Natl. Centers Environ. Inf. URL https://www.ncdc.noaa.gov/sotc/tornadoes/201113 (accessed 4.20.20).

NOAA, 2021. Monthly and annual U.S. tornado summaries [WWW Document]. NOAA / Natl. Weather Serv. Strorm Predict. Cent. URL https://www.spc.noaa.gov/climo/online/monthly/newm.html (accessed 6.10.21).

Oh, J.H., Kopp, G.A., Inculet, D.R., 2007. The UWO contribution to the NIST aerodynamic database for wind loads on low buildings: Part 3. Internal pressures. J. Wind Eng. Ind. Aerodyn. 95, 755–779. https://doi.org/10.1016/j.jweia.2007.01.007

Peng, X., Roueche, D.B., Prevatt, D.O., Gurley, K.R., 2016. An engineering-based approach to predict tornado-induced damage, in: Gardoni, P., LaFave, J.M. (Eds.), Multi-Hazard Approaches to Civil Infrastructure Engineering. Springer International Publishing, Switzerland, pp. 311–355. https://doi.org/10.1007/978-3-319-29713-2_15

Prevatt, D.O., van de Lindt, J.W., Back, E.W., Graettinger, A.J., Pei, S., Coulbourne, W., Gupta, R., James, D.L., Agdas, D., 2012a. Making the case for improved structural design: tornado outbreaks of 2011. Leadersh. Manag. Eng. 12, 254–270. https://doi.org/10.1061/(asce)lm.1943-5630.0000192

Prevatt, D.O., Roueche, D.B., Van De Lindt, J.W., Pei, S., Dao, T.N., Coulbourne, W., Graettinger, A.J., Gupta, R., Grau, D., 2012b. Building damage observations and EF classifications from the Tuscaloosa, AL and Joplin, MO tornadoes. ASCE Struct. Congr. 2037–2045.

Razavi, A., Sarkar, P.P., 2018. Tornado-induced wind loads on a low-rise building: Influence of swirl ratio, translation speed and building parameters. Eng. Struct. 167, 1–12. https://doi.org/10.1016/j.engstruct.2018.03.020

Razavi, A., Sarkar, P.P., 2021. Effects of roof geometry on tornado-induced structural actions of a low-rise building. Eng. Struct. 226, 111367. https://doi.org/10.1016/j.engstruct.2020.111367

Refan, M., Hangan, H., Wurman, J., 2014. Reproducing tornadoes in laboratory using proper scaling. J. Wind Eng. Ind. Aerodyn. 135, 136–148. https://doi.org/10.1016/j.jweia.2014.10.008

Refan, M., Hangan, H., 2018. Near surface experimental exploration of tornado vortices. J. Wind Eng. Ind. Aerodyn. 175, 120–135. https://doi.org/10.1016/j.jweia.2018.01.042

Roueche, D.B., Prevatt, D.O., Haan, F.L., Datin, P.L., 2015. An estimate of tornado loads on a wood-frame building using database-assisted design methodology. J. Wind Eng. Ind. Aerodyn. 138, 27–35. https://doi.org/10.1016/j.jweia.2014.11.011

Roueche, D.B., Prevatt, D.O., Haan, F.L., 2020. Tornado-induced and straight-line wind loads on a low-rise building with consideration of internal pressure. Front. Built Environ. 6, 1–18. https://doi.org/10.3389/fbuil.2020.00018

Sabareesh, G.R., Matsui, M., Tamura, Y., 2012. Dependence of surface pressures on a cubic building in tornado like flow on building location and ground roughness. J. Wind Eng. Ind. Aerodyn. 103, 50–59. https://doi.org/10.1016/j.jweia.2012.02.011

Sabareesh, G.R., Matsui, M., Tamura, Y., 2019. Vulnerability of roof and building walls under a translating tornado like vortex. Front. Built Environ. 5, 1–9. https://doi.org/10.3389/fbuil.2019.00053

Sadek, F., Simiu, E., 2002. Peak non-Gaussian wind effects for database-assisted low-rise building design. J. Eng. Mech. 128, 530–539. https://doi.org/10.1061/(asce)0733-9399(2002)128:5(530)

St. Pierre, L.M., Kopp, G.A., Surry, D., Ho, E., 2005. The UWO contribution to the NIST aerodynamic database for wind loads on low buildings: Part 2. Comparison of data with wind load provisions. J. Wind Eng. Ind. Aerodyn. 93, 31–59. https://doi.org/10.1016/j.jweia.2004.07.007

Tecle, A.S., Bitsuamlak, G.T., Chowdhury, A.G., 2015. Opening and compartmentalization effects of internal pressure in low-rise buildings with gable and hip roofs. J. Archit. Eng. 21, 04014002. https://doi.org/10.1061/(asce)ae.1943-5568.0000101

Van De Lindt, J.W., Pei, S., Dao, T.N., Graettinger, A.J., Prevatt, D.O., Gupta, R., Coulbourne, W., 2013. Dual-objective-based tornado design philosophy. J. Struct. Eng. (United States) 139, 251–263. https://doi.org/10.1061/(ASCE)ST.1943-541X.0000622

Vickery, B.J., 1986. Gust-factors for internal-pressures in low rise buildings. J. Wind

Eng. Ind. Aerodyn. 23, 259–271. https://doi.org/10.1016/0167-6105(86)90047-4

Vickery, P., Banik, S., Twisdale, L., 2020. Development of Tornado Design Criteria for Buildings and Shelters Subject to Tornado Induced Loads, in: NIST National Resilience Symposium. U.S. Department of Commerce, Gaithersburg, MD.

Wakimoto, R.M., Stauffer, P., Lee, W.C., Atkins, N.T., Wurman, J., 2012. Finescale structure of the Lagrange, Wyoming, Tornado during VORTEX2: GBVTD and photogrammetric analyses. Mon. Weather Rev. 140, 3397–3418. https://doi.org/10.1175/MWR-D-12-00036.1

Wang, J., Cao, S., Pang, W., Cao, J., Zhao, L., 2016. Wind-load characteristics of a cooling tower exposed to a translating tornado-like vortex. J. Wind Eng. Ind. Aerodyn. 158, 26–36. https://doi.org/10.1016/j.jweia.2016.09.008

Wang, J., Cao, S., Pang, W., Cao, J., 2018. Experimental study on tornado-induced wind pressures on a cubic building with openings. J. Struct. Eng. 144, 04017206. https://doi.org/10.1061/(asce)st.1943-541x.0001952

Wang, J., Cao, S., 2021. Characteristics of tornado wind loads and examinations of tornado wind load provisions in ASCE 7–16. Eng. Struct. 241, 112451. https://doi.org/10.1016/j.engstruct.2021.112451

Chapter 4

4 Tornado Impact on the Component and Cladding Design of a Low-Rise Building

4.1 Introduction

Between the years of 2000 and 2020, over 1200 tornadoes have been recorded annually in the United States, resulting in 74 tornado-related deaths per year (NOAA, 2021). Further, annual insured damages from severe convective storms, which includes tornado events, exceeds those from any other natural catastrophe in the United States, such as tropical cyclones, earthquakes, wildfire, and flooding (Insurance Information Institute, 2020). Tornado windstorm events are also being detected at an increased frequency in Canada, with the Northern Tornado Project at Western University confirming on average 67 tornadoes annually between 2018 and 2020 (Northern Tornado Project, 2021). Although winds from tropical cyclones (which includes hurricanes) dictates the design wind speeds in coastal regions in the United States and eastern Canada, localized convective storms that produce gust fronts, downbursts and tornadoes can be more detrimental in inland regions (Solari et al., 2015).

Tornadoes severity is rated using the Enhanced Fujita (EF) Scale, in which observed damage from post-tornado surveys are used to estimate the wind speeds on a scale from zero to five (McDonald et al., 2006). 94% of tornadoes in the United States are rated with a severity of EF2 or less (NOAA, 2021), and it has also been shown that the majority of structures located outside of the vortex core of very severe EF3 to EF5 tornadoes also experience EF0 to EF2 wind speeds (Prevatt et al., 2012a). Thus, there is growing consensus that in tornado-prone regions, it is reasonable to design structures (especially critical infrastructure) for damage mitigation against tornadoes up to EF2 intensities (Prevatt et al., 2012b; Van De Lindt et al., 2013). This objective is reflected in the current tornado wind load recommendations provided in the commentary of ASCE 7-16 (ASCE, 2017) and has fueled the development of a separate tornado load chapter that is expected to be included in the ASCE 7-22 standard (ASCE, 2021).

Tornadoes have significantly different characteristics from typical atmospheric boundary layer (ABL) winds. Significant vertical wind speed components, rapid changes in atmospheric pressure near the core of the vortex, significant wind field curvature, "nose-like" profiles of the rotational winds, and varying translation speeds are all characteristics of tornadoes that can impact the resulting aerodynamics and load distribution on structures (Kosiba and Wurman, 2013; Lombardo, 2018; Refan and Hangan, 2018; Kopp and Wu, 2020; Ashrafi et al., 2021). There has been a growing body of literature seeking to address the significance of these differences on the resulting tornado load distributions over the exterior building envelope, which would have a direct impact on tornado-resistant component and cladding (C&C) design. Mishra et al. (2008) studied the simulated tornado loading on a cubic building model, highlighting the importance of the atmospheric pressure drop (APD) on tornado-induced loading while also demonstrating the differences in pressure magnitudes and distributions between tornado-induced and ABL winds. Haan et al. (2010) studied the tornado wind loads on a sealed gable roof low-rise building, showing that wind pressures on the roof could be 1.4 to 2.4 times larger than the C&C loads from the ASCE 7-05 standard. An additional study from Haan (2017) demonstrated that by analytically removing the APD from the tornado pressures, the resulting wind loads are reduced but could still be up to 89% larger than ASCE 7 loads in certain roof zones. Kopp and Wu (2020) separated the APD and aerodynamic contributions that make up the external tornado wind loads, showing that there are local deviations in surface pressures caused by the tornado flow versus those from ABL winds, particularly on the leeward walls which experience higher suction forces due to the wind curvature.

A common theme from tornado wind load studies is the significant impact that the APD has on the external load distribution. However, its impact on the net structural loading depends on the rate of pressure equalization across the building envelope, which can be assessed through measurements or estimations of internal pressure (Kikitsu et al., 2011; Letchford et al., 2015; Sabareesh et al., 2019; Roueche et al., 2020; Kassab, 2021; Wang and Cao, 2021). A recent study conducted by Roueche et al. (2020) estimated the internal pressure for cases of both distributed leakage over the building surface and dominant windward or leeward wall openings, showing that peak enveloped net tornado-induced pressures are on average 13% greater than those from straight-line winds but can be up to

twice as large in zones of high flow separation. Further, Wang and Cao (2021) compared enveloped area-averaged net pressures induced by a stationary tornado on a cubic model to the C&C envelope curves derived from the tornado load commentary in ASCE 7-16, showing that there were noteworthy underestimations of pressures on the wall zones by the ASCE standard.

The current literature regarding localized tornado loading has helped to ascertain differences in the pressure distributions between tornado and ABL flows. However, only a few of the studies mentioned above studied building models in large-scale tornado simulators, such as the Wind Engineering, Energy and Environment (WindEEE) Dome, which can simulate large-scale tornadoes at high translation speeds, addressing issues related between the scaling of simulated tornado-like vortices (TLVs) with full-scale events (Refan et al., 2014; Refan and Hangan, 2018; Baker and Sterling, 2019). Further, these large scale simulated TLVs also enable the use of building models with high tap resolutions, which lends itself to detailed studies of tornado loading within specific building zones. Further, in light of the tornado-specific C&C loads being introduced in the draft ASCE 7-22 standard, it would be useful for the engineering design community if an independent analysis of the localized tornado-induced pressure distributions on a low-rise building is conducted in order to comment on the effectiveness of these new ASCE tornado provisions.

This chapter is a continuation of the tornado load analysis carried out in Chapter 3, with a focus on net pressures used for the design of component and cladding elements. The first objective is to determine the unique characteristics of tornado-induced wind loading by differentiating the enveloped distributions of peak net pressures on a low-rise building between measured tornado and ABL wind experimental data. The second goal is to compare the area-averaged peak tornado pressures to the proposed tornado load C&C envelope curves in the draft of ASCE 7-22 to assess its current performance. As was done in Chapter 3, opening configurations corresponding to a perfectly sealed, enclosed, and partially enclosed structure will be considered. The section “Analysis Description” will briefly discuss the experimental data and will describe the area-averaging methodology for obtaining the enveloped peak pressure coefficients. The “Results and Discussion” will

include analysis of peak pressure distributions from the tornado experimental data, ABL wind database, and the ASCE 7-22 C&C tornado clauses. A summary of the major findings is provided in the "Conclusion".

4.2 Analysis Description

4.2.1 External and Internal Pressure Data

External pressure measurements and internal pressure estimates for a low-rise building model subjected to tornado and ABL winds used in Chapter 3 were again utilized herein for the C&C load analysis. The experiments and methods used to obtain these pressures are outlined in detail in Chapter 2 of this thesis, but a brief summary is provided in this section for completeness. Also note that throughout this chapter, "TLV" and "tornado" will be used interchangeably for conciseness and ease of reading.

The low-rise building used in this C&C load investigation corresponded to "Building 3" from the National Institute of Standards and Technology (NIST) aerodynamic database, with full-scale plan dimensions of 38.1 m by 24.4 m, an eave height of 12.2 m, and a gable roof with a slope of 3:12 (14.4°) (Ho et al., 2005). A simulated tornado with a swirl ratio ($S = \frac{r_0 \Gamma_{\max}}{2Qh}$) of 0.76, core radius ($R_C$) of 0.60 m, aspect ratio ($a = \frac{h}{r_0}$) of 0.35, and radial Reynolds number ($Re_r = \frac{Q}{2\pi v}$) of 10^6 was produced in the WindEEE Dome facility, where r_0 is the updraft radius, h is the inflow depth, Γ_{max} is the maximum circulation in the flow, Q is the flow rate per unit axial length, v is the kinematic viscosity, and ρ is the density of air. The tornado was translated by a 1:200 scale model of the building at a speed, V_t, of 1.5 m/s in smooth terrain. External tornado pressures were measured by 360 taps on the building surface at a sampling rate of 500 Hz. External ABL wind pressures were obtained for the same building model geometry from the NIST aerodynamic database, which were measured at the Boundary Layer Wind Tunnel II at Western University (Ho et al., 2005). The pressure data was obtained from 677 taps distributed over the building surface subjected to open terrain winds. Test schematics are displayed in Figure 4.1 and Figure 4.2, while Table 2.3 provides a comparison between the two sets of aerodynamic data with additional details included.

(a)

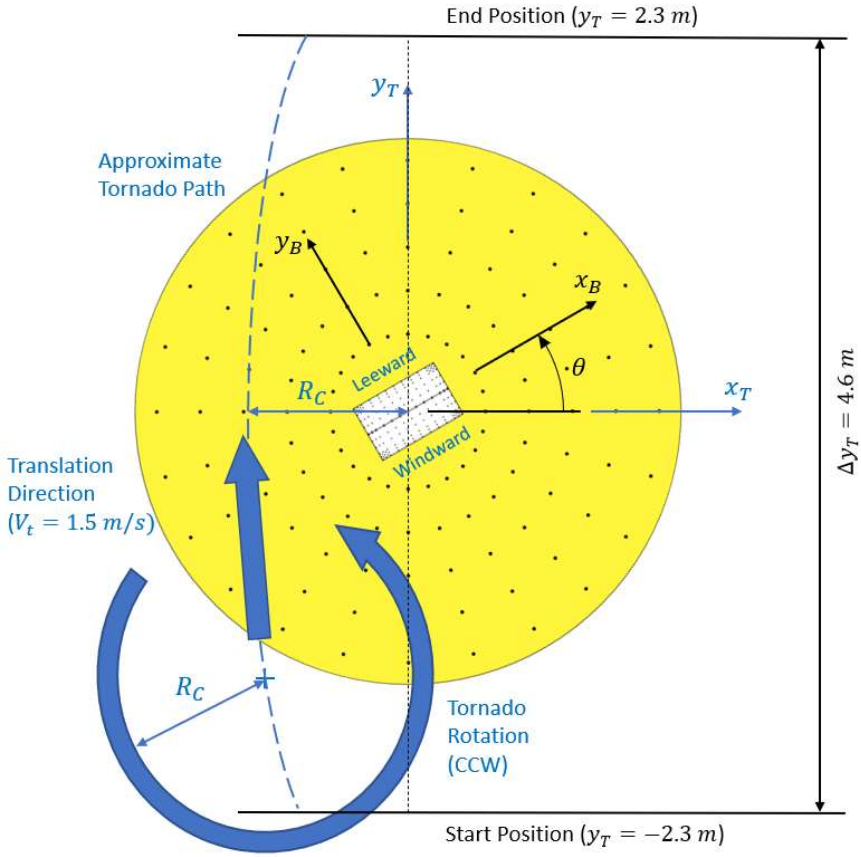

(b)

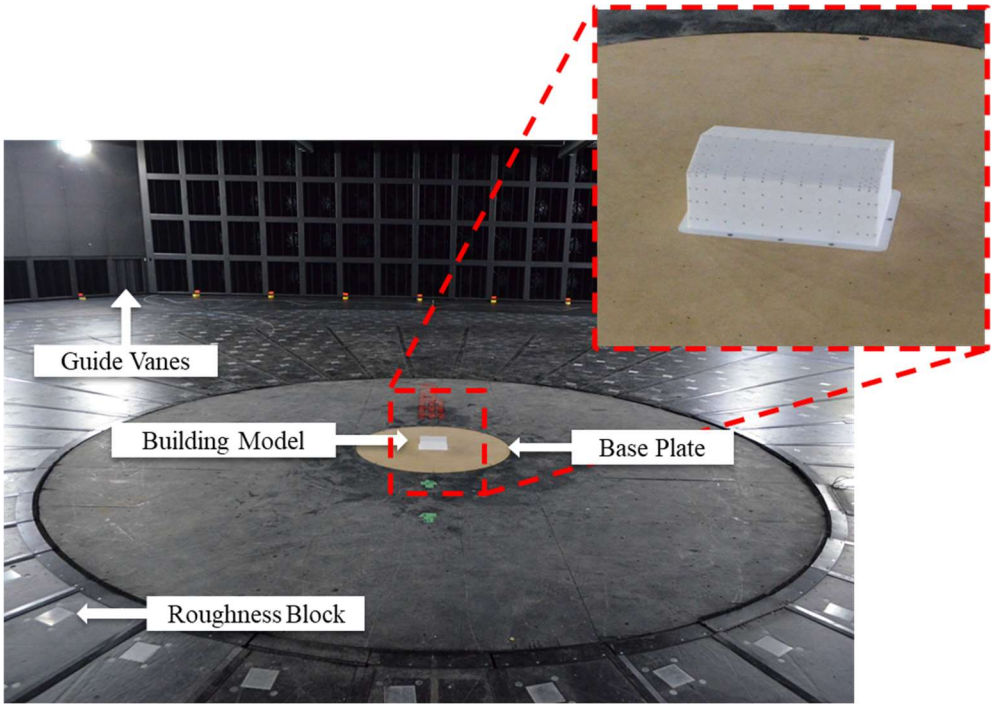

Figure 4.1: (a) Test schematic for a translating tornado in the WindEEE Dome. (b) Image of the tornado test setup in the WindEEE Dome chamber.

(a)

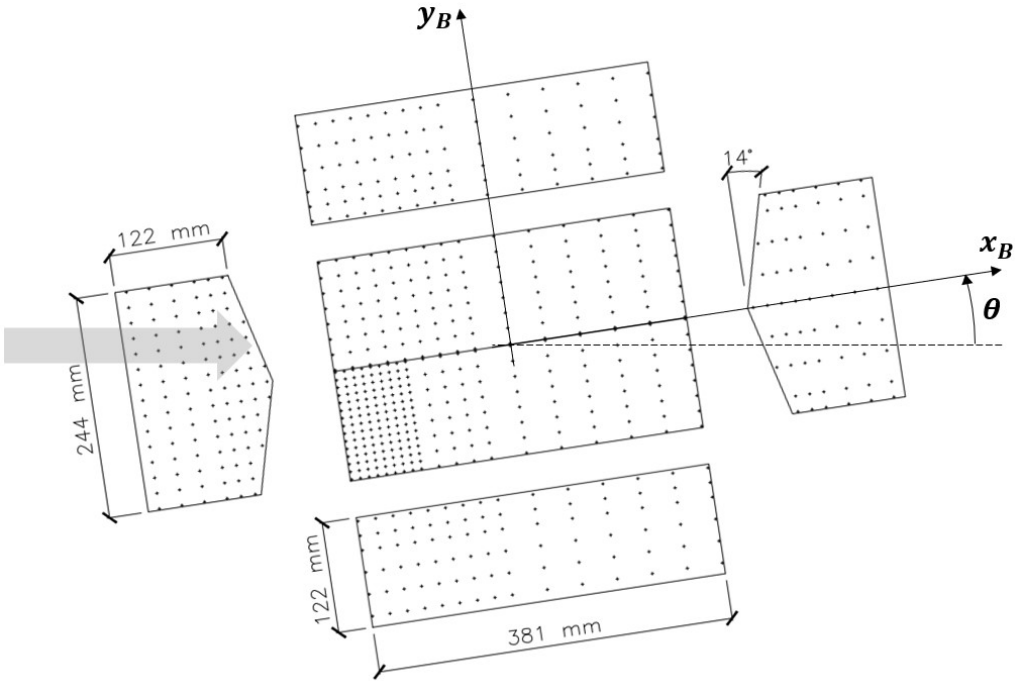

(b)

Figure 4.2: (a) Layout of the "Building 3" model from the NIST ABL wind aerodynamic database. The grey arrow indicates the inflow ABL wind direction. (b) Image of the ABL test setup in the Boundary Layer Wind Tunnel (Ho et al., 2003).

Table 4.1: Comparison of wind tunnel test parameters between the WindEEE Dome (TLV) and the NIST Aerodynamic Database (ABL Wind).

Parameter	WindEEE (TLV)	NIST (ABL)
Length Scale (λ_L)	1:200	1:100
Velocity Scale (λ_V)	1:3.0	1:2.8
Time Scale (λ_T)	3:200	1:36
Model Dimensions	191 mm x 122 mm x 61 mm eave height	381 mm x 244 mm x 122 mm eave height
Roof Shape	Gable, 14° roof slope	Gable, 14° roof slope
Building Orientations (θ)	0° to 90° (45° increments)	180° to 345° (15° increments)
Test Repetitions	10	1
Sampling Frequency	500 Hz	500 Hz
Test Duration	15 sec	100 sec
Exposure	Open	Open ($z_0 = 0.03\ m$)
Number of Taps	360	677
Reference Velocity	3-sec gust velocity at mean roof height	3600-sec average velocity at mean roof height

External pressure measurements from both datasets were non-dimensionalized into pressure coefficients, $C_{Pe,eq}(t,\theta)$, which were defined in Equation 4.1 as follows:

$$C_{Pe,eq}(t,\theta) = \frac{p_e(t,\theta) - p_0}{\frac{1}{2}\rho V_{ref}^2} \tag{4.1}$$

where p_0 is the ambient static pressure, ρ is the density of air and V_{ref} is the standard reference velocity, defined herein as the peak 3-second gust (in full-scale time) horizontal velocity at the mean roof height, h, in open terrain. In the case of the tornado pressure coefficients, $C_{Pe,TLV}(t,\theta)$, the refence velocity matched the standard definition employed in this study, meaning $C_{Pe,TLV}(t,\theta) = C_{Pe,eq}(t,\theta)$. Since the NIST aerodynamic database pressure coefficients were referenced to a mean hourly wind speed at the mean roof height in open terrain ($V_{3600\,s,h,open}$), they needed to be converted to a 3-second gust velocity. This averaging time adjustment was made using the Durst Curve (Durst, 1960). Therefore,

the ABL wind tunnel external pressure coefficients, $C_{Pe,ABL}$, were converted to equivalent pressure coefficients using a wind tunnel factor, $F_{WT,NIST}$, as defined by St. Pierre et al. (2005):

$$C_{Pe,eq}(t,\theta) = F_{WT,NIST} * C_{Pe,ABL}(t,\theta) = \left(\frac{V_{3600\ s,h,open}}{V_{3\ s,h,open}}\right)^2 * C_{Pe,ABL}(t,\theta) \qquad (4.2)$$

In this case, the resulting wind tunnel factor was equal 0.43, with no adjustments needed to be made to account for terrain or wind speed reference height between the two tests. With respect to the differences in tap layout and density between the two tests, the NIST aerodynamic pressures were interpolated and resampled to match the tap layout from the WindEEE Dome model using the Nearest-Neighbour interpolation scheme implemented through the "*scatteredInterpolant*" function in MATLAB (Amidror, 2002).

Three opening cases were assumed across the building envelope, corresponding to the definitions provided in Table 26.13-1 in ASCE 7-16 and the proposed ASCE 7-22 for a perfectly sealed building, enclosed building, and partially enclosed building, with details provided in Table 3.2 and schematically in Figure 4.3. The dominant opening dimensions and position utilized to represent a partially enclosed building were the same as those utilized for models of comparable dimensions in the NIST database by Oh et al. (2007).

Table 4.2: Summary of the internal pressure opening cases for the low-rise building.

Opening Description	Dimensions (Full-Scale)	Porosity Ratio*
Perfectly Sealed	No openings	0 %
Enclosed	80 holes, $\emptyset = 0.202$ m	0.1 %
Partially Enclosed	8.13 m x 1.91 m (L x W)	3.3 %

** Porosity Ratio corresponds to the opening area divided by the corresponding building surface area.*

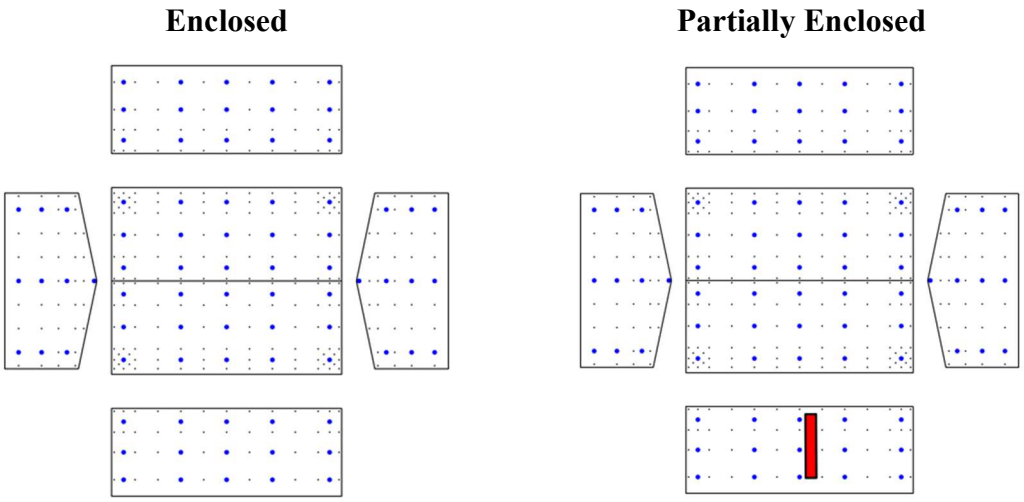

Figure 4.3: Schematics of the enclosed opening case with 80 holes distributed over the building walls (indicated by the blue dots) and the partially enclosed case with an 8.13 x 1.91 m dominant opening on the predominantly windward face of the building (shown by the red rectangle).

The internal pressures for these opening configurations were estimated using the Multiple Discharge Equations (MDE's) for unsteady, incompressible flow. Time histories of net pressure coefficients, $C_{P,net}(t,\theta)$, required for the analysis were computed from the external and internal pressure coefficients using Equation 4.3.

$$C_{P,eq}(t,\theta) = C_{Pe,eq}(t,\theta) - C_{Pi,eq}(t,\theta) \tag{4.3}$$

Peak pressure coefficients were estimated using statistical methods, which are critical for determining stable estimates of the component and cladding design pressures. For the WindEEE tornado test data, the peak pressure coefficients at an individual tap for a given building orientation, denoted as $\hat{C}_{P,eq,TLV}(\theta)$, is defined by Equation 4.4:

$$\hat{C}_{P,eq,TLV}(\theta) = \underset{r=1..10}{\text{median}}\, \hat{C}_{P,eq,TLV,r}\,(\theta) \tag{4.4}$$

where $\hat{C}_{P,eq,TLV,r}(\theta)$ is the ordered set of the peak equivalent pressure coefficients at a specific tap for each tornado translation run, r. The peak pressure coefficients from the

ABL wind data for each building orientation, $\hat{C}_{P,eq,ABL}(\theta)$, were estimated using a Type I (Gumbel) Extreme Value distribution, which takes the following form:

$$\hat{C}_{P,eq,ABL}(\theta) = F\left(C_{P,eq,ABL}(\theta) = 0.577\right) \tag{4.5a}$$

$$F\left(C_{P,eq,ABL}(\theta)\right) = exp\left(-exp\left(-\frac{C_{P,eq,ABL}(\theta) - \mu}{\beta}\right)\right) \tag{4.5b}$$

where μ is the location parameter and β is the scale parameter. These parameters were obtained using the general translation method proposed by Sadek and Simiu (2002), which was implemented using the NIST "*maxminest"* MATLAB function developed by Main (2011). In this study, $\hat{C}_{P,eq,ABL}(\theta)$ was taken as the 57th percentile of the Gumbel distribution for a one-hour storm duration, for which there is precedence to use from the literature (Davenport, 1964; Gierson et al., 2017; Simiu et al., 2017).

4.2.2 Component and Cladding Wind Loads in ASCE 7-22

The proposed tornado chapter (Chapter 32) in the new ASCE 7-22 standard specifies tornado loads for C&C elements. The tornado design pressure, p, for the C&C is defined as follows:

$$p = \left(\frac{1}{2}\rho K_{zTor} K_e V_T^2\right)\left(K_{dT} K_{vT} GC_p - GC_{piT}\right) \tag{4.6}$$

where ρ is the air density, V_T^2 is the 3-sec gust horizontal tornado wind speed obtained at a height of 10 m independent of terrain, K_{zTor} is the tornado velocity pressure exposure coefficient, K_e is the ground elevation factor, K_{dT} is the tornado directionality factor, K_{vT} is a pressure coefficient modification factor to account for winds in the vertical-direction, GC_P is the external pressure coefficient, and GC_{piT} is the tornado internal pressure coefficient.

The mean roof height of the building under study was 13.7 m, which is less than 18.0 m, meaning the structure was classified as a low-rise building in ASCE 7-22. Chapter 30 in the ASCE standard provides GC_P envelope curves for different zones on the walls and roof of a low-rise building, as shown by Figure 4.4. Since the roof slope of the building

was 14.4°, the external pressure coefficients envelope curves corresponded to those provided by Figure 30.3-1 for wall zones and Figure 30.3-2B for roof zones within Chapter 30 of ASCE 7-22. The dimension "a" was equivalent to 2.44 m, defined as the smaller of 10% of the least horizontal dimension or 0.4h, but not less than 4% of the least horizontal dimension or 0.9 m. It is noted that for the comparison, the "a" dimension that defines the roof edge zones were slightly extended by 0.53 m (from an original 2.44 m) in order to remove some bias caused by the tap layout. The design GC_P envelope curves for the wall and roof zones are provided in Figure 4.5, which are defined as a function of averaging area (i.e. the area of the cladding element or tributary area of the component to be designed). These curves were developed by enveloping the peak pressure coefficients measured in ABL wind tunnel tests for multiple low-rise building geometries (Kopp and Morrison, 2014).

The internal pressure coefficients provided in ASCE 7-22 includes the effects of both aerodynamically induced internal pressures and the atmospheric pressure drop (APD). Therefore, values of $GC_{P_i} = +1.0$ were utilized for a perfectly sealed building, $GC_{P_i} = -0.18$ to $+0.55$ for an enclosed building, and $GC_{P_i} = \pm 0.55$ for a partially enclosed building. Further, the design wind pressure factors were determined to be the following when considering the study building dimensions:

- K_{zTor} equaled 1.0 for a mean roof height of 13.7 m based on the proposed tornado wind profile.
- K_e equaled 1.0 as no adjustment is needed for air density.
- K_{dT} was assumed to be 1.0 for the C&C tornado pressures used in this analysis by treating the entire building as an essential facility.
- K_{vT} equaled 1.2 for the negative pressures acting on roof zones 1 and 2, 1.3 for negative pressures acting on roof zone 3, and 1.0 for negative pressures on the walls and positive pressures for all wall and roof zones.

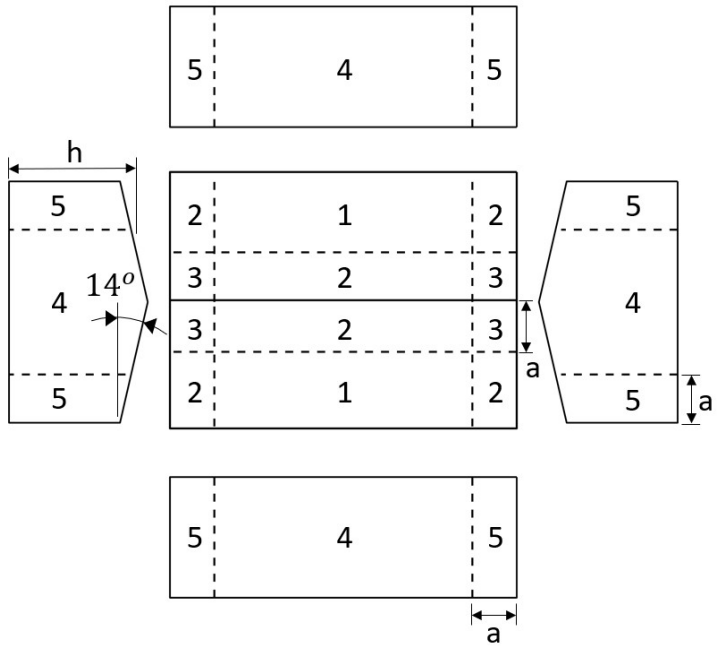

Figure 4.4: Component and cladding pressure coefficient zones provided by Figures 30.3-1 and 30.3-2B in ASCE 7-22 for a low rise, gable roof building with a roof slope between 7º and 20º.

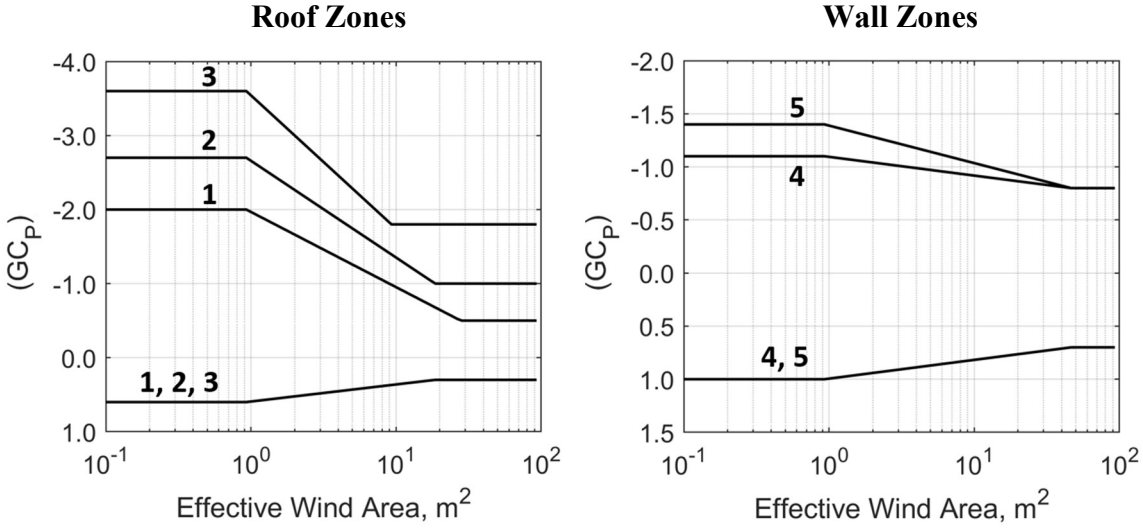

Figure 4.5: External pressure coefficient, GC_P, envelope curves provided by ASCE 7-22 for the roof zones (defined by Figure 30.3-2B) and wall zones (defined by Figure 30.3-1).

4.3 Results and Discussion

4.3.1 Enveloped Tornado and ABL Peak Pressures

The subsequent sections compare the enveloped peak pressure coefficients over all original and reflected building orientations. In the case of the tornado loads, this meant enveloping the set of peak coefficients over the three building orientations with measured data (0º, 45º, and 90º) and reflected building orientations (180º, 225º, and 270º). For the ABL winds, the enveloped peak pressure coefficients corresponded to enveloping the peaks over the original building orientations (180º to 345º at 15º increments) and reflected orientations (0º to 165º at 15º increments). Schematics of the enveloping assumptions are shown in Figure 4.6 for both the tornado and ABL flows, with the additional consideration of the reflected single dominant opening for the partially enclosed building also depicted. The discussion will be limited only to the minimum peak pressures, which are typically larger in magnitude than the positive pressures.

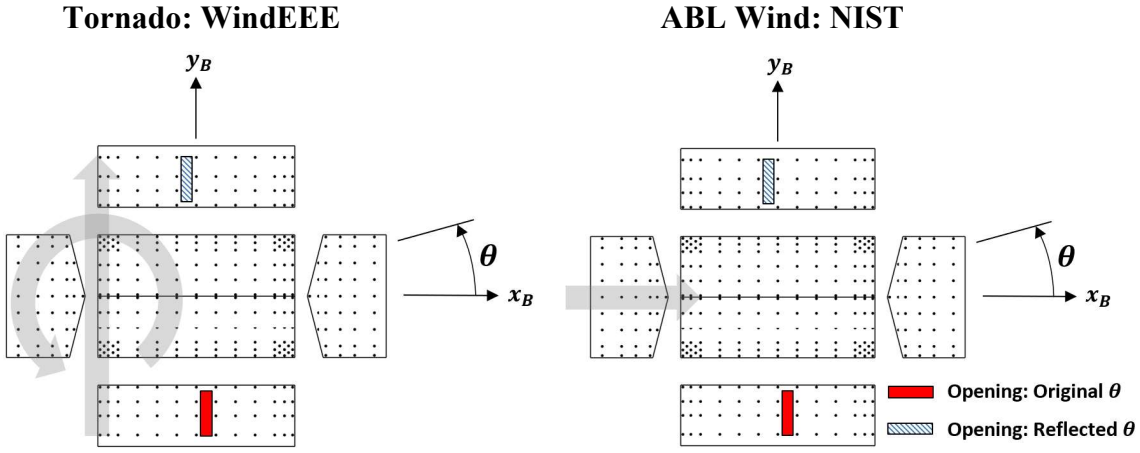

Figure 4.6: Diagram showing position of dominant opening for original (i.e. measured) and reflected building orientations for determining enveloped peak pressures for a partially enclosed building.

Figure 4.7 provides both contour and scatter plots comparing the peak enveloped pressure coefficients at each tap location between the WindEEE tornado and NIST ABL datasets for the case of a perfectly sealed building. This means that the net peak pressures are equivalent to the external pressures in this case. The ASCE 7-22 C&C pressure coefficient zones have also been overlaid on the enveloped peak pressure contour plots. It

is clearly shown by both the contour and scatter plots that the peak minimum pressures induced by the tornado are larger in magnitude than those from ABL winds. These differences are quantitatively reflected by a significant skew of the scatter data away from the "unity" line favouring the tornado pressures. This trend suggests that the atmospheric pressure drop (APD) plays a large role in the consistent differences in peak pressures between the tornado and ABL wind data for the perfectly sealed building.

Figure 4.8 displays the contour and scatter plots of the enveloped peak minimum pressure coefficients for the enclosed building configuration, where internal pressures are considered in the computation of net pressures in accordance with Equation 4.3. The scatter data is distributed on both sides of the unity line, suggesting that the influence of the APD on the peak net pressures is not as significant once openings are present in the building envelope. For the case of an enclosed building with a dominant windward opening depicted in Figure 4.9, there is a negative shift in the peak pressure coefficients for both flow regimes, which can be attributed to the observed rise in internal pressure as the wind impinges on the windward dominant opening and pressurizes the internal volume. A slight skew of the peak pressure coefficients towards the tornado values may also indicate that the wind flow near the vortex core (which is characterized by high turbulence and multiple sub-vortices) induces larger internal pressures versus ABL flow, resulting in larger magnitudes of peak negative pressures. This mechanism would fall in line with similar observations by Jaffe and Kopp (2021) for tornado-induced pressures on a low-rise building with a dominant opening.

There are notable local differences in the distributions of the peak minimum pressure coefficients between both datasets, which are most clearly highlighted in Figure 4.8 for the enclosed building. The contour plot reveals regions of high suction pressures near the roof corners for the tornado-induced flow, which can be attributed to presence of conical vortices. This region of high suction pressures also extends along the roof edge into "Zone 1", which does not occur for the ABL peak pressures. The scatter plot quantitatively indicates that the peak pressure coefficients from the tornado winds in these corner regions are 2 to 2.5 times larger in magnitude than those from ABL winds, which agrees with the results from a similar comparison conducted by Roueche et al. (2020). A slight increase in

the peak suction pressure coefficients is also noted in the interior roof region under the tornado flow, which may be due to the significant vertical winds causing additional uplift loads on the roof. Conversely, the contour and scatter data for the enclosed building revealed that the magnitudes of the ABL-induced peak minimum pressures exceeded those from the simulated tornadoes near the roof ridge near the gable ends by up to 40%. Comparisons of the peak enveloped minimum wall pressures reveal that there are higher magnitude negative pressures caused by the tornado winds in the regions of flow separation at the wall edges, which falls in line with observations from literature for other low-rise building tests (Roueche et al., 2020; Wang and Cao, 2021). There is also a region of high negative pressure in the interior wall Zone 4 that is most easily identified in Figure 4.9 for the partially enclosed building. This negative pressure region could have been caused by enhanced flow separations on the leeward walls due to the wind flow curvature in tornadoes, which was also noted in other studies for similar TLV characteristics (Kopp and Wu, 2020; Kassab, 2021). Due to variations in tornado structures, simulator characteristics, swirl ratio definitions and building sizes, it is difficult to make direct quantitative comparisons of the results to other studies.

Opening Condition: Perfectly Sealed

TLV: WindEEE	ABL: NIST

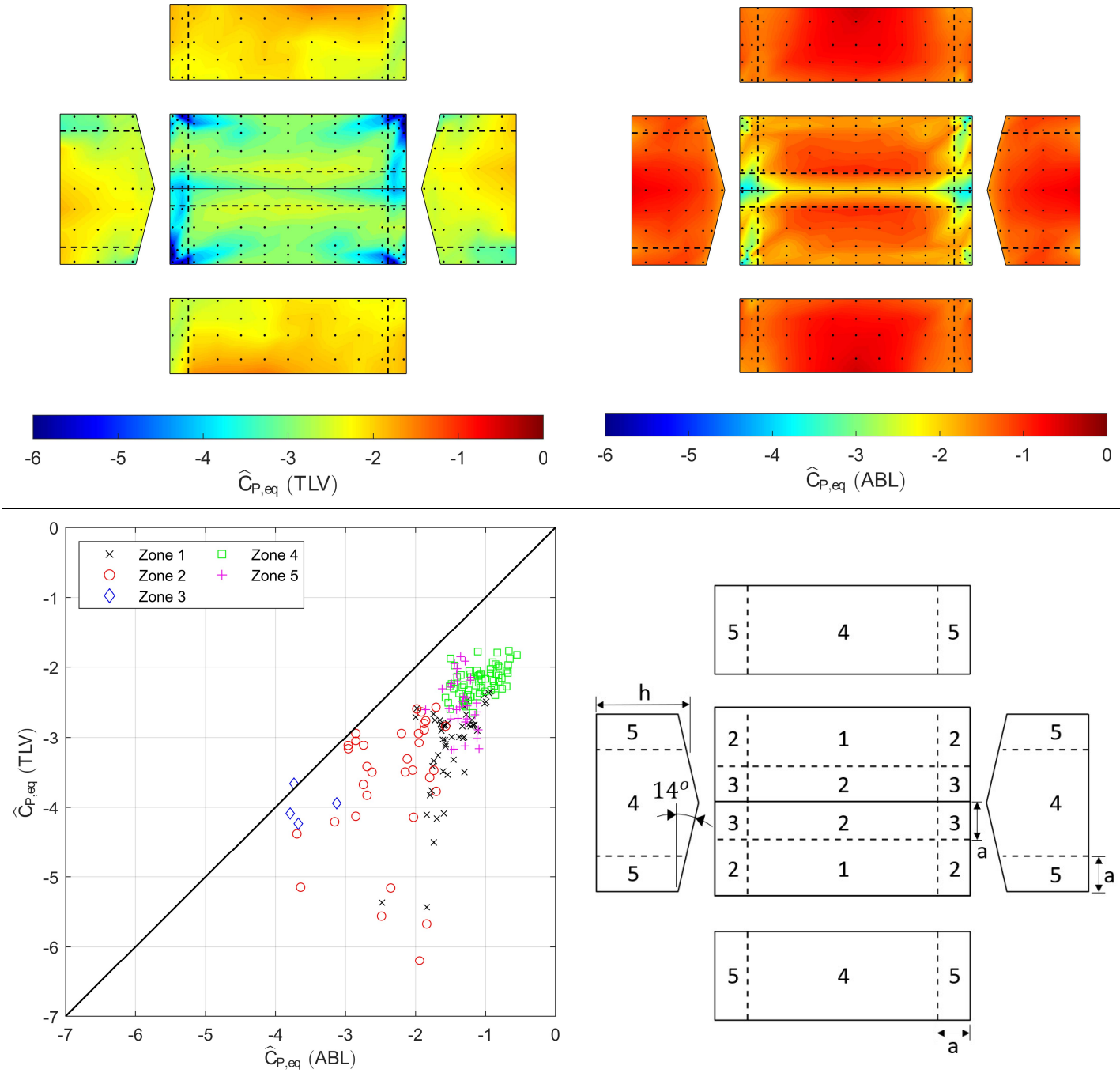

Figure 4.7: Contour and scatter plots comparing the peak minimum enveloped pressure coefficients between tornado and ABL wind flows for a perfectly sealed building.

Opening Condition: Enclosed

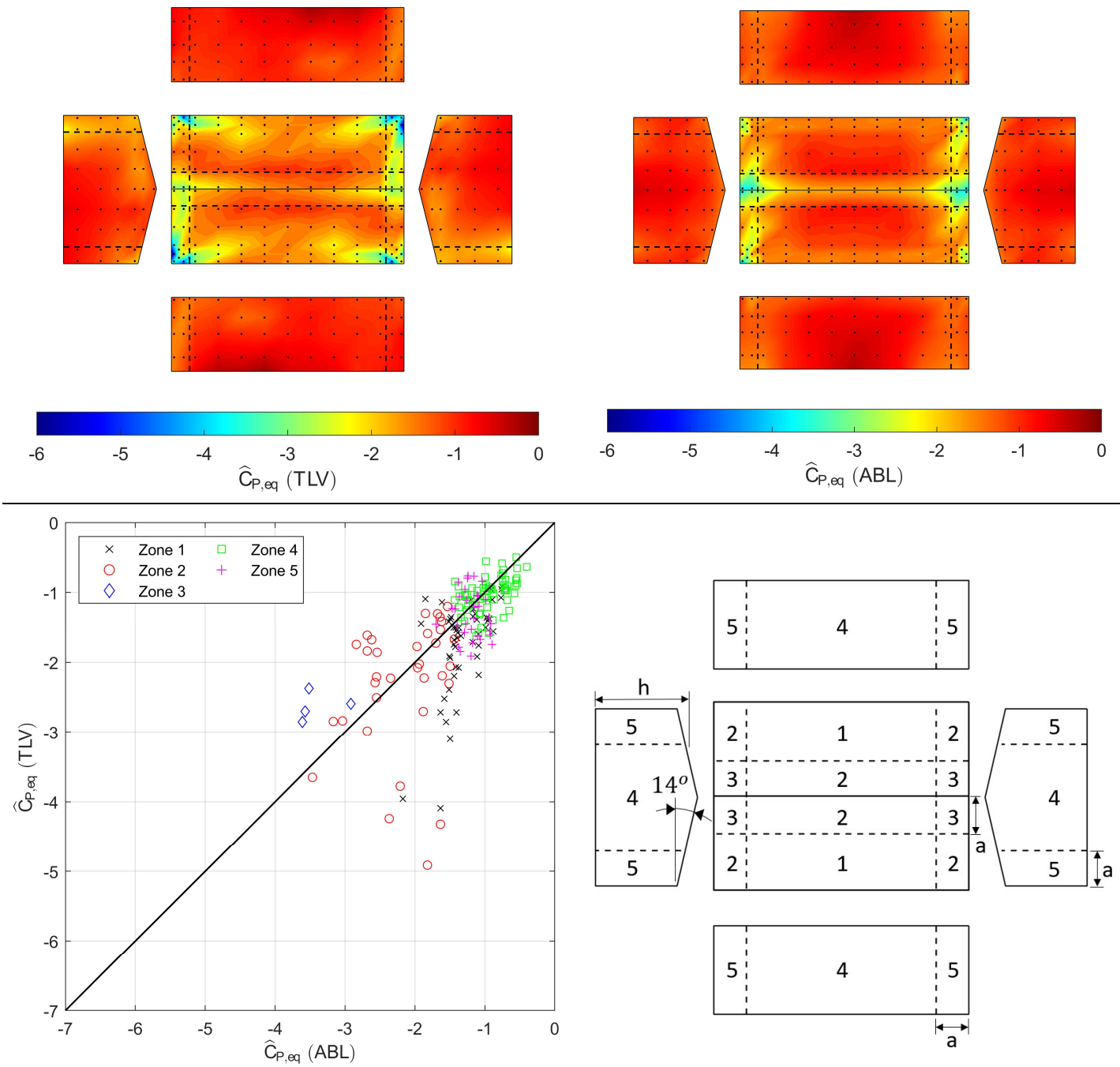

Figure 4.8: Contour and scatter plots comparing the peak minimum enveloped pressure coefficients between tornado and ABL wind flows for an enclosed building.

Opening Condition: Partially Enclosed

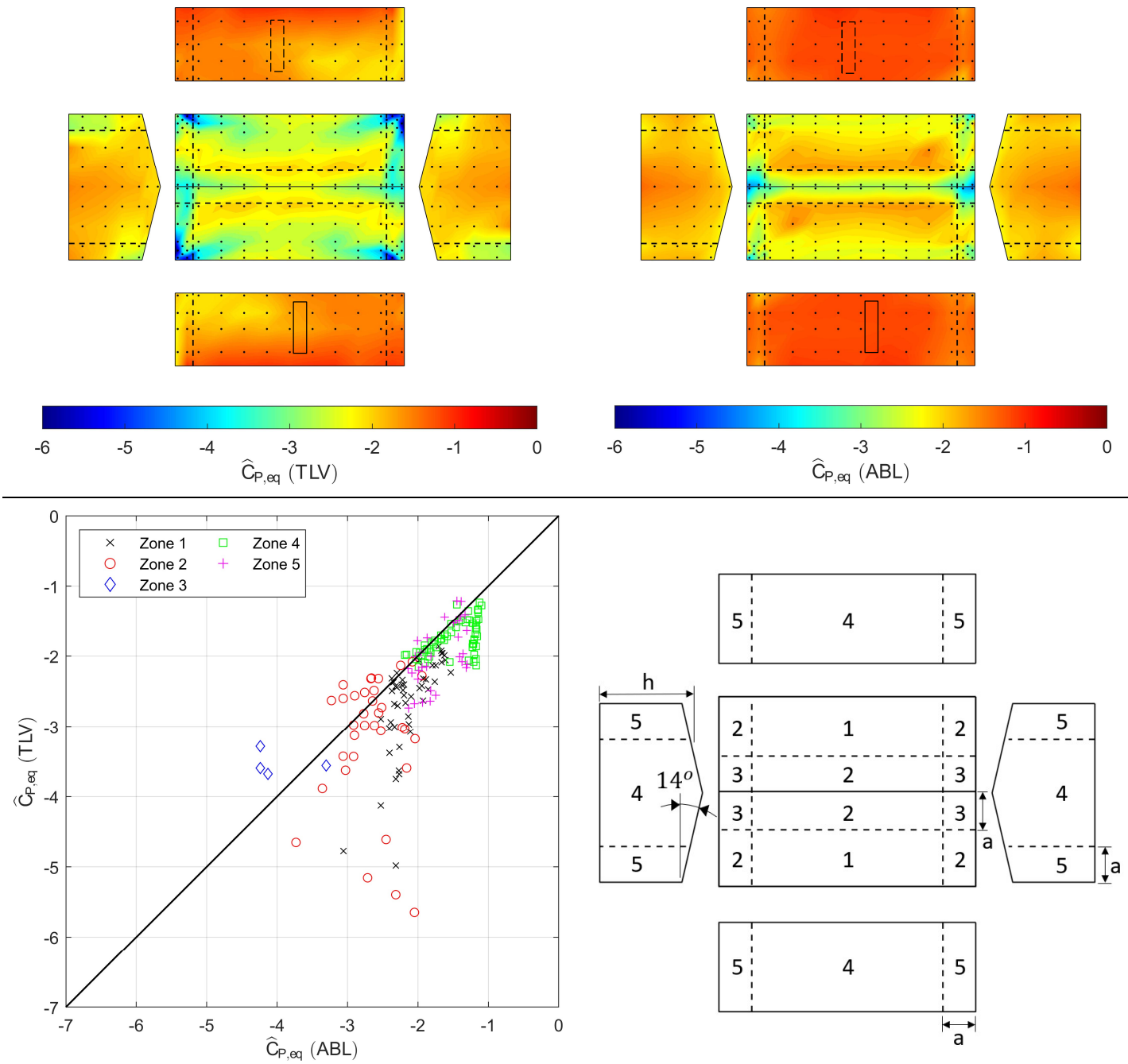

Figure 4.9: Contour and scatter plots comparing the peak minimum enveloped pressure coefficients between tornado and ABL wind flows for a partially enclosed building.

The differences in peak pressure coefficients between tornado and ABL-induced loading is further illustrated by Figure 4.10 and Figure 4.11, which show the distributions of the minimum peaks for a column of pressure taps along the building mid-section and end-zones, respectively. The ABL pressure coefficient data corresponds to the statistical peaks computed from the Type I Extreme Value Distribution, while the tornado data is represented by the statistical peak (median) and spread of the observed peaks used to compute the median, represented here by error bars for the 10^{th} and 90^{th} percentiles of the ten sample peaks for the critical building orientation. The distributions of the peaks for a perfectly sealed building in both figures reinforces the trends observed in the contour and scatter data, showing the overall exceedance in magnitudes of tornado-induced peak minimum pressures versus those from ABL winds. From the enclosed and partially enclosed opening cases, the mid-section taps highlight the exceedance of tornado-induced minimum pressure magnitudes along the building walls and roof interior, while the ABL-induced pressures are larger at the roof edge. Further, for the column of end-zone taps, there is a clear indication of the large suction pressures induced by the tornado in the roof corner zones compared to the corner peak suction pressures from the ABL winds.

The comparison conducted herein is highly conditioned upon the peak tornado pressure coefficients used, which have a variety of limitations that need to be considered. First, no standard definition exists for the reference velocity and reference static pressure used to calculate the non-dimensional pressure coefficients in tornado flows. Kopp and Wu (2020) demonstrated a methodology for simultaneous pressure and velocity measurement, which is standard practice in ABL wind tunnel tests, but challenges associated with cobra probe positioning and re-orientation are limiting barriers that need to be resolved. It is also recognized that the tap distribution used herein may not have fully captured the tornado-induced loads in separation zones, particular near the roof ridge where the largest ABL-induced suction loads were observed. Finally, further study is required to determine statistical methods for peak pressure estimations in tornado-like flows, which can help to aid in comparisons made with the peak ABL-induced pressure coefficients.

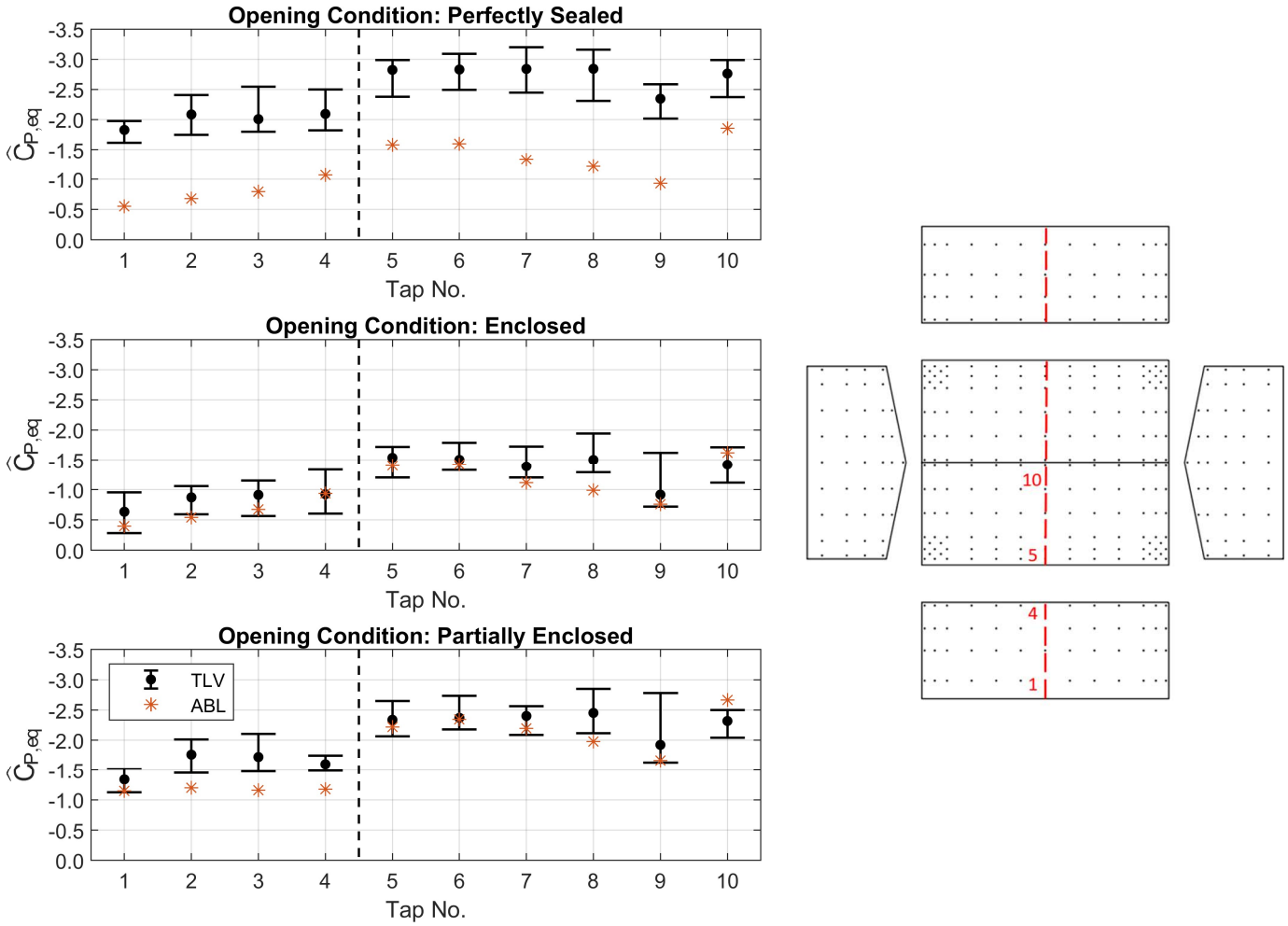

Figure 4.10: Comparison of the peak negative enveloped pressure coefficients between the tornado and ABL wind flows for a perfectly sealed, enclosed, and partially enclosed building along a row of pressure taps at the model mid-section. The bars represent the 10th and 90th percentiles of the of the set of observed peak pressure coefficients for each building orientation.

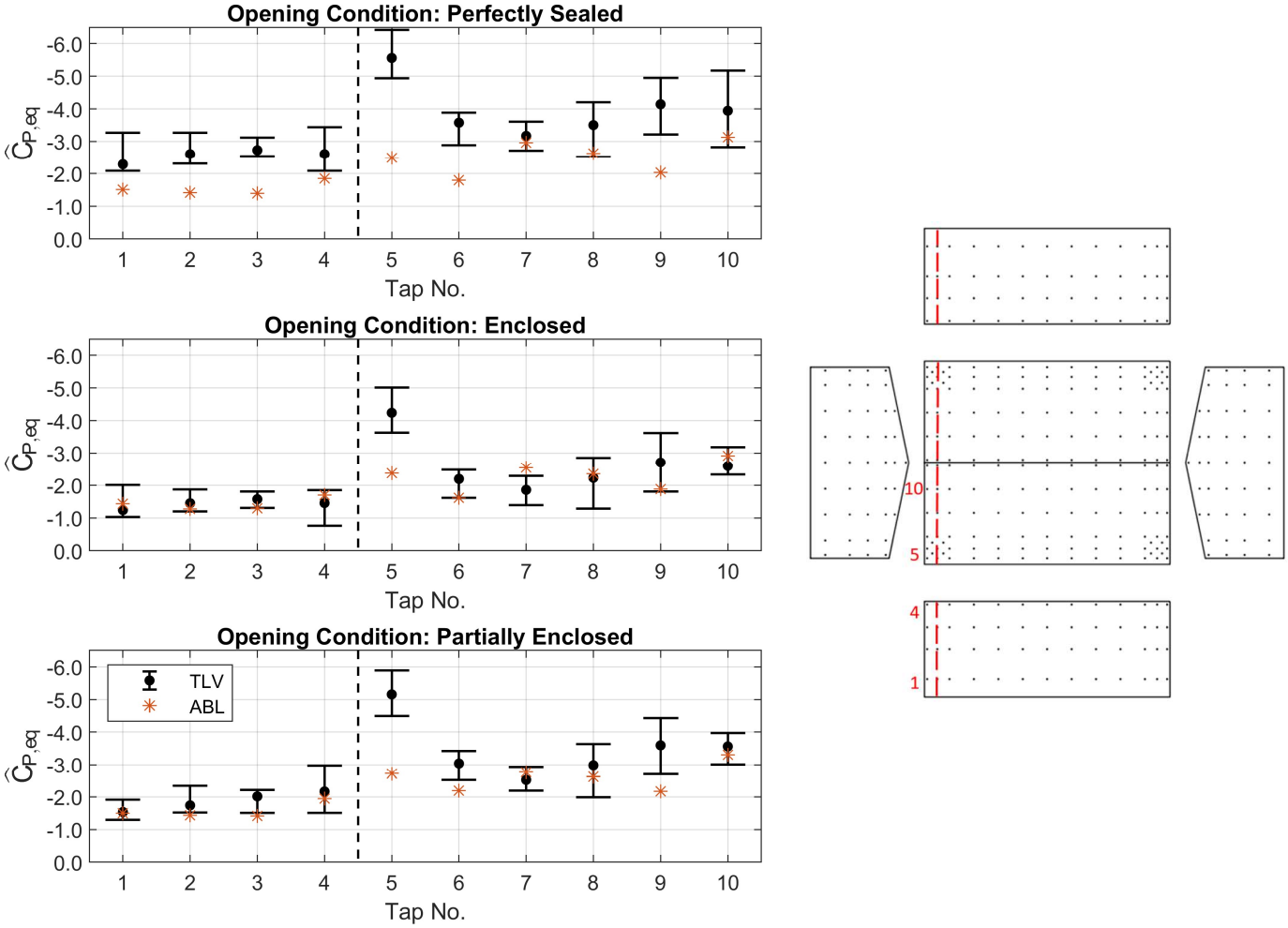

Figure 4.11: Comparison of the peak negative enveloped pressure coefficients between the tornado and ABL wind flows for a perfectly sealed, enclosed, and partially enclosed building along a row of roof edge pressure taps. The bars represent the 10th and 90th percentiles of the of the set of observed peak pressure coefficients for each building orientation.

4.3.2 Enveloped Tornado and ASCE 7-22 Peak Pressures

The second set of comparisons involves the peak enveloped pressure coefficients from the WindEEE tornado tests and the design curves from ASCE 7-22. To facilitate this analysis, modifications to the ASCE 7-22 design pressure coefficients must be made. A useful formula to modify the pressure coefficients is again adapted from St. Pierre et al. (2005) as shown in Equation 4.7.

$$\hat{C}_{P,eq} = \frac{\left(\frac{1}{2}\rho K_{zTor} K_e V_T^2\right)\left(K_{dT} K_{vT} G C_p - G C_{piT}\right)}{\frac{1}{2}\rho V_{ref,TLV}^2} \tag{4.7a}$$

$$\hat{C}_{P,eq} = F_{WT,ASCE}\left(K_{dT} K_{vT} G C_p - G C_{piT}\right) \tag{4.7b}$$

In this formulation, $\hat{C}_{P,eq}$ is the equivalent net peak pressure coefficient, $V_{ref,TLV}$ is the 3-second gust reference wind velocity measured at the mean roof height in the tornado wind test, $F_{WT,ASCE}$ is a wind tunnel factor applied to the external and internal pressure coefficients from ASCE 7-22, and all other terms are defined back in Equation 4.6. The value of $F_{WT,ASCE}$ is equal to 1.0 in this case since the definitions of V_T and $V_{ref,TLV}$ both correspond to 3-second horizontal wind gusts, while K_{zTor} and K_e both equal 1.0 as explained in Section 4.2.2.

4.3.2.1 Area-Averaging Procedure

To produce enveloped $\hat{C}_{P,eq}$ data as a function of area from the WindEEE tests for comparison to ASCE 7-22, an area-averaging procedure needed to be implemented. The algorithm used herein is adapted from procedures found in the literature (Duthinh et al., 2015; Gierson et al., 2017). The averaging areas consisted of a grid of cells that were overlaid on top of the tributary areas of each pressure tap, as shown in Figure 4.12. Highlights of the algorithm are as follows:

- The minimum averaging cell size was based on the minimum of the x- and y-direction tap spacings on each building face.

- The maximum averaging cell size was the largest area of interest from the ASCE envelope curves for each building zone.
- The aspect ratio of the averaging cells (i.e. cell length divided by cell width) was fixed at either one or two, with the cell length oriented along either the x- or y-axis of each building face.
- Each building face corner along with the centre was used as a base point for the averaging cell grid generation in order to capture the highest peak pressures.

Time histories of pressure coefficients were computed for each averaging cell using a weighted average governed by the ratios of pressure tap tributary areas contained within each cell. As has been done throughout this chapter, the peak pressure coefficients for each building orientation were taken as the median value from the ten peak pressures obtained from the repeated test runs. To create a fair comparison to the ASCE envelope curves, the boundaries from the ASCE wall zones were slightly adjusted such that the pressure tap tributary areas used in the algorithm only belonged to the taps contained within each zone. It is noted that unlike prior studies on NIST database models where at least four pressure taps were contained in each area-averaging zone (Kopp and Morrison, 2018), only one tap was used in some instances in order to compute peak pressure coefficients corresponding to the smaller area sizes.

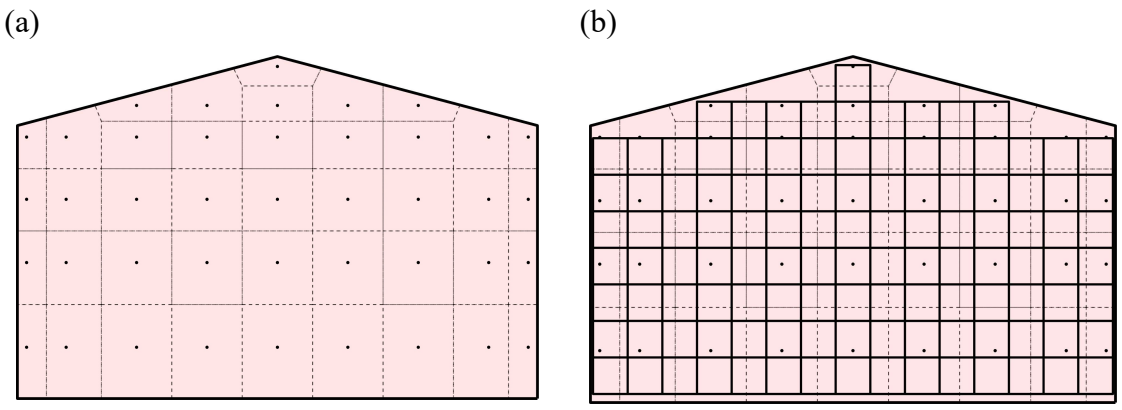

Figure 4.12: (a) Pressure taps and their tributary areas for the end walls of the building model. (b) Overlaid area-averaging cell grid corresponding to a cell aspect ratio of one.

4.3.2.2 Results

Figure 4.13 to Figure 4.15 present a comparison of the scattered peak area-averaged minimum pressure coefficients for various averaging cell sizes from the WindEEE tests to the ASCE 7-22 design pressure coefficient envelope curves for the specified wall and roof zones from Chapter 30 of the standard. The ASCE envelope curves were derived from the worst-case net pressure coefficients, which corresponded to an internal pressure, GC_{piT}, of $+1.0$ for a perfectly sealed building and $+0.55$ for both the enclosed and partially enclosed buildings.

For the case of a perfectly sealed building, referring to Figure 4.13, the ASCE 7-22 envelope curves are exceeded in all zones except for Zone 3. As discussed in the comparison to the NIST ABL peak pressures, the ABL-induced pressures were larger than the tornado pressures within Zone 3 at the roof ridge and corners. Since the ASCE Zones are derived from the same ABL wind datasets with an additional factor of 1.3 applied to winds in this zone to account for additional uplift, it is sensible why the ASCE envelope curve far exceeds the peak minimum pressure coefficients from the tornado experiment. At all other zones, there is a consistent exceedance of the tornado peak pressure coefficients versus the ASCE envelope curves despite the use of an internal pressure coefficient of +1.0 to account for the influence of the APD. It was observed from the scatter data presented in Figure 4.7 comparing the peak tornado and ABL pressures that a significant number of tornado-induced pressures fell below the best-fit line of the data in these C&C zones. This implies that the vertical wind factor, K_{zT}, might not be large enough to account for the increase in tornado-induced suction pressures on the roof or that the ASCE zones may need to be adjusted to accommodate the distribution of enveloped tornado pressures.

For the peak enveloped pressure coefficients of an enclosed building shown in Figure 4.14, the ASCE envelope curves effectively envelope the experimental tornado data in all roof and wall zones. This is a departure from the observations for the perfectly sealed building. The effectiveness of the ASCE envelope curves appears to be tied to the increase in the positive bound for the design internal pressure from +0.18 for ABL winds to +0.55 for tornadoes, which was done in the standard to address the influence of the APD (ASCE,

2021). This seems to contrast the results from Figure 4.8, which showed an overall similarity in the peak pressures between the tornado and ABL flows, suggesting that the impact of the APD is minimal for this specific building. However, the increase in internal pressure in ASCE 7-22 further enveloped the tornado data, capturing most of the local variations observed between the tornado and ABL peak pressures indicated by Figure 4.8.

The results from Figure 4.15 for a partially enclosed building tend to closely resemble the trends observed for a perfectly sealed building, in which the peak minimum pressure coefficients exceed the ASCE 7-22 envelope curves in all zones aside from roof Zone 3. The main contributor to this is the use of the same internal pressure of $+0.55$ for both the enclosed and partially enclosed opening cases, meaning that the envelope curves from ASCE 7-22 remain unchanged between the enclosed and partially enclosed configurations. This is a departure from the observations made in Figure 4.9 for a partially enclosed building exposed to tornado winds, in which there was a further increase in minimum peak net pressure coefficients due to the additional internal pressurization caused by the "ballooning" effect from the impinging winds on the dominant opening.

While these results presented for the perfectly sealed and partially enclosed building seem to indicate that the proposed ASCE 7-22 tornado loads are inadequate for C&C design, it is important to recognize that only one building geometry, three building orientations and one tornado scenario were considered for the current analysis while the ASCE 7-22 data was derived from over 5,000 simulations (ASCE, 2021). The case presented in this study tends to represent a worst-case scenario for tornado loading (Razavi and Sarkar, 2018) while the code represents the loads for more general conditions, which might contribute to the discrepancies. This considered, it appears that the proposed ASCE 7-22 tornado loads are effective for the design of low-rise buildings under various opening conditions, but further refinements in the internal pressures and loading zones may be required to better represent the net tornado load conditions.

Opening Condition: Perfectly Sealed

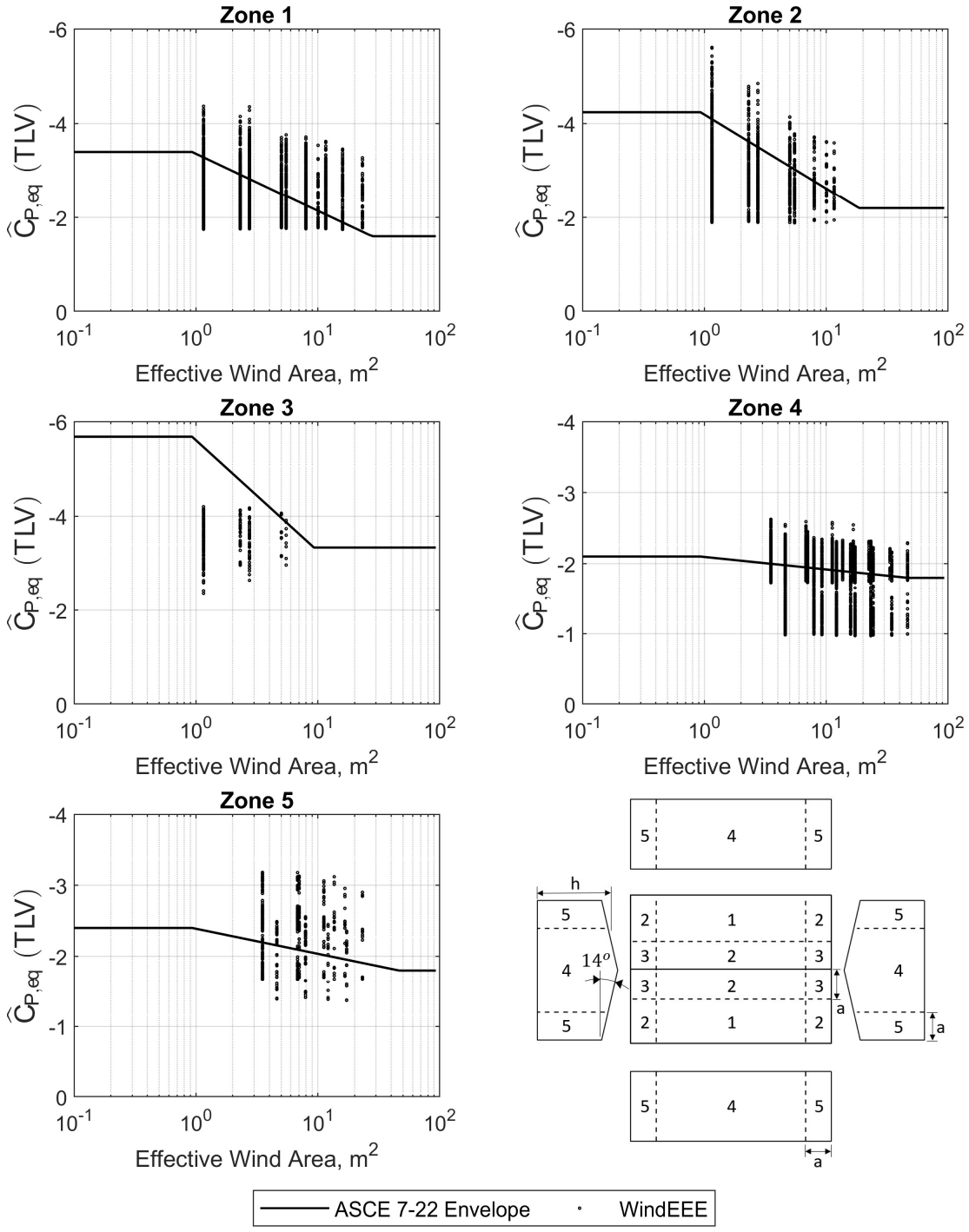

Figure 4.13: Comparison of the area-averaged enveloped minimum peak pressure coefficients from the tornado experimental data to the ASCE 7-22 C&C envelope curves for a perfectly sealed building.

Opening Condition: Enclosed

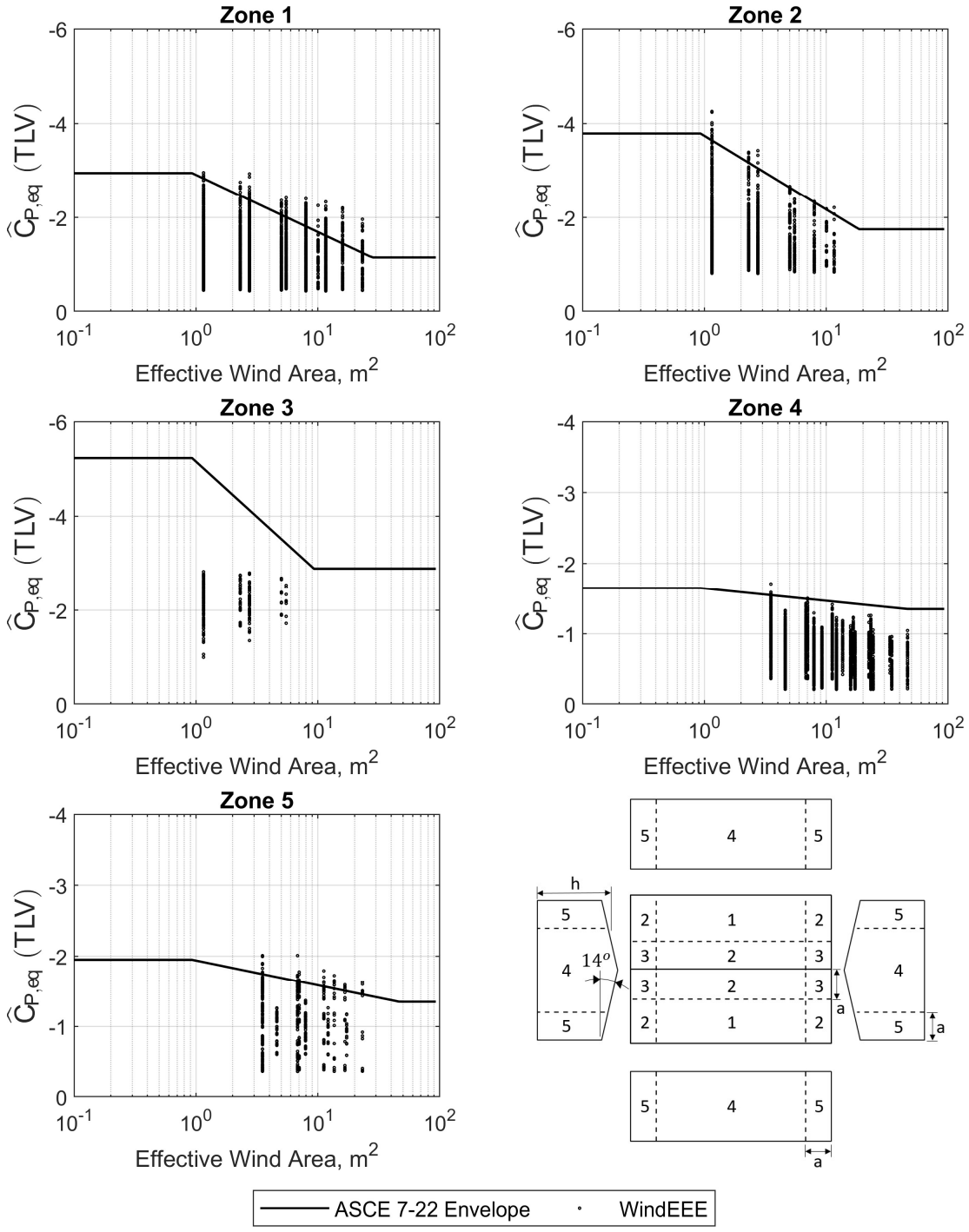

Figure 4.14: Comparison of the area-averaged enveloped minimum peak pressure coefficients from the tornado experimental data to the ASCE 7-22 C&C envelope curves for an enclosed building.

Opening Condition: Partially Enclosed

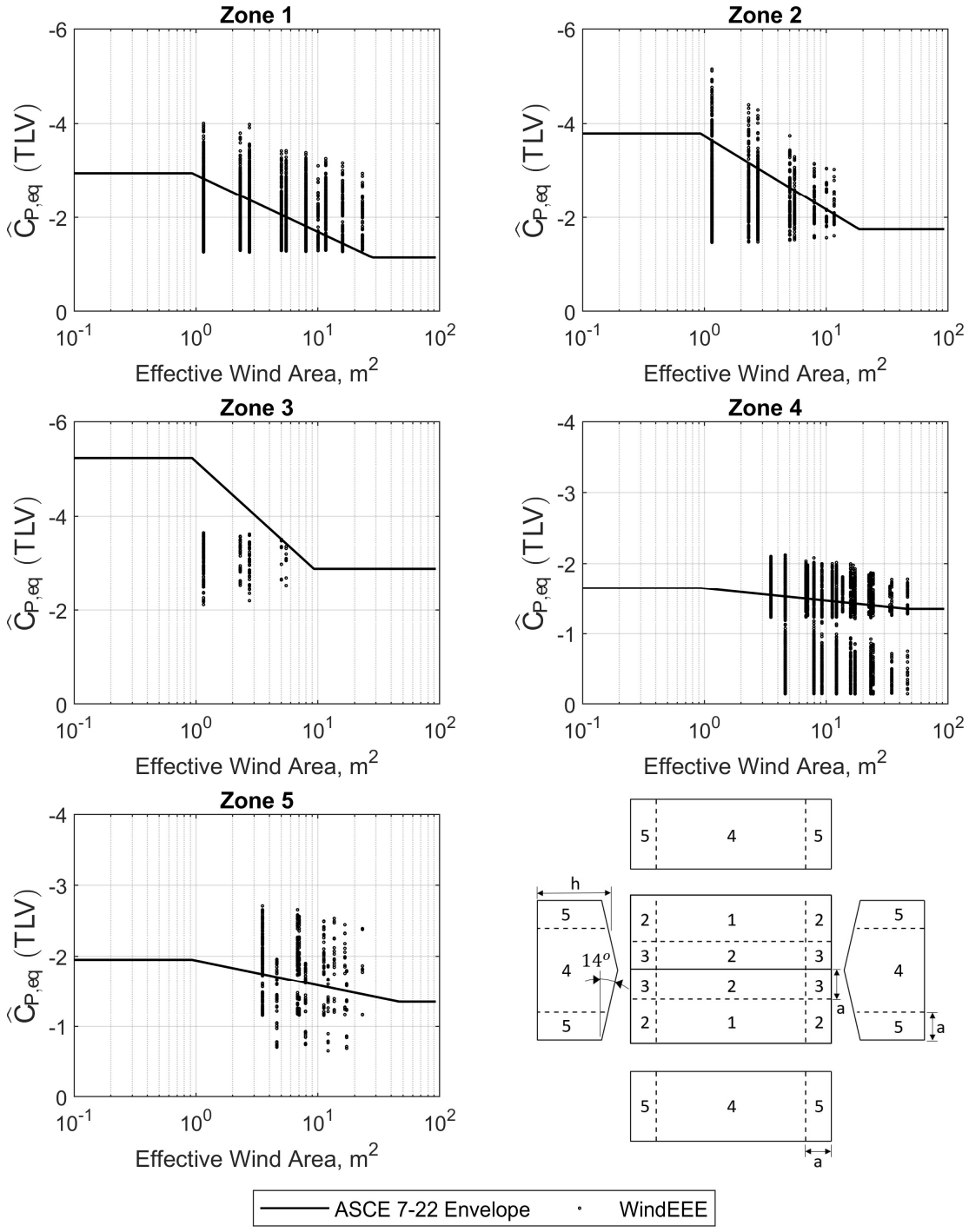

Figure 4.15: Comparison of the area-averaged enveloped minimum peak pressure coefficients from the tornado experimental data to the ASCE 7-22 C&C envelope curves for a partially enclosed building.

As was done in Chapter 3, a case study was considered assuming the study building is located in Chicago, IL, which is depicted in Figure 4.16 for the partially enclosed opening configuration. The new tornado chapter in ASCE 7-22 contains tornado hazard maps that can be used to determine tornado design wind speeds based on the building's location, size, and risk category. From wind speed hazard maps provided in ASCE 7-22, three design wind speeds were selected: 35.8 m/s, 49.2 m/s and 68.4 m/s, which correspond to mean recurrence intervals (MRI's) of 3000, 10,000 and 100,000 years. The ASCE 7-22 peak pressure coefficient envelope curves were converted into design pressures by multiplying the coefficients by the dynamic pressure corresponding to each full-scale wind speed: $\frac{1}{2}\rho K_{zTor} K_e V_T^2$. For comparison, the WindEEE tornado loads were multiplied by the reference dynamic pressure, $\frac{1}{2}\rho V_{ref}^2$, corresponding to the assumed full-scale horizontal wind speed of 49.2 m/s, which is the upper-limit wind speed of an EF1 tornado. For an MRI of 10,000 years, since the design wind speed is equal to the upper limit of an EF1 tornado, the trends between the ASCE envelope curve and tornado pressure data are the same as those displayed in Figure 4.15. When an MRI of 3,000 years is considered, the design pressures are much lower than those from the case study EF1 tornado. This result is sensible since the design wind speed is significantly reduced to account for the unlikelihood that the building will be close to the core of the vortex during a tornado event. At the other extreme, the 100,000-year MRI design wind speed completely envelops the WindEEE-derived enveloped component and cladding loads from an EF1 tornado aside from some minor exceedances in Zone 1.

Opening Condition: Partially Enclosed

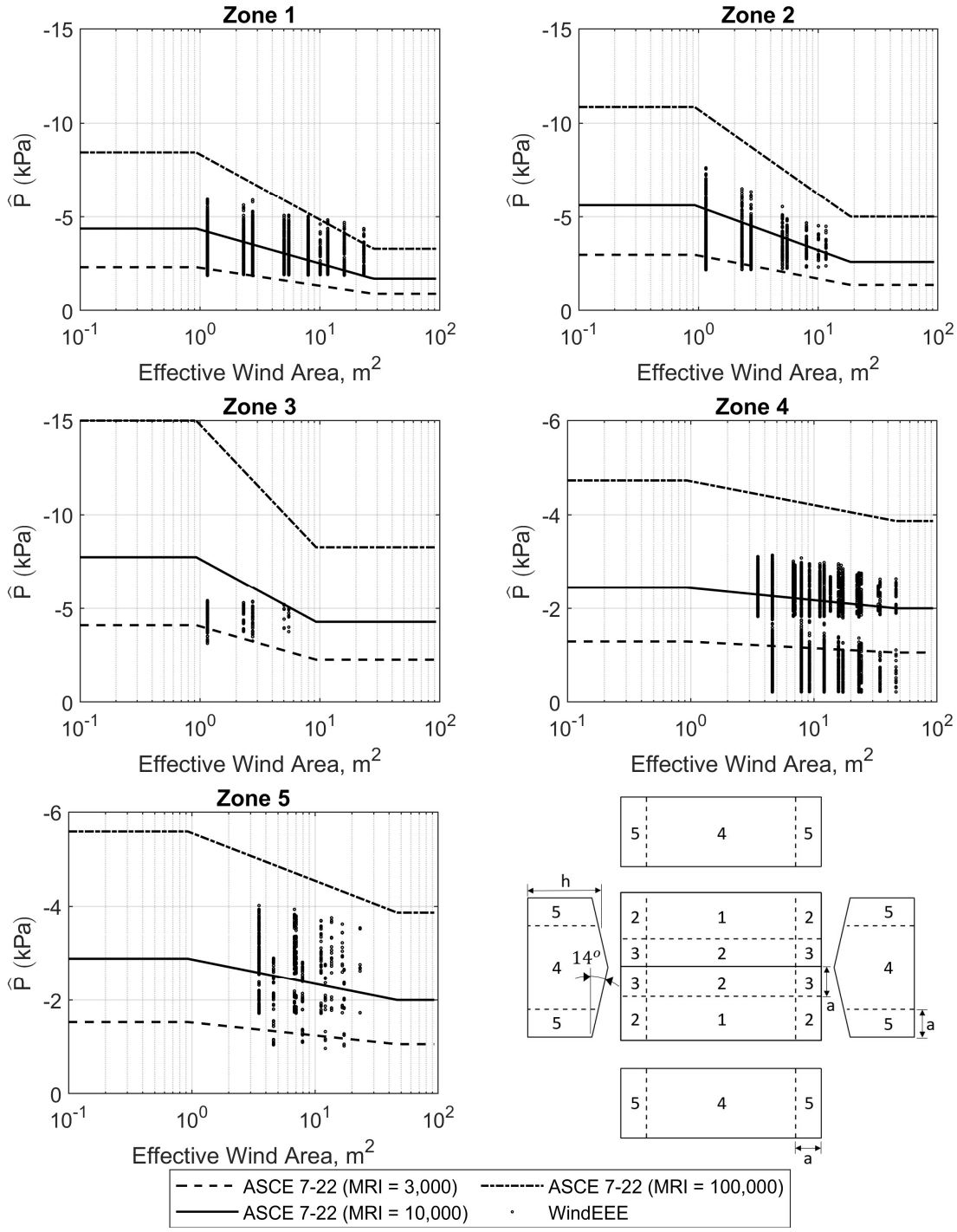

Figure 4.16: Case study comparison of the area-averaged enveloped minimum peak pressures from the tornado experimental data with the ASCE 7-22 C&C envelope curves for a partially enclosed building located in Chicago, IL for three mean recurrence intervals (MRI's).

4.4 Conclusions

External pressures were measured for a gable roof low-rise building model in the WindEEE Dome tornado simulator at Western University, which were used to estimate the internal pressures for simple opening configurations that represented an enclosed and partially enclosed building. The net peak pressure coefficients were compared to atmospheric boundary layer wind net pressures obtained from the NIST aerodynamic database for the same building geometry (Ho et al., 2005), with the same numerical model used to estimate the internal pressures. Further, the tornado net pressures were compared to the new component and cladding tornado load provisions proposed in the new ASCE 7-22 standard (ASCE, 2021). The comparisons of the component and cladding wind loads led to the following key findings:

i) The enveloped tornado peak pressures for a perfectly sealed building exceed those from ABL winds at all pressure taps throughout the building envelope due to the presence of the atmospheric pressure drop (APD) inducing an additional negative pressure on the building surface.

ii) Peak enveloped tornado-induced pressures are closely in-line with those from ABL winds on average once openings are incorporated for an enclosed or partially enclosed building, which diminished the influence of the APD. However, local differences saw tornado-induced pressures exceed those from ABL winds by up to 250% in the roof edge and corner regions, while ABL-induced pressures exceeded those from the tornado by 40% in the ridge corner zones.

iii) The greatest differences between tornado and ABL-induced wind loads tend to be in regions of flow separation, which falls in line with observations from other recent tornado load studies (Kopp and Wu, 2020; Roueche et al., 2020; Wang and Cao, 2021).

iv) For the building geometry and simulated tornado studied in this chapter, the proposed ASCE 7-22 tornado loads for component and cladding elements conservatively envelop the tornado-induced peak pressure coefficients for the enclosed building but are unconservative for the perfectly sealed and partially enclosed opening cases in all areas except at “Zone 3” near the roof ridge corners.

From these results, further refinements in the internal pressures and component and cladding loading zones may be required to better represent the tornado load conditions.

There are important limitations tied to the results that need to be considered as they are interpreted. First, there are no standard definitions of reference velocity for tornado experimental tests as there are for ABL wind tunnel studies, and thus any changes in the reference velocity will influence the magnitudes of the pressure coefficients. As well, the study only investigated one building geometry and a limited range of building orientations, due to time and economic constraints. Further, the pressure tap densities over the building envelope were reasonable considering the model size, but further refinement would be required to enable a more detailed study of component and cladding loads. Finally, assumptions regarding tornado scaling are based on limitations of both the collected full-scale tornado data and the physical limits of the WindEEE Dome facility.

References

Amidror, I., 2002. Scattered data interpolation methods for electronic imaging systems: a survey. J. Electron. Imaging 11, 157–176. https://doi.org/10.1117/1.1455013

ASCE, 2017. Minimum design loads and associated criteria for buildings and other structures. American Society of Civil Engineers, Reston, Virginia.

ASCE, 2021. Draft of minimum design loads and associated criteria for buildings and other structures (released for public comment). American Society of Civil Engineers, Reston, Virginia.

Ashrafi, A., Romanic, D., Kassab, A., Hangan, H., Ezami, N., 2021. Experimental investigation of large-scale tornado-like vortices. J. Wind Eng. Ind. Aerodyn. 208. https://doi.org/10.1016/j.jweia.2020.104449

Baker, C., Sterling, M., 2019. Are tornado vortex generators fit for purpose? J. Wind Eng. Ind. Aerodyn. 190, 287–292. https://doi.org/10.1016/j.jweia.2019.05.011

Davenport, A.G., 1964. Note on the distribution of the largest value of a random function with application to gust loading. Insitution Civ. Eng. 28, 187–196. https://doi.org/https://doi.org/10.1680/iicep.1964.10112

Durst, C.S., 1960. The statistical variation of wind with distance. Q. J. R. Meteorol. Soc. 86, 543–549.

Duthinh, D., Main, J.A., Phillips, B.M., 2015. Methodology to analyze wind pressure data on components and cladding of low-rise buildings. Gaithersburg, Maryland.

Gierson, M.L., Phillips, B.M., Duthinh, D., Ayyub, B.M., 2017. Wind-pressure coefficients on low-rise building enclosures using modern wind-tunnel data and Voronoi diagrams. ASCE-ASME J. Risk Uncertain. Eng. Syst. Part A Civ. Eng. 3, 04017010. https://doi.org/10.1061/ajrua6.0000915

Haan, F.L., Balaramudu, V., Sarkar, P.P., 2010. Tornado-induced wind loads on a low-rise building. J. Struct. Eng. 136, 106–116. https://doi.org/10.1061/(ASCE)ST.1943-541X.0000093

Haan, F.L., 2017. An examination of static pressure and duration effects on tornado-induced peak pressures on a low-rise building. Front. Built Environ. 3, 1–11. https://doi.org/10.3389/fbuil.2017.00020

Ho, E., Surry, D., Morrish, D., 2003. NIST/TTU cooperative agreement - windstorm mitigation initiative: wind tunnel experiments on generic low buildings, BLWT-SS20-2003.

Ho, E., Surry, D., Morrish, D., Kopp, G.A., 2005. The UWO contribution to the NIST aerodynamic database for wind loads on low buildings: Part 1. Archiving format and

basic aerodynamic data. J. Wind Eng. Ind. Aerodyn. 93, 1–30. https://doi.org/10.1016/j.jweia.2004.07.006

Insurance Information Institute, 2020. Natural catastrophe losses in the United States by peril: archived tables [WWW Document]. URL https://www.iii.org/table-archive/21420

Jaffe, A.L., Kopp, G.A., 2021. Internal pressure modelling for low-rise buildings in tornadoes. J. Wind Eng. Ind. Aerodyn. 209, 104454. https://doi.org/10.1016/j.jweia.2020.104454

Kassab, A., 2021. Experimental study of tornado-induced pressures. (Ph.D. Dissertation) Western University Electronic Thesis and Dissertation Repository.

Kikitsu, H., Sarkar, P.P., Haan, F.L., 2011. Experimental study on tornado-induced loads of low-rise buildings using a large tornado simulator, in: 13th International Conference on Wind Engineering. Amsterdam.

Kopp, G.A., Morrison, M.J., 2014. Component and cladding pressures and zones for the roofs of low-rise buildings. University of Western Ontario, London, ON, Canada.

Kopp, G.A., Morrison, M.J., 2018. Component and cladding wind loads for low-slope roofs on low-rise buildings. J. Struct. Eng. 144, 04018019. https://doi.org/10.1061/(asce)st.1943-541x.0001989

Kopp, G.A., Wu, C.H., 2020. A framework to compare wind loads on low-rise buildings in tornadoes and atmospheric boundary layers. J. Wind Eng. Ind. Aerodyn. 204, 104269. https://doi.org/10.1016/j.jweia.2020.104269

Kosiba, K.A., Wurman, J., 2013. The three-dimensional structure and evolution of a tornado boundary layer. Weather Forecast. 28, 1552–1561. https://doi.org/10.1175/WAF-D-13-00070.1

Letchford, C.W., Levitz, B., James, D.L., 2015. Internal pressure dynamics in simulated tornadoes, in: Structures Congress 2015. American Society of Civil Engineers, Reston, Virginia, pp. 2689–2701.

Lombardo, F.T., 2018. Engineering analysis of a full-scale high-resolution tornado wind speed record. J. Struct. Eng. (United States) 144, 1–9. https://doi.org/10.1061/(ASCE)ST.1943-541X.0001942

Main, J.A., 2011. Special-purpose software: MATLAB functions for estimation of peaks from time series [WWW Document]. URL www.itl.nist.gov/div898/winds/homepage.htm (accessed 1.15.21).

McDonald, J.R., Mehta, K.C., Mani, S., 2006. A recommendation for an Enhanced Fujita Scale (EF-Scale), Revision 2, Wind Science and Engineering Center, Texas Tech University. Lubbock, Texas.

Mishra, A.R., James, D.L., Letchford, C.W., 2008. Physical simulation of a single-celled tornado-like vortex, Part B: Wind loading on a cubical model. J. Wind Eng. Ind. Aerodyn. 96, 1258–1273. https://doi.org/10.1016/j.jweia.2008.02.027

NOAA, 2021. Monthly and annual U.S. tornado summaries [WWW Document]. NOAA / Natl. Weather Serv. Strorm Predict. Cent. URL https://www.spc.noaa.gov/climo/online/monthly/newm.html (accessed 6.10.21).

Northern Tornado Project, 2021. Northern Tornado Project open data [WWW Document]. URL https://westernu.maps.arcgis.com/apps/dashboards/19460b79cf24493680e5792f5247f46d (accessed 6.10.21).

Oh, J.H., Kopp, G.A., Inculet, D.R., 2007. The UWO contribution to the NIST aerodynamic database for wind loads on low buildings: Part 3. Internal pressures. J. Wind Eng. Ind. Aerodyn. 95, 755–779. https://doi.org/10.1016/j.jweia.2007.01.007

Prevatt, D.O., Roueche, D.B., Van De Lindt, J.W., Pei, S., Dao, T.N., Coulbourne, W., Graettinger, A.J., Gupta, R., Grau, D., 2012a. Building damage observations and EF classifications from the Tuscaloosa, AL and Joplin, MO tornadoes. ASCE Struct. Congr. 2037–2045.

Prevatt, D.O., van de Lindt, J.W., Back, E.W., Graettinger, A.J., Pei, S., Coulbourne, W., Gupta, R., James, D.L., Agdas, D., 2012b. Making the case for improved structural design: tornado outbreaks of 2011. Leadersh. Manag. Eng. 12, 254–270. https://doi.org/10.1061/(asce)lm.1943-5630.0000192

Razavi, A., Sarkar, P.P., 2018. Tornado-induced wind loads on a low-rise building: Influence of swirl ratio, translation speed and building parameters. Eng. Struct. 167, 1–12. https://doi.org/10.1016/j.engstruct.2018.03.020

Refan, M., Hangan, H., 2018. Near surface experimental exploration of tornado vortices. J. Wind Eng. Ind. Aerodyn. 175, 120–135. https://doi.org/10.1016/j.jweia.2018.01.042

Refan, M., Hangan, H., Wurman, J., 2014. Reproducing tornadoes in laboratory using proper scaling. J. Wind Eng. Ind. Aerodyn. 135, 136–148. https://doi.org/10.1016/j.jweia.2014.10.008

Roueche, D.B., Prevatt, D.O., Haan, F.L., 2020. Tornado-induced and straight-line wind loads on a low-rise building with consideration of internal pressure. Front. Built Environ. 6, 1–18. https://doi.org/10.3389/fbuil.2020.00018

Sabareesh, G.R., Matsui, M., Tamura, Y., 2019. Vulnerability of roof and building walls under a translating tornado like vortex. Front. Built Environ. 5, 1–9. https://doi.org/10.3389/fbuil.2019.00053

Sadek, F., Simiu, E., 2002. Peak non-Gaussian wind effects for database-assisted low-rise

building design. J. Eng. Mech. 128, 530–539. https://doi.org/10.1061/(asce)0733-9399(2002)128:5(530)

Simiu, E., Pintar, A.L., Duthinh, D., Yeo, D., 2017. Wind load factors for use in the wind tunnel procedure. ASCE-ASME J. Risk Uncertain. Eng. Syst. Part A Civ. Eng. 3, 04017007. https://doi.org/10.1061/ajrua6.0000910

Solari, G., Burlando, M., De Gaetano, P., Repetto, M.P., 2015. Characteristics of thunderstorms relevant to the wind loading of structures. Wind Struct. An Int. J. 20, 763–791. https://doi.org/10.12989/was.2015.20.6.763

St. Pierre, L.M., Kopp, G.A., Surry, D., Ho, E., 2005. The UWO contribution to the NIST aerodynamic database for wind loads on low buildings: Part 2. Comparison of data with wind load provisions. J. Wind Eng. Ind. Aerodyn. 93, 31–59. https://doi.org/10.1016/j.jweia.2004.07.007

Van De Lindt, J.W., Pei, S., Dao, T.N., Graettinger, A.J., Prevatt, D.O., Gupta, R., Coulbourne, W., 2013. Dual-objective-based tornado design philosophy. J. Struct. Eng. (United States) 139, 251–263. https://doi.org/10.1061/(ASCE)ST.1943-541X.0000622

Wang, J., Cao, S., 2021. Characteristics of tornado wind loads and examinations of tornado wind load provisions in ASCE 7–16. Eng. Struct. 241, 112451. https://doi.org/10.1016/j.engstruct.2021.112451

Chapter 5

5 Conclusions

In the present work, a low-rise, gable roof high frequency pressure integration (HFPI) model was constructed and tested at the WindEEE Dome facility, a state-of-the-art tornado simulator. One multi-celled tornado-like vortex was generated with scaled properties that resembled the 2009 Goshen County, Wyoming tornado. The simulated tornado was translated past the building model at a speed of 1.5 m/s, with three building orientations considered. External pressure measurements were obtained from 360 taps distributed over the building surface in addition to ground pressures obtained from 120 taps radially distributed around the building. Reference tornado velocity measurements were obtained from a separate set of experiments carried out by Kassab (2021).

The tornado loads and pressures obtained from the WindEEE tests were compared to atmospheric boundary layer (ABL)-induced wind loads from a straight-line wind tunnel test in addition to design loads from the proposed tornado-specific Chapter 32 in the upcoming ASCE 7-22 standard. The ABL wind loads were obtained from the NIST aerodynamic database for a low-rise building that matched the dimensions of the model tested in the WindEEE Dome (Ho et al., 2005). Adjustments were made to the reference velocity and tap layouts to aid in a direct comparison with the WindEEE tornado wind loads. Internal pressures were estimated using the Multiple Discharge Equations for both the tornado and ABL datasets in order to determine net pressures for assumed enclosed (distributed leakage) and partially enclosed (dominant opening on the windward wall) opening conditions.

The first set of comparisons between the tornado, ABL, and ASCE 7-22 loads involved the main wind force resisting system (MWFRS) of the building. In this case, a structural system consisting of six evenly spaced moment frames was assumed. Two-global force coefficients, corresponding to the uplift and lateral loads, were computed for each of the five building bays. In addition, moment coefficients were calculated at the ridge and knees of the frames. The peak force and moment coefficients were enveloped over all tested

building orientations and compared for a perfectly sealed building and the two opening conditions.

The second set of comparisons pertained to the component and cladding (C&C) loads on the structure. To start, the peak pressure coefficients at each tap were compared between the tornado and ABL wind datasets to evaluate similarities and differences between the enveloped distributions for all opening configurations. The peak pressure coefficients were then area-averaged and evaluated against the component and cladding design pressure curves in ASCE 7-22 for specific building zones.

5.1 Summary of Findings

A number of conclusions were drawn from this study, which are summarized as follows:

- The peak MWFRS enveloped uplift, lateral force and moment coefficients from the tornado-induced loading exceeded the ABL wind loads for a perfectly sealed building. The enveloped tornado peak pressures pertaining to the C&C of a perfectly sealed building also exceeded those from ABL winds at all pressure taps throughout the building envelope. These differences highlighted the impact of the atmospheric pressure drop (APD) and enhanced suction pressures on the resulting tornado loads.
- The assumed opening conditions representing an enclosed or partially enclosed building led to reductions in the net tornado uplift and moment coefficients, closely aligning them with the ABL wind-induced net loads for the same enclosure classifications.
- Peak enveloped tornado-induced pressures were closely in-line with those from ABL winds once openings were incorporated for an enclosed or partially enclosed building, which diminished the influence of the APD. The greatest differences in local net peak pressure coefficients between tornado and ABL-induced wind loads tended to be in regions of flow separation.
- The proposed MWFRS tornado loads from ASCE 7-22 effectively enveloped the peak tornado uplift and moment coefficients for the enclosed building configuration

but were slightly unconservative for the perfectly sealed and partially enclosed buildings despite tornado-specific modifications made to the roof uplift design pressures and the internal pressure coefficients. Further, the proposed ASCE 7-22 C&C loads conservatively enveloped the tornado-induced peak pressure coefficients for the case of an enclosed building but were unconservative for the perfectly sealed and partially enclosed buildings in all areas except at "Zone 3" near the roof ridge corners.

- Considering that only one building placed at a critical position relative to the tornado vortex was experimentally studied in this thesis, it was determined that the ASCE tornado wind loads performed well in generating representative tornado loads for low-rise building design.

5.2 Recommendations for Future Work

The following recommendations for future research can be made to extend the work completed in the current study and to address some of its limitations:

- The analysis contained herein can be extended to multiple building geometries and tornado structures in order to generalize the results. Due to the limitations and economic costs associated with experimental testing at the WindEEE Dome, numerical approaches such as through the use of computational fluid dynamics (Nasir and Bitsuamlak, 2016; Gairola and Bitsuamlak, 2019), could aid in this effort.
- The tornado wind loads compared in this study corresponded to an isolated building in open terrain. More work needs to be done to understand the effects of the building surroundings and surrounding topography on the resulting tornado wind structure and loads.
- The assumptions regarding tornado scaling still had a limiting impact on the size of the building model tested, while Baker and Sterling (2019) have highlighted the limitations of current tornado simulators to effectively scale tornadoes from nature. Therefore, the use of alternative methods, including new tornado generation modes in the WindEEE Dome (Ashrafi et al., 2021), computational simulations, or

augmentations of typical boundary layer wind tunnel facilities to accommodate non-synoptic wind flows (Catarelli et al., 2020) can further aid in understanding the effects of tornado-induced loading.

- The internal pressures utilized in this analysis were estimated for a single interior volume under the assumption that they were closely related to the weighted average of external pressures. Further research efforts are needed to understand the effects of compartmentalization on tornado-induced internal pressures and the rate at which the internal pressure equalizes the APD present at the core of the tornado vortex.
- Further work is recommended on methods to standardize reference velocities and ambient pressures for use in deriving tornado pressure coefficients in order to enable easier and effective comparisons with ABL wind pressure measurements. Such a task, which may include simultaneously measuring reference velocities and pressures as is typically done in boundary layer wind tunnel testing, has many challenges, a few of which were outlined by Kopp and Wu (2020).

References

Ashrafi, A., Romanic, D., Kassab, A., Hangan, H., Ezami, N., 2021. Experimental investigation of large-scale tornado-like vortices. J. Wind Eng. Ind. Aerodyn. 208. https://doi.org/10.1016/j.jweia.2020.104449

Baker, C., Sterling, M., 2019. Are tornado vortex generators fit for purpose? J. Wind Eng. Ind. Aerodyn. 190, 287–292. https://doi.org/10.1016/j.jweia.2019.05.011

Catarelli, R.A., Fernández-Cabán, P.L., Phillips, B.M., Bridge, J.A., Masters, F.J., Gurley, K.R., Prevatt, D.O., 2020. Automation and new capabilities in the University of Florida NHERI boundary layer wind tunnel. Front. Built Environ. 6, 1–11. https://doi.org/10.3389/fbuil.2020.558151

Gairola, A., Bitsuamlak, G.T., 2019. Numerical tornado modeling for common interpretation of experimental simulators. J. Wind Eng. Ind. Aerodyn. 186, 32–48. https://doi.org/10.1016/j.jweia.2018.12.013

Ho, E., Surry, D., Morrish, D., Kopp, G.A., 2005. The UWO contribution to the NIST aerodynamic database for wind loads on low buildings: Part 1. Archiving format and basic aerodynamic data. J. Wind Eng. Ind. Aerodyn. 93, 1–30. https://doi.org/10.1016/j.jweia.2004.07.006

Kassab, A., 2021. Experimental study of tornado-induced pressures. (Ph.D. Dissertation) Western University Electronic Thesis and Dissertation Repository.

Kopp, G.A., Wu, C.H., 2020. A framework to compare wind loads on low-rise buildings in tornadoes and atmospheric boundary layers. J. Wind Eng. Ind. Aerodyn. 204, 104269. https://doi.org/10.1016/j.jweia.2020.104269

Nasir, Z., Bitsuamlak, G.T., 2016. Computational modeling of hill effects on tornado like vortex. Proceedings, Annu. Conf. - Can. Soc. Civ. Eng. 3, 1844–1854.

Curriculum Vitae

Name:	Cody Van Der Kooi
Post-secondary Education and Degrees:	McMaster University Hamilton, Ontario, Canada 2014-2019 B.Eng. Civil Engineering and Management
	The University of Western Ontario London, Ontario, Canada 2019-2021 M.E.Sc. Civil and Environmental Engineering
Honours and Awards:	NSERC Canada Graduate Scholarship (CGSM) 2019-2020
	Alan G. Davenport Memorial Scholarship 2020
	Ontario Graduate Scholarship 2020-2021
Related Work Experience	Teaching Assistant The University of Western Ontario 2019-2020